BIOGEOCHEMICAL RESPONSES OF THE EARTH SYSTEM TO MASSIVE CARBON CYCLE PERTURBATIONS AND THE CENOZOIC LONG-TERM EVOLUTION OF CLIMATE: A MODELING PERSPECTIVE

A DISSERTATION SUBMITTED TO THE GRADUATE DIVISION OF THE UNIVERSITY OF HAWAIʻI AT MĀNOA IN PARTIAL FULFILLMENT OF THE REQUIREMENTS FOR THE DEGREE OF

DOCTOR OF PHILOSOPHY

IN

OCEANOGRAPHY

DECEMBER 2017

By

Nemanja Komar

Dissertation Committee:

Richard Zeebe, Chairperson
Fred Mackenzie
Jane Schoonmaker
Gerald Dickens
David Beilman

ACKNOWLEDGMENTS

Above all, I would like to thank my friend, mentor, and advisor, Dr. Richard Zeebe to whom I will be eternally indebted. Not only has Richard served as an exceptional role model in terms of science but more importantly, he has taught me a lot about life in general. His understanding and knowledge of the field is unparalleled but even more exceptional are his interpersonal skills and the chemistry he creates with all the members of his research group. His mentorship and guidance is truly exemplary. It has been an honor and privilege to have had Richard guide me throughout my entire graduate career. Thank you, Richard!

I also want to extend my sincere thanks to my dissertation committee: Drs. Fred Mackenzie, Jane Schoonmaker, Gerald Dickens and David Beilman. I am grateful for their constructive criticism, patience, support, and encouragement.

Graduate school has been a very long journey during which I have crossed paths with many individuals who all contributed to shaping me into the person I am today. My success would not have been possible without their constant support as well as necessary, sporadic distractions. Thank you Slobodane, Nejc, Djole, and Jimmy for staying in touch despite living on the opposite side of the world. The friend support on this side of the planet was no less important; Olivia, Kim, Milane, Lazare, and Van, having you in my life is a true blessing, thank you for everything! Some (significant) others have not endured the process, nevertheless they played a serious role in my (graduate) life at some point, and I would like to use this opportunity to thank "mojoj kokici" for all her sacrifices.

Last but not least, I would like to thank my dear mother Radojka, father Branko and sister Gordana who have always cheered me on and provided a much needed moral support

and unconditional love.

Financial support for the research presented in this dissertation was provided by a National Science Foundation subaward of OCE13-38842 and OCE16-58023 to Richard Zeebe.

ABSTRACT

Both short-term and long-term changes in climate and carbon cycling are reflected in oxygen ($\delta^{18}O$) and carbon ($\delta^{13}C$) isotope fluctuations in the geological record, often indicating a highly dynamic nature and close connection between climate and carbon cycling through the ocean-atmosphere-biosphere system. When used in conjunction with mathematical models, stable carbon and oxygen isotopes provide a powerful tool for deciphering magnitude and rate of past environmental perturbations. In this study, we focus on two transient global warming events and a multi-million-year evolution of climate: (1) the end-Permian ($\sim$252 Ma), (2) the Paleocene Eocene Thermal Maximum (PETM; $\sim$56 Ma), and (3) climatic and ocean chemistry variations across the Cenozoic. The transient events (1) and (2) are both accompanied by a massive introduction of isotopically light carbon into the ocean-atmosphere system, as indicated by prominent negative excursions of both $\delta^{13}C$ and $\delta^{18}O$. We use a combination of the well-established GEOCARB III and LOSCAR models to examine feedbacks between the calcium and carbon cycle during massive and rapid CO_2 release events, and feedbacks between biological production and the cycles of carbon, oxygen and phosphorus (C-O-P feedback). The coupled GEOCARB-LOSCAR model enables simulation of marine carbonate chemistry, $\delta^{13}C$, the calcite compensation depth (CCD) and organic carbon burial rates across different time scales. The results of the coupled carbon-calcium model (LOSCAR only model) suggest that ocean acidification, which arises due to large and rapid carbon input, is not reflected in the calcium isotope record during the end-Permian, contrary to the claims of previous studies. The observed changes in calcium isotopes arise due to 12,000 Pg C emitted by Siberian Trap volcanism, the consequent extinction of the open ocean primary producers, and variable

calcium isotope fractionation. The results presented in Chapter 3 indicate that the C-O-P mechanism may act as a negative feedback during high CO_2 emission events such as the PETM, restoring atmospheric CO_2 through increased organic carbon burial as a consequence of an accelerated nutrient delivery to the surface ocean and enhanced organic carbon export. Our results indicate that the feedback was triggered by an initial carbon pulse of 3,000 Pg C followed by an additional carbon leak of 2,500 Pg C. Through the C-O-P feedback, ∼2,000 Pg C could be sequestered during the recovery phase of the PETM but only if $CaCO_3$ export remained constant. Regarding long-term Cenozoic changes (Chapter 4), we propose that the temperature effect on metabolic rates played an important role in controlling the evolution of ocean chemistry and climate across multi-million-year time scales by altering organic carbon burial rates. Model predicted organic carbon burial rates combined with the ability to simulate the CCD changes imposes a critical constraint on the carbon cycle and aids in a better understanding carbon cycling during the Cenozoic. Our results suggest that the observed CCD trends over the past 60 million years were decoupled from the continental carbonate and silicate weathering rates. We identify two dominant mechanisms for the decoupling: (a) shelf-basin carbonate burial fractionation and (b) decreasing respiration of organic matter at intermediate water depths as the Earth transitioned from the greenhouse conditions of the Eocene to the colder temperatures of the Oligocene.

TABLE OF CONTENTS

LIST OF TABLES

LIST OF FIGURES

CHAPTER 1
INTRODUCTION

1.1 Overview of the Dissertation Content

This dissertation is a compilation of three research projects that were accomplished under the supervision and guidance of Dr. Richard E. Zeebe while pursuing a doctorate degree in Oceanography. Chapters 2 and 3 are published in peer reviewed scientific journals. The research presented in Chapter 4 is in preparation for submission. The following are the citations for these publications:

Chapter 2

Komar, N., and R. E. Zeebe (2016), Calcium and calcium isotope changes during carbon cycle perturbations at the end-Permian, Paleoceanography, 31, 115-130, doi:10.1002/2015PA002834.

Chapter 3

Komar, N., and R. E. Zeebe (2017), Redox-controlled carbon and phosphorus burial: A mechanism for enhanced organic carbon sequestration during the PETM, Earth and Planetary Science Letters, 479, 71-82, doi:10.1016/j.epsl.2017.09.011.

Chapter 4

Komar, N., and R. E. Zeebe (in preparation), Modeling the evolution of ocean carbonate chemistry, carbonate compensation depth, atmospheric CO_2, and climate over the Cenozoic. Journal to be determined.

In general, all three individual studies have the same underlying theme, investigating climate, carbon cycle dynamics and ocean chemistry of the past utilizing numerical modeling. Despite the differences in time scales and time periods examined in each of the studies (Chapter 2 and 3 consider Earth system response to short-term carbon cycle perturbations, whereas Chapter 4 focuses on long-term evolution of climate), the results collectively contribute to a better understanding of carbon cycling and biogeochemical feedbacks that regulate Earth's climate over millennia to multi-million year periods. The background and significance of each individual project (Chapters 2-4) is addressed in this chapter.

1.2 Global carbon cycle and LOSCAR

The carbon cycle refers to the carbon exchange between a number of carbon reservoirs through a variety of processes, taking place on different time scales. Shorter time scales encompass processes such as photosynthesis, respiration, air-sea exchange of CO_2, and accumulation of carbon in soil [e.g. *Post et al.*, 1990; *Berner*, 1999]. These processes transfer carbon within the so called surficial system, which includes atmosphere, biosphere, oceans, soils, and exchangeable sediments in the marine environment. On very long time scales (i.e. greater than 1 Ma years) the global surface carbon inventory is regulated by changes in the fluxes between surficial and geologic reservoirs (e.g. crustal rocks and deep sea sediments). Partitioning of carbon between the two systems controls the concentration of atmospheric CO_2 over geological time scales (Fig. 1.1) [e.g. *Berner*, 1999].

The dominant long-term processes that affect carbon transfer and control the partitioning of atmospheric CO_2 are volcanic degassing and weathering of organic carbon (carbon sources), and silicate weathering and burial of organic carbon (carbon sinks) [e.g. *Berner*, 1991, 1999;

Zeebe, 2012b]. The weathering of silicates removes atmospheric CO_2 in form of dissolved HCO_3^-, which is then transfered to the ocean by rivers and runoff and eventually precipitates as $CaCO_3$ in sediments. The sum of the described processes primarily governs the carbonate saturation state of the oceans, which dictates the position of the calcite compensation depth (CCD). Calcite compensation is a mechanism that maintains the balance between calcite weathering influx into the ocean and calcite sink (sediment burial). As long as the riverine flux of Ca^{2+} and CO_3^{2-} equals the $CaCO_3$ burial, the CCD remains unchanged [e.g. *Zeebe and Westbroek*, 2003]. If the system is disturbed (e.g. accelerated weathering), in order to preserve the steady state, the $CaCO_3$ saturation state of the ocean changes. In the case of excess weathering over burial, the saturation state will increase, thus leading to a deepening of the CCD, until the fluxes are balanced again [e.g. *Zeebe and Westbroek*, 2003; *Zeebe and Zachos*, 2013]. However, it is important to note that the CCD is not solely controlled by atmospheric CO_2 and weathering rates (higher weathering rates do not necessarily imply a deeper CCD). Other factors, such as the biological pump, shelf basin fractionation, rain ratio, weatherability, and bathymetry also affect the CCD and calcite saturation. In this dissertation we investigate both the short-term and long-term carbon cycle dynamics and quantify the effects of the above mention processes on the CCD evolution over the Cenozoic using numerical modeling. The numerical carbon cycle box models employed in the following chapters are the Long-term Ocean-atmosphere-Sediment CArbon cycle Reservoir model [LOSCAR; *Zeebe*, 2012a] and GEOCARB III [*Berner and Kothavala*, 2001].

LOSCAR is constructed to perform efficient computations of carbon partitioning between ocean, atmosphere and sediments on a wide range of timescales (from centuries to millions of years). The model is developed after a carbon cycle model designed by *Walker and Kasting*

[1992] but expanded to include a sediment module [*Zeebe and Zachos*, 2007]. LOSCAR has two different configurations representing modern ocean geometry (Figure 1.2) and Late Paleocene ocean geometry (Figure 1.3).

In the modern set-up, the model contains three ocean basins Atlantic (A), Indian (I), and Pacific (P), and one generic high latitude box (H). Each of the A,I, and P boxes is subdivided into surface (L), intermediate (M), and deep ocean (D; Figure 1.2).The H box, represents cold surface waters without reference to a specific location. Therefore, the total number of ocean boxes in the modern model version is 10. There is an additional box representing atmosphere, which exchanges weathering and gas fluxes between surface ocean and atmosphere. All ocean boxes are in contact with sediments. The paleo model version includes an additional ocean basin, Tethys, representing the ocean geometry when the Tethys ocean was still open. This model basin is also divided into surface, intermediate, and deep boxes, bring the total to 13 ocean boxes for the paleo model set-up (Figure 1.3).

Aside from differences in ocean geometry between the modern and paleo model set-up, the two model versions also have different circulation modes. The modern model version uses predominant North Atlantic Deep Water (NADW) formation, while the paleo model simulations employ Southern Ocean (SO) formation. The different circulation patterns are depicted with arrows in Figures 1.2 & 1.3.

The model contains a description of various biogeochemical tracers, including total carbon (TC), total alkalinity (TA), dissolved phosphorus (PO_4), dissolved oxygen, and stable carbon isotopes ($\delta^{13}C$), and $\%CaCO_3$ in sediments. Based on model predicted distribution and concentration of TC and TA, the model calculates other components of ocean carbonate chemistry system, e.g. pH, Ω, $[CO_3^{2-}]$, and $[HCO_3^-]$. Weathering of carbonate and silicate

rocks in LOSCAR is parameterized as follows:

$$F_{Si} = F^0_{Si} \times \left(\frac{p\mathrm{CO}_2}{p\mathrm{CO}^0_2}\right)^{n_{Si}} \tag{1.1}$$

$$F_C = F^0_C \times \left(\frac{p\mathrm{CO}_2}{p\mathrm{CO}^0_2}\right)^{n_{CC}} \tag{1.2}$$

where F_{Si} and F_C are silicate and carbonate weathering fluxes, respectively, and F^0_{Si} and F^0_C are the same fluxes at time $t = 0$. Similarly, $\mathrm{pCO_2}^0$ is the initial ($t = 0$) atmospheric $\mathrm{CO_2}$ concentration, and $\mathrm{pCO_2}$ is the atmospheric partial pressure calculated in the model at time t. n_{Si} and n_{CC} are silicate and carbonate weathering-$\mathrm{pCO_2}$ feedback parameters, respectively, which determine the strength of the feedback [see *Uchikawa and Zeebe*, 2008]. This parameterization describes the $\mathrm{CO_2}$-weathering feedback; when atmospheric $\mathrm{CO_2}$ concentration increases, it leads to a rise in temperature and to intensified hydrological cycle, which in turn results in enhanced weathering rates and an ultimate decrease in $\mathrm{pCO_2}$. It is essentially a mechanism that helps restore the ocean-atmosphere system back to pre-perturbation state after a rapid increase in atmospheric $\mathrm{pCO_2}$.

The $\mathrm{CaCO_3}$ dry weight content in the bioturbated sediment layer is calculated as a function of sediment rain, dissolution, burial and chemical erosion [*Zeebe and Zachos*, 2007; *Zeebe*, 2012a]. The sediment module includes variable sediment porosity. The surface area-depth relationship of the model sediment boxes is determined by the bathymtery data for a particular time domain [*Stuecker*, 2009].

1.3 Background and motivation of the individual studies

1.3.1 Chapter 2 introduction

Calcium carbonate ($CaCO_3$) deposition on the ocean floor is the major sink of both calcium and carbon [e.g. *Ridgwell and Zeebe*, 2005]. Additionally, the calcium and carbon cycles are connected through weathering of carbonate and silicate rocks, which are sources of both carbon and calcium. These processes are often represented by the following chemical reactions [e.g. *Walker and Kasting*, 1981]:

$$CaCO_3 + CO_2 + H_2O \longrightarrow Ca^{2+} + 2HCO_3^- \tag{1.3}$$

$$CaSiCO_3 + 2CO_2 + H_2O \longrightarrow Ca^{2+} + SiO_2 + 2HCO_3^- \tag{1.4}$$

Because both cycles exert great influence on oceanic alkalinity, dissolved inorganic carbon, and atmospheric CO_2, they play an important role in controlling Earth's climate [*Urey*, pp. 245, 1952; *Berner*, 1999]. This large, mutual sink and the major shared sources closely link the calcium and carbon cycles. Therefore variations in the carbon cycle (as inferred from $CaCO_3$ sedimentation and $\delta^{13}C$) may also be reflected in the oceanic calcium cycle and calcium isotopic composition of dissolved calcium in seawater ($\delta^{44}Ca_{sw}$) during major perturbations in carbon cycling [*Skulan et al.*, 1997; *Zhu and Macdougall*, 1998].

The most severe mass extinction event in Earth's history took place at the Permian-Triassic transition (end-Permian, ~252 Ma) [e.g. *Erwin*, 1993]. The event left an imprint in the sedimentary record, which exhibits a negative excursion in $\delta^{13}C$ of carbonate rocks

[e.g. *Magaritz et al.*, 1992; *Corsetti et al.*, 2005], a global temperature increase [*Holser et al.*, 1989], a negative excursion in calcium isotopes of marine sediments ($\delta^{44}Ca_{carb}$) [*Payne et al.*, 2010], and a possible decrease in calcium isotope of seawater [*Hinojosa et al.*, 2012]. Open ocean primary production was essentially non-existent during this time period [*Berner*, 1994; *Walker et al.*, 2002; *Erba*, 2006] and prior to the mass extinction event, biogenic precipitation of $CaCO_3$ (e.g. via coral and foraminifera) was confined to the shelf ocean areas. However, as these organisms suffered severe extinctions at the end-Permian, biogenic carbonate production was substantially diminished. In theory, a sudden loss of calcifiers should create an imbalance between the input and the output of carbon and alkalinity. Given enough time (a few thousand years), the riverine input of carbon and alkalinity would outpace the sink, resulting in a rapidly rising carbon content and alkalinity of the ocean, leading to a decline in atmospheric CO_2 and possibly cooling [*Caldeira and Rampino*, 1993]. As the evidence for significant imbalances in carbon and alkalinity fluxes is lacking [*Holser et al.*, 1989; *Magaritz and Holser*, 1991; *Retallack*, 1999; *Caldeira and Rampino*, 1993], there must be a mechanism that restores the imbalance caused by the absence of biogenic carbonate precipitation [e.g. *Ridgwell et al.*, 2003].

It has been previously suggested that in the absence of biogenic carbonate production, such as during mass extinction events (e.g., Cretaceous/Tertiary) an increased inorganic carbonate accumulation in shallow waters would compensate for the reduction in biogenically mediated carbonate production [*Caldeira and Rampino*, 1993]. In Chapter 2, we employ the Long-term Ocean-atmosphere-Sediment CArbon cycle Reservoir model (LOSCAR, *Zeebe* [2012a]) that has been expanded to trace $[Ca^{2+}]$ and $\delta^{44}Ca$ in both sediments and seawater (fully coupled C-Ca model) to explore the implications of the increased inorganic carbonate

precipitation on carbon and calcium cycle and ocean carbonate chemistry.

The main conclusion of Chapter 2 is that the changes in calcium isotopes observed in the sediment record are not a result of ocean acidification, as previously claimed [*Payne et al.*, 2010; *Hinojosa et al.*, 2012]. The model results suggest that a combination of factors resulted in the observed changes in δ^{13}C, δ^{44}Ca and temperature. The factors include emission of 12,000 Pg of carbon from Siberian Trap volcanism, and a variable calcium isotope fractionation that arises due to rapid changes in the ocean's carbonate ion concentration.

1.3.2 Chapter 3 introduction

Another major carbon cycle disruption and global temperature increase took place at the Paleocene Eocene boundary (∼56 Ma), during an event known as the Paleocene Eocene Thermal Maximum (PETM). The PETM left significant marks in both terrestrial and marine sediments, with geological records showing a negative carbon excursion of >2.5‰[*Kennett and Stott*, 1991], while the global temperature concomitantly increased by >5^{o}C [*Zachos et al.*, 2003; *McInerney and Wing*, 2011]. The event is associated with an abrupt and massive input of isotopically light carbon (>3,000 Pg C) into the ocean-atmosphere system over a few thousand years [e.g. *Zeebe et al.*, 2016]. Due to its rapid nature and the amount of carbon emitted, the PETM is often labeled as the closest paleoanalog for the ongoing and future anthropogenic climate change [e.g. *Zachos et al.*, 2008]. Accordingly, the PETM has received considerable attention within the paleo-climate community because quantifying and understanding biogeochemical changes during the PETM may offer insight into forthcoming changes caused by human activity.

The vast majority of the PETM studies investigated the initial and the main phase of the

event, constraining the sources, duration and magnitude of carbon input [e.g. *Dickens et al.*, 1995; *Zeebe et al.*, 2009, 2016], while very few studies focused on the recovery phase of the PETM. Chapter 3 investigates the mechanisms and feedbacks responsible for the termination of the PETM.

Because on long-time scales dissolved phosphorus in the ocean is a limiting nutrient [e.g. *Tyrrell*, 1999], its concentration affects the rate of the primary production and organic matter export (biological carbon pump). The temporal variation in the biological carbon pump, due to its influence on organic carbon burial, might play an important role in regulating climate on multi-millennial time scales [*Broecker*, 1982]. To simulate variations in the ocean's PO_4 inventory (and ultimately in organic carbon sequestration), the LOSCAR model (utilized in Chapter 2) was expanded here to include a long-term phosphorus cycle.

We show that the interplay between carbon, oxygen, and phosphorus (C-O-P) acts as a negative feedback during high CO_2 emission events, such as the PETM. Specifically, in our simulations restoration of elevated atmospheric CO_2 is triggered by an input of 3,000 Pg C to the ocean-atmosphere system. Due to a large initial pulse of carbon, high atmospheric CO_2 concentrations generate an increased nutrient delivery to the surface ocean, enhancing primary production and organic carbon burial, ultimately accelerating the system recovery. The C-O-P mechanism could be operating during other carbon perturbation events (not only the PETM). However, our preferred simulation requires $CaCO_3$ rain to remain constant or decrease in order to obtain results fully consistent with the PETM data.

1.3.3 Chapter 4 introduction

Sedimentary archives reveal dramatic changes in climate and reorganization in carbon cycling over the last 66 million years [*Zachos et al.*, 2001]. The planet has undergone a prominent ∼6 My long global warming period during the Late Paleocene Early Eocene (LPEE, ∼58-52 Ma), which culminated in the Early Eocene Climatic Optimum (∼52-50 Ma) with peak Cenozoic temperatures and an ice-free world [e.g. *Bijl et al.*, 2009; *Westerhold et al.*, 2011]. The warmest period of the Cenozoic was followed by a long-term global cooling period that commenced ∼50 Ma and persisted until modern days, which lead to the eventual formation of ice sheets in both hemispheres [e.g. *Cramer et al.*, 2009].

Of the two long-term trends described above, the global cooling is more anomalous as the trends observed do not behave according to rules of the conventional carbon cycle theory. The past 50 million years have been characterized by a decline in atmospheric CO_2 and a parallel temperature drop and therefore a reduced strength of the hydrological cycle. According to the current understanding of carbon cycle processes, the combination of these factors would lead to a deceleration of weathering fluxes due to the pCO_2-weathering feedback [e.g. *Walker and Kasting*, 1981; *Berner et al.*, 1983]. Everything else being constant, reduced weathering rates would diminish ocean alkalinity and result in CCD shoaling. However, carbonate mass accumulation rates over the past 50 Ma reveal CCD trends opposite to expectations, with the Pacific CCD deepening over this time interval by at least 1 km [*Pälike et al.*, 2012].

There have been a number of studies centered around investigation of the carbon cycle dynamics and climate across the Cenozoic [e.g. *Berner et al.*, 1983; *Berner and Kothavala*, 2001; *Wallmann*, 2001; *Arvidson et al.*, 2006; *Li and Elderfield*, 2013; *Caves et al.*, 2016]. However, none of the previous modeling work included an integral part of the long-term

carbon cycle, namely the CCD. In Chapter 4, we use an expanded version of the LOSCAR model [*Zeebe*, 2012a] called LOSCAR-P (see Chapter 3), which just like the original LOSCAR contains a sediment module allowing for reconstruction of the CCD along with ocean carbonate chemistry. The LOSCAR-P model used in this study is an extended LOSCAR version that incorporates the long-term phosphorus cycle coupled to a modified version of the GEOCARB III model [*Berner and Kothavala*, 2001]. Because dissolved P is a biolimiting nutrient on long time scales [e.g. *Tyrrell*, 1999], the addition of the P cycle has enabled predictive organic phosphorus and carbon burial rates.

The ability to simulate the CCD response during the Cenozoic along with predictive organic carbon burial rates imposes a crucial constraint on our carbon cycle reconstruction. The main conclusion that follows from our modeling efforts is that the global CCD deepening trend observed over the past 50 million years was decoupled from the carbon and silicate weathering input, for which we propose two decoupling mechanisms. First, sea level regression and consequent shelf-basin carbonate burial fractionation, led to more carbonate buried in the deep ocean relative to shelves going forward in time. Second, respiration of organic matter at intermediate water depths decreased as the global climate cooled and PO_4 concentration declined, thus increasing the carbonate ion content of intermediate waters, and instigating widespread and permanent CCD deepening.

1.4 Figures:

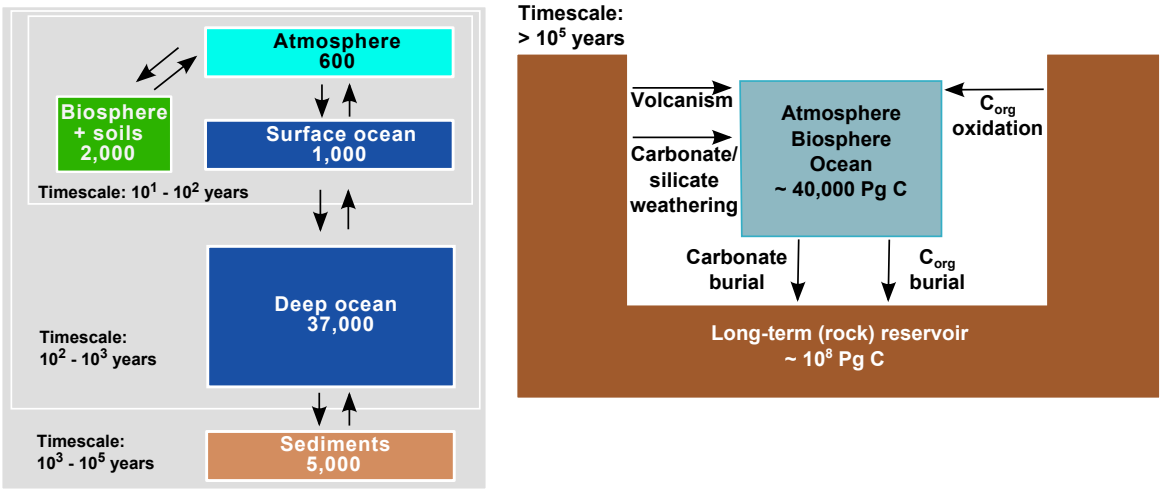

Figure 1.1: Left: Surficial (exogenic) carbon cycle. Right: Geologic (long-term) carbon cycle. Adopted from *Zeebe* [2012b].

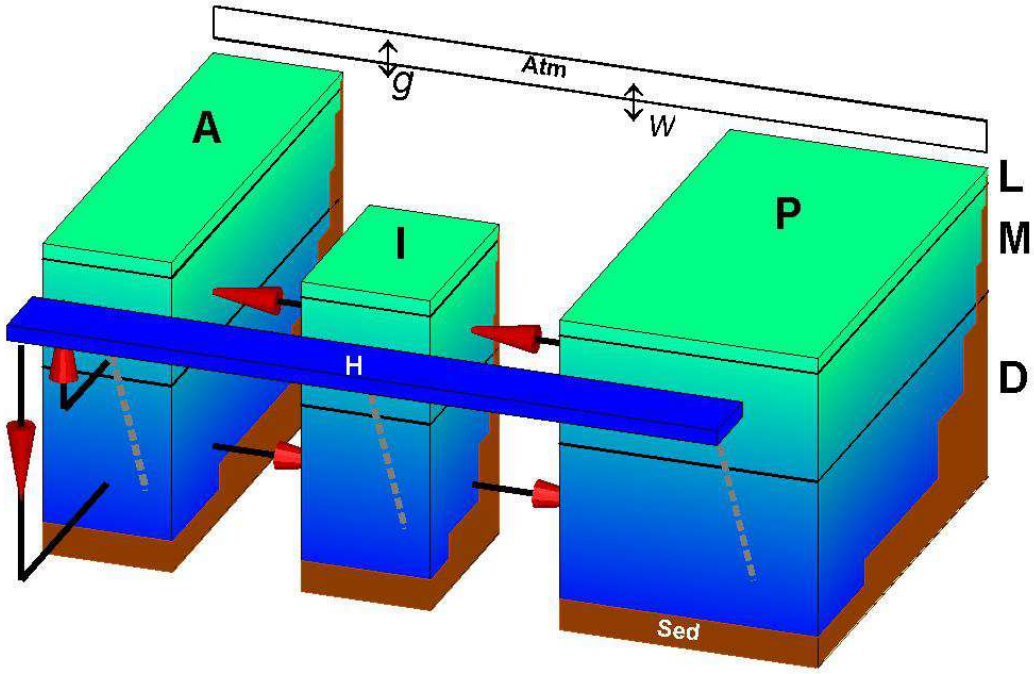

Figure 1.2: Schematic representation of the LOSCAR model (Modern configuration). A = Atlantic, I = Indian, P = Pacific, H = High-latitude surface, L = Low-latitude surface, M = interMediate, D = Deep box. Weathering fluxes and gas exchange with the atmosphere (Atm) are indicated by "w" and "g", respectively. Steps on the faces of ocean boxes indicate sediments (Sed).

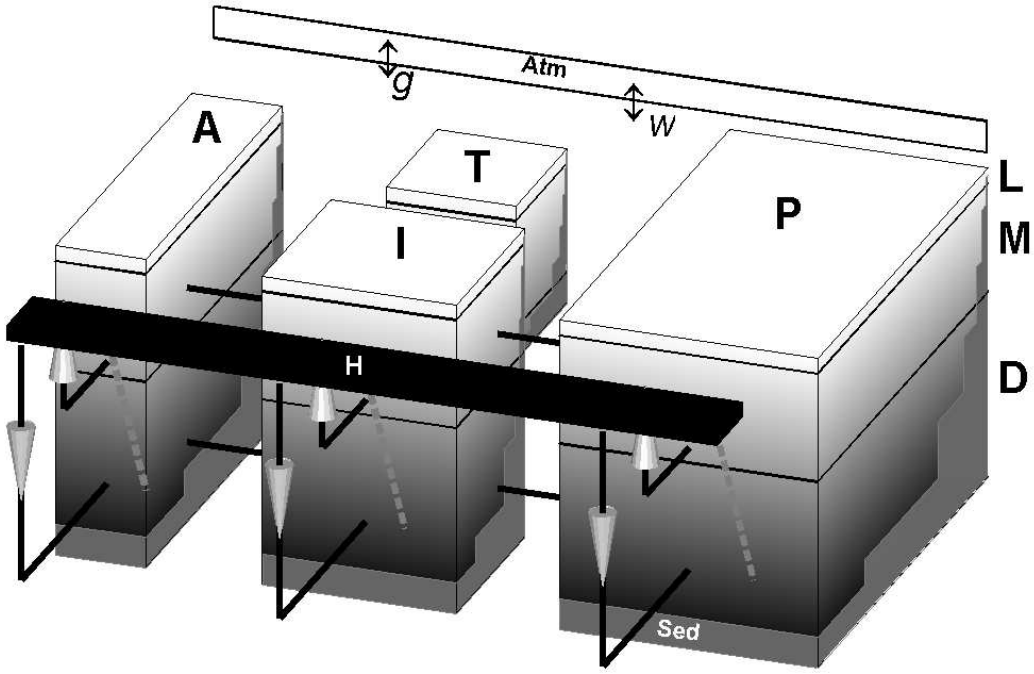

Figure 1.3: Schematic representation of the LOSCAR model (Paleocene/Eocene configuration). A = Atlantic, I = Indian, P = Pacific, T = Tethys ocean, H = High-latitude surface, L = Low-latitude surface, M = interMediate, D = Deep box. Weathering fluxes and gas exchange with the atmosphere (Atm) are indicated by "w" and "g", respectively. Steps on the faces of ocean boxes indicate sediments (Sed).

CHAPTER 2
CALCIUM AND CALCIUM ISOTOPE CHANGES DURING CARBON CYCLE PERTURBATIONS AT THE END-PERMIAN

Published in Paleoceanography

Komar, N., and R. E. Zeebe (2016), Calcium and calcium isotope changes during carbon cycle perturbations at the end-Permian, Paleoceanography, 31, 115-130, doi:10.1002/2015PA002834.

ABSTRACT

Negative carbon and calcium isotope excursions, as well as climate shifts, took place during the most severe mass extinction event in Earth's history, the end-Permian (∼252 Ma). Investigating the connection between carbon and calcium cycles during transient carbon cycle perturbation events, such as the end-Permian, may help resolve the intricacies between the coupled calcium-carbon cycles, as well as provide a tool for constraining the causes of mass extinction. Here, we identify the deficiencies of a simplified calcium model employed in several previous studies and we demonstrate the importance of a fully coupled carbon-cycle model when investigating the dynamics of carbon and calcium cycling. Simulations with a modified version of the LOSCAR model, which includes a fully coupled carbon-calcium cycle, indicate that increased weathering rates and ocean acidification (potentially caused by Siberian Trap volcanism) are not capable of producing trends observed in the record, as previously claimed. Our model results suggest that combined effects of carbon input via Siberian Trap volcanism (12,000 Pg C), the cessation of biological carbon export, and variable calcium isotope fractionation (due to a change in the seawater carbonate ion concentration) represents a more plausible scenario. This scenario successfully reconciles δ^{13}C and δ^{44}Ca trends observed in the sediment record, as well as the proposed warming of $>6^{o}$C.

2.1 Introduction

The calcium and carbon cycles in the ocean-atmosphere system are closely linked via weathering of carbonate and silicate rocks (sources of carbon and calcium) and calcium carbonate ($CaCO_3$) deposition, which is the major sink of both calcium and carbon [*Ridgwell and Zeebe*, 2005]. Both cycles affect oceanic alkalinity, dissolved inorganic carbon and atmospheric CO_2, therefore playing a major role in controlling earth's climate [*Urey*, pp. 245, 1952; *Berner*, 1999]. Sharing the major sources and sinks, fluctuations in the carbon cycle (as inferred from $CaCO_3$ sedimentation and $\delta^{13}C$) may also be reflected in the oceanic calcium cycle and calcium isotopic composition of dissolved calcium in seawater ($\delta^{44/40}Ca_{sw}$=$\delta^{44}Ca_{sw}$) during major perturbations in carbon cycling [*Skulan et al.*, 1997; *Zhu and Macdougall*, 1998]. Studying the connection between calcium and carbon cycling during transient carbon cycle perturbation events may help elucidate the intricacies of the coupled calcium-carbon cycles.

The largest known mass extinction of both terrestrial and marine organisms took place at the Permian-Triassic transition [*Erwin*, 1993], also known as the end-Permian ($\sim$ 252 Ma). Sedimentary records across the end-Permian show a negative excursion in the $\delta^{13}C$ of carbonate rocks [e.g *Magaritz et al.*, 1992; *MacLeod et al.*, 2000; *Corsetti et al.*, 2005], mass extinction of marine calcifiers [e.g. *Knoll et al.*, 1996; *Wignall and Newton*, 2003; *Knoll et al.*, 2007], a global temperature increase [*Holser et al.*, 1989; *Magaritz and Holser*, 1991; *Retallack*, 1999; *Sun et al.*, 2012], a negative excursion in calcium isotopes of marine sediments ($\delta^{44}Ca_{carb}$) [*Payne et al.*, 2010] and a possible drop in $\delta^{44}Ca$ of seawater [*Hinojosa et al.*, 2012] (Figure 2.1; $\delta^{44}Ca$ values reported are normalized to a bulk Earth standard), suggesting a carbon cycle and seawater carbonate chemistry perturbation. With the absence of pelagic calcifiers, open ocean carbonate production was essentially non-existent during

this time period [*Berner*, 1994; *Walker et al.*, 2002; *Erba*, 2006]. Before the mass extinction event, the organisms that were capable of biogenically precipitating $CaCO_3$ (e.g. corals and foraminifera) were mainly confined to the the shelf ocean areas, a mode of carbonate cycling also known as the "Neritan Ocean" [*Zeebe and Westbroek*, 2003]. These organism suffered severe extinctions at the end-Permian, resulting in a significantly reduced biogenic carbonate production. In theory, this should create an imbalance between the input and the output of carbon and alkalinity. If imbalances persisted for a period longer than a few thousand years, the riverine input of alkalinity and carbon would exceed the output and, alkalinity and carbon of the ocean would rapidly increase, leading to a decrease in atmospheric CO_2 and possibly cooling [*Caldeira and Rampino*, 1993]. Furthermore, depending on the duration and the magnitude of the disequilibrium, the deep ocean would eventually become supersaturated with respect to calcite. However, the evidence suggests that this was not the case during the end-Permian because temperatures rose by several degrees [*Holser et al.*, 1989; *Magaritz and Holser*, 1991; *Retallack*, 1999] while the sedimentation rates in deeper shelf sections appear to have dropped dramatically [*Bowring et al.*, 1998] indicating that there was no supersaturation with respect to calcite. Similar arguments also apply to the K/T boundary because there is no evidence for a fully saturated deep ocean or a drop in pCO_2 [*Caldeira and Rampino*, 1993] during this time period, suggesting presence of some other mechanism that keeps the ocean chemistry in balance.

The lack of evidence for large imbalances in alkalinity and carbon fluxes suggests that there has to be a mechanism that relatively quickly (on a time scale of several thousand years) compensates for the reduction in biogenically mediated carbonate precipitation, restoring the balance between inputs and outputs during the absence of biogenic carbonate production

[*Ridgwell et al.*, 2003]. *Caldeira and Rampino* [1993] showed that during a mass extinction event (i.e. Cretaceous/Tertiary), ocean chemistry might shift so that the diminution or complete cessation in biogenic $CaCO_3$ production can be compensated for by a significant increase in inorganic carbonate accumulation in shallow waters, which would have important implications for the global carbon and calcium cycle and ocean carbonate chemistry. Indeed, there is a large body of evidence for Early Triassic abiotic carbonate deposition as indicated by the ubiquitous occurrence of cements, seafloor fans, stromatolites, calcified bacteria etc. [*Grotzinger and Knoll*, 1995; *Woods et al.*, 1999; *Ridgwell and Zeebe*, 2005].

Here, we employ a modified version of a one-box, calcium isotope mass-balance model constructed by *Payne et al.* [2010] to study the possible effects of a major carbon perturbation accompanied by mass extinction of biota (such as the end-Permian) on ocean carbonate chemistry and the marine calcium cycle. We also point out problems in the assumptions made in the original model by *Payne et al.* [2010] pertaining to the shallow-water carbonate compensation mechanism explained above. Next, we utilize the Long-term Ocean-atmosphere-Sediment CArbon cycle Reservoir Model (LOSCAR) [*Zeebe*, 2012a] that has been expanded to trace $[Ca^{2+}]$ and $\delta^{44}Ca$ in the ocean (in both sediments and seawater), i.e. a fully coupled C-Ca model. This allows us to perform more sophisticated analyses of carbon and calcium cycle dynamics and resulting changes in seawater carbonate chemistry.

2.2 Calcium-only model

The model of *Payne et al.* [2010] consists of a single ocean box. The calcium fluxes to the ocean are river input (F_{riv}), hydrothermal alteration (F_{hyd}), and pore water flux (F_{pw}). Calcium is removed from the ocean via burial of carbonate minerals (F_{carb}). The following

equation describes the change in calcium concentration (M_{Ca}) over time:

$$\frac{dM_{Ca}}{dt} = F_{riv} + F_{hyd} + F_{pw} - F_{carb}. \tag{2.1}$$

Values for F_{riv}, F_{hyd}, and F_{pw} are prescribed (see Table 2.1), while the burial of carbonate is calculated as the square of the ratio between the current ($[\mathrm{Ca}^{2+}]_t$) and steady-sate calcium concentration ($[\mathrm{Ca}^{2+}]_0$):

$$F_{carb} = k_{carb} \times \left(\frac{\left[Ca^{2+}\right]_t}{\left[Ca^{2+}\right]_0} \right)^2 \tag{2.2}$$

where k_{carb} is a scaling constant. It is important to note that this approach assumes a constant carbonate ion concentration. Each of the fluxes has a calcium isotope composition ($\delta^{44}\mathrm{Ca}$) with values presented in Table 2.1. This allows modeling of the changes in $\delta^{44}\mathrm{Ca}_{sw}$ using the following equation:

$$\frac{d(M_{Ca}\delta_{sw})}{dt} = F_{riv} \times (\delta_{riv} - \delta_{sw}) + F_{hyd} \times (\delta_{hyd} - \delta_{sw}) + F_{pw} \times (\delta_{pw} - \delta_{sw}) - F_{carb} \times \varepsilon_{carb} \tag{2.3}$$

where δ_{sw}, δ_{riv}, δ_{hyd}, and δ_{pw} are the $\delta^{44}\mathrm{Ca}$ of seawater, river, hydrothermal input, and pore water fluxes, respectively. ε_{carb} is the fractionation factor between seawater and buried carbonates.

Equations (2.1) and (2.3) are solved numerically by running the model forward in time over 4 million years. In order to replicate the end-Permian acidification scenario, which is the preferred scenario proposed by *Payne et al.* [2010] and *Hinojosa et al.* [2012], the carbonate

burial flux was decreased by 17.7% while simultaneously increasing the riverine input by a factor of 3.3 over 100 ky (Figure 2.2). This was justified by *Payne et al.* [2010] who argued that during ocean acidification the carbonate burial flux decreases and then subsequently increases due to weathering feedbacks. These forcing values were chosen in order to replicate the δ^{44}Ca trend and the duration observed in the sediment record ($\delta^{44}Ca_{carb}$), which suggests a negative excursion of about 0.3‰. Note that 0.3‰ is the full excursion from mean uppermost Permian values of ~ -0.5‰ (Figure 2.1) to the minimum value of about -0.8‰ at the end of extinction horizon. The excursion from $t = 0$ (the extinction horizon) to the minimum value is about 0.2‰, which is used as the target in our LOSCAR simulations.

However, while we recognize the desire for simplicity, there are problems with this approach. First, the shape of the riverine perturbation is not realistic. An abrupt increase in weathering rates, subsequently remaining elevated for 100ky, followed by an instantaneous cessation and recovery back to pre-perturbation levels is very unlikely (Figure 2.2d) as the change in weathering is expected to be more gradual in either direction. Second, the feedback between carbonate burial and [Ca^{2+}] described in equation (2.2) is not used during the perturbation period. The carbonate burial is instead simply prescribed, essentially decoupling inputs and outputs of calcium. Therefore, the only sink of carbonate in this model becomes independent of both riverine fluxes and seawater [Ca^{2+}].

The prescribed reduction in burial was used to simulate acidification (by reducing burial by 17.7% over 100ky), which also contributes to an additional negative excursion in δ^{44}Ca. However, it is important to note that even without this prescribed reduction in burial, the $\delta^{44}Ca_{carb}$ drops by about 0.27‰ due to the increased riverine flux alone (Figure 2.3). In this simulation, the change in carbonate burial (Figure 2.3c) is governed by the change in [Ca^{2+}]

as described in equation (2.2).

Most importantly, the model does not account for changes in $[CO_3^{2-}]$. On the time scale of the perturbation it is essential to account for changes in $[CO_3^{2-}]$ because the compensation e-folding time of the carbonate ion concentration in seawater is about 6,000 to 10,000 years. This means that the response time of carbonate ion is quick relative to a ∼100 ky perturbation. Therefore, on time scales of hundreds of thousands of years it appears unrealistic to decouple the weathering and carbonate burial. For this reason the model presented in *Payne et al.* [2010] has been expanded to account for changes in the carbonate ion concentration of seawater.

2.3 Calcium and carbonate ion model

As explained above, the major shortcoming of the calcium-only model is that it neglects changes in $[CO_3^{2-}]$, which is essential, however, for calculating shallow water carbonate production/deposition. This drawback can be easily rectified by introducing an additional equation to the model tracing $[CO_3^{2-}]$ in the ocean over time, as described in *Zeebe and Westbroek* [2003]:

$$\alpha M_{OC} \frac{d[CO_3^{2-}]}{dt} = F_{rivC} - F_{carb} \tag{2.4}$$

where M_{OC} is the mass of the ocean (1.4×10^{21}kg), α is a factor that accounts for the buffer capacity of seawater ($\alpha \approx 2$), and F_{rivC} is the total CO_3^{2-} input. The α factor takes into account that the dissolution or precipitation of one mole of $CaCO_3$ changes $[CO_3^{2-}]$ by roughly half a mole. The main implicit assumption in eq. (2.4) is that any imbalance between

riverine input of calcium and calcium burial also represents an imbalance of carbon fluxes. In other words, calcium and carbon are weathered/buried in a 1:1 molar ratio. Because this ratio is 1:1, the only way to balance CO_3^{2-} and calcium fluxes in this simple model is to assume that Ca^{2+} and CO_3^{2-} influx are equal ($F_{rivC} = F_{riv} + F_{hyd} + F_{pw}$).

Since now both [CO_3^{2-}] and [Ca^{2+}] are predicted by the model, the carbonate saturation state (Ω) of seawater can be calculated:

$$\Omega = \frac{\left[Ca^{2+}\right]_{sw} \times \left[CO_3^{2-}\right]_{sw}}{K^*_{sp}} \tag{2.5}$$

where $[Ca^{2+}]_{sw}$ and $[CO_3^{2-}]_{sw}$ are the in situ concentration of Ca^{2+} and CO_3^{2-} in seawater, respectively. K^*_{sp} is the solubility product of calcite at the in situ temperature, salinity, and pressure (see Table 2.2). Knowing Ω allows for calculation of precipitation rates of inorganic calcite in shallow water according to [*Caldeira and Rampino*, 1993; *Zeebe and Westbroek*, 2003; *Ridgwell et al.*, 2003; *Rampino and Caldeira*, 2005]:

$$F_{carb} = k_{cr} \times (\Omega - 1)^{\eta} \tag{2.6}$$

where k_{cr} is a rate constant (for values see Table 2.2), set to balance fluxes at the initial steady-state, and η is the order of reaction (set to η=2; see [e.g. *Caldeira and Rampino*, 1993; *Opdyke and Wilkinson*, 1993; *Zeebe and Westbroek*, 2003]).

As pointed out earlier, the $\delta^{44}Ca_{carb}$ in the preferred scenario (Figure 2.2b) of *Payne et al.* [2010] is mostly controlled by the weathering flux rather than acidification. By "turning off" acidification, 90% of the $\delta^{44}Ca_{carb}$ signal is still preserved (Figure 2.3b). Having [CO_3^{2-}] as an additional tracer and the carbonate burial feedback as described above, a new simulation

was performed (Figure 2.4) in order to investigate how the system responds to increased weathering fluxes with a proper burial feedback. In order to demonstrate the significance of $[CO_3^{2-}]$ on $\delta^{44}Ca_{carb}$, a new simulation (Figure 2.4) was run with the same forcing as in Figure 2.3 (F_{riv} increased by 3.3 times over 100ky). Because carbonate burial now depends on the calcite saturation state, the burial flux (Figure 2.4c) responds more quickly to the perturbation and closely follows the shape of the riverine flux (Figure 2.4d). As a consequence, changes in $[Ca^{2+}]$ and $\delta^{44}Ca_{carb}$ are dampened by an order of magnitude when compared to the simulation shown in Figure 2.3. The oceanic calcium concentration changes by only 0.14 μmoles kg^{-1} and the $\delta^{44}Ca_{carb}$ excursion is only about 0.03‰ (about seven times smaller than implied by the data).

The initial $[CO_3^{2-}]$ (180 μmol kg^{-1}) was chosen arbitrarily in order to produce shallow water initially supersaturated with respect to calcite ($\Omega \approx 4$). The actual shallow water concentration of CO_3^{2-} during the end-Permian is unknown but assuming any two components of the ocean CO_2 system it can be calculated [*Zeebe and Wolf-Gladrow*, 2001]. Because there is little or no direct way of knowing any component of the CO_2 system during the end-Permian, the DIC and pH values estimated by the Earth system model described in *Ridgwell* [2005] were used. *Ridgwell* [2005] suggests a DIC concentration of about 4000 μmol kg^{-1} and pH of about 7.7. Note that for the same DIC and $[CO_3^{2-}]$ the Ω calculated in this study (Ω =4) is lower than the one in *Ridgwell* [2005, $\Omega \sim 5.5$]. This is due to the fact that we use a lower $[Ca^{2+}]$ here in order to be consistent with the model results presented in *Payne et al.* [2010].

There is a large uncertainty associated with initial $[CO_3^{2-}]$ and therefore Ω during the studied time period. However, additional model runs (not shown) revealed that the change

in $\delta^{44}Ca_{carb}$ is not very sensitive to the initial $[CO_3^{2-}]$. For example, doubling the initial $[CO_3^{2-}]$ produces a greater negative excursion ($\sim$0.05‰) in $\delta^{44}Ca_{carb}$ but still not nearly enough to explain the observation. According to our simulations and sensitivity studies, it appears that an accelerated weathering event on time scales of hundreds of thousands of years is not capable of producing significant changes in the calcium cycle (i.e. seawater $[Ca^{2+}]$ and Ca isotope ratio).

2.4 LOSCAR Simulations

In order to perform a more sophisticated analysis, we also used an expanded version of the LOSCAR model. A detailed, comprehensive description of the LOSCAR model (Figure S1), its components and architecture is given in *Zeebe* [2012a]. Here, we only describe main modifications made in the model as well as updated boundary conditions, which pertain to the end-Permian. A similar LOSCAR version that includes Ca^{2+} as a tracer was used and described in *Komar and Zeebe* [2011] with the exception that now the model also includes the distribution of stable calcium isotopes (δ^{44}Ca), thus integrating fully coupled carbon and calcium cycles.

The model was modified in order to reflect the changes associated with a mass extinction across the end-Permian. Accordingly, the pre-steady-state pelagic biological $CaCO_3$ rain is set to zero. $CaCO_3$ is precipitated exclusively over the shallow sediment boxes (driven by saturation state; eq.(2.6)), rendering the deep sediments free of calcite, meaning that calcite is accumulated only in shallow waters. The calculated shelf area is $\sim 30 \times 10^6$ km^2, which is approximately equal to the shelf ocean area during the Late Permian [*Osen et al.*, 2013]. The rate of inorganic precipitation of $CaCO_3$ depends on the calcite saturation state, the same

way it does in the simple calcium and carbonate model as described by eq. (2.6).

Model time $t = 0$ corresponds to end-Permian extinction horizon ($\sim$252.6 Ma). The initial atmospheric pCO_2 used in all LOSCAR simulations is set to 850 μatm. This CO_2 concentration is within the range of values reconstructed from proxy records and other modeling studies [*Berner*, 1994; *Royer et al.*, 2004; *Cui and Kump*, 2014] for this time period. The low latitude surface ocean temperature is set to 25^oC [*Sun et al.*, 2012]. Temperature sensitivity to doubling of CO_2 was set to 3^oC. Silicate and carbonate weathering fluxes were set so that the initial cumulative riverine input (14×10^{12} mol yr^{-1}) equals that of the simple calcium model [*Payne et al.*, 2010]. Additionally, for consistency and easier comparison with the simple model, the initial $[Ca^{2+}]$ was set to 10 mmol kg^{-1}, which is in line with the fluid inclusions data for this time period [*Horita et al.*, 2002]. Nevertheless, we tested model sensitivity to different Ca concentrations (see Section 6.1 and Supporting Information). Carbonate and silicate weathering fluxes of calcium are set to the same isotopic value of $-0.6‰$. The model calculates ocean carbonate chemistry parameters (e.g. $[CO_2]$, $[CO_3^{2-}]$, pH) from total carbon and total alkalinity using routines described in *Zeebe and Wolf-Gladrow* [2001]; *Zeebe* [2012a]. These routines allow for variations in the Ca^{2+} concentration of seawater, which is critical for paleo-ocean carbonate chemistry reconstructions. This is important because the concentration of calcium affects the thermodynamics (e.g. equilibrium constants and solubility products), which in turn affects the predicted ocean carbonate chemistry and atmospheric pCO_2.

2.5 Comparison: Simple model vs. LOSCAR

As noted above, both the simple calcium-carbonate ion model and LOSCAR use the same feedback for calculating calcite precipitation, which is governed by eq.(2.6). Nevertheless, the two models produce significantly different results (e.g. compare Figs. 2.4 and 2.5). The core of this discrepancy is the fact that the two models utilize different forcings. The simple calcium model is simply driven by prescribing an increase in riverine flux (simulating accelerated weathering), whereas in LOSCAR the system is perturbed by adding a large amount of carbon to the ocean-atmosphere reservoir. This addition of carbon drives the atmospheric CO_2 upwards. Observations indicate that the increase in pCO_2 (and consequently temperature and precipitation) result in enhanced weathering of carbonate and silicate rocks. In LOSCAR, this is parameterized as:

$$F_{Si} = F^0_{Si} \times \left(\frac{p\mathrm{CO}_2}{p\mathrm{CO}^0_2}\right)^{n_{Si}} \tag{2.7}$$

$$F_C = F^0_C \times \left(\frac{p\mathrm{CO}_2}{p\mathrm{CO}^0_2}\right)^{n_{CC}} \tag{2.8}$$

where F_{Si} and F_C are silicate and carbonate weathering fluxes, respectively, and F^0_{Si} and F^0_C are the same fluxes at time $t = 0$. Similarly, ${\mathrm{pCO}_2}^0$ is the initial ($t = 0$) atmospheric CO_2 concentration, and pCO_2 is the atmospheric partial pressure calculated in the model at time t. n_{Si} and n_{CC} are silicate and carbonate weathering-pCO_2 feedback parameters, respectively, which determine the strength of the feedback. It follows that the carbon introduced into the system will eventually enhance the weathering rates, which is equivalent to increasing the riverine flux in the simple calcium model. Then, why do the two models produce significantly different responses?

In the simple model, the saturation state increases during the prescribed increase in weathering due to increased fluxes of Ca^{2+} and CO_3^{2-} ions, giving stronger saturation-burial feedback (Figure 2.4). Therefore, any imbalance created by accelerated riverine input is quickly restored by enhanced burial resulting in a small change in $[Ca^{2+}]$ and δ^{44}Ca. On the contrary, in LOSCAR, even though there is also an increase in weathering, the calcite saturation response is in the opposite direction (Figure 2.5d) when compared to the simple calcium model. Because LOSCAR includes complete ocean carbonate chemistry, the calcite saturation drops when a large input of carbon is introduced rapidly to the ocean-atmosphere system. As a result of a lower calcite saturation state, the dissolution rate of calcite increases dramatically, so there is essentially no burial. This state of accelerated weathering combined with practically no calcite burial augments the change in $[Ca^{2+}]$ and $\delta^{44}Ca_{carb}$ (Figures 2.5 to 2.7) when compared with the simple calcium model. The augmented change in $[Ca^{2+}]$ and $\delta^{44}Ca_{carb}$ predicted by LOSCAR is a more realistic response of the system. Nevertheless, even when an unrealistic mass of 43,200 Pg C is added to the ocean-atmosphere system over 100ky (the most extreme scenario, Figure 2.7) the change in $\delta^{44}Ca_{carb}$ ($\Delta\delta^{44}Ca \sim 0.15‰$) is still not large enough to explain the observations (change of about 0.2‰ across the extinction horizon [*Payne et al.*, 2010]).

2.6 Alternative hypothesis

The end-Permian extinction event is often associated with the formation of a large igneous province, namely, the Siberian Traps [e.g. *Bowring et al.*, 1998; *Wignall*, 2001; *Kamo et al.*, 2006]. The estimates of volume of basalt that was originally present in the Siberian Traps range from 2 to 4 $\times$ 10^6 km^3 [*Wignall*, 2001; *Lightfoot and Keays*, 2005; *Ivanov et al.*, 2013].

According to *McCartney et al.* [1990], 1 km^3 of basalt emits 5×10^{12} g of C. This translates to 10,000 to 20,000 Pg C that could have been released during the eruption of the Siberian Traps. As we show above, even as much as 40,000 Pg C would not have been enough to produce the desired change observed in $\delta^{44}Ca_{carb}$. Additional LOSCAR runs showed that around 70,000 Pg C of carbon would be necessary to achieve the desired drop of 0.2‰ in $\delta^{44}Ca_{carb}$ across the extinction horizon [*Payne et al.*, 2010]. Also, assuming that the age model used in *Payne et al.* [2010] is correct, then the carbon in the above LOSCAR simulations would have to be released at a much higher rate ($\leq$50ky) in order to better match the observations. In turn, this would raise another issue; such a massive input of carbon would produce large and unrealistic atmospheric CO_2 concentration [10,000 − 20,000 ppm; *Cui and Kump*, 2014]. It would also require a very high rate of carbon input, comparable to present day anthropogenic emissions [*Clarkson et al.*, 2015], which appears difficult to conceive. According to our model, these problems indicate that the eruption of the Siberian Traps cannot alone reconcile all of the trends observed during end-Permian without consideration of additional feedbacks.

Rampino and Caldeira [2005] proposed an alternative mechanism which successfully reproduces the $\delta^{13}C$ and warming trends observed across the end-Permian without volcanic carbon input. They suggest that a drastic decrease in ocean primary productivity ('Strangelove Ocean') was responsible for the observed negative excursion of ∼3‰ (3.6‰ according to *Payne et al.* [2010]), and a consequent rise in pCO_2 was large enough to account for the observed warming of at least 6^oC [*Magaritz and Holser*, 1991; *Sun et al.*, 2012]. The main assumption of *Rampino and Caldeira* [2005] was that the pre end-Permian $\delta^{13}C$ surface to deep gradient in the ocean was considerably greater than today, implying a significantly stronger biological carbon export during that time period when compared with the modern day ocean.

Thus, shutting down the pre end-Permian biological pump (which was active prior to the extinction horizon) ocean results in much greater rise in atmospheric pCO_2, when compared to similar model experiments for the modern ocean, in which pCO_2 increases from 280 μatm to around 500 μatm after turning off biological carbon export.

Here, we perform an experiment in which initial export productivity in LOSCAR was set to approximately twice the modern value, similar to that of *Rampino and Caldeira* [2005], except that in our simulation marine biological export was linearly decreased to zero over the first 50ky, whereas *Rampino and Caldeira* [2005] turn off the biological pump instantaneously. The initial strength of biological carbon export is necessary in order to produce the observed Ca excursion and warming. The linear approach was chosen in order to obtain a better temporal match with the data (assuming that the age model used in *Payne et al.* [2010] is correct). The biological pump was then slowly, linearly returned back to pre-perturbation level over the remainder of the simulation ($\sim$ 350ky). Additionally, *Lemarchand et al.* [2004] showed that in a simple inorganic system, the Ca isotope fractionation between calcite crystals and the mother solution directly depends on $[CO_3^{2-}]$ at which the crystals were precipitated. The regression line showing this dependence was calculated by *Gussone et al.* [2005] and was incorporated into LOSCAR:

$$1000 \cdot ln(\alpha_{cc}) = -(1.31 \pm 0.12) + (3.69 \pm 0.59) \cdot \left[CO_3^{2-}\right](mmol/kg) \tag{2.9}$$

where $1000 \cdot ln(\alpha_{cc})$ is the calcium isotope fractionation between calcium in solution and calcite in ‰. Therefore, fractionation between calcium in seawater and calcium carbonates becomes a function of $[CO_3^{2-}]$ during inorganic precipitation. In other words, the calcium

isotope fractionation becomes larger as $[CO_3^{2-}]$ decreases and vice versa. The valid range of $[CO_3^{2-}]$ is 0 to 350 $\mu mol kg^{-1}$, hence the range of $1000 \cdot ln(\alpha_{cc})$ is -1.31 to 0‰.

Slowing down and eventually turning off the biological carbon pump over 50ky elevates atmospheric pCO_2 via outgassing of CO_2 from the surface ocean (Figure 2.8a). Due to a sudden rise in pCO_2 (governed by Eqs. (2.7) and (2.8)), silicate and carbonate weathering fluxes also increase (Figure 2.8b), which produces a small negative excursion in $\delta^{44}Ca$. The shut down of the biological pump raises the amount of total dissolved carbon in the ocean at a faster rate than the rate of increase of total alkalinity (Figure 2.8c) causing the $[CO_3^{2-}]$ and calcite saturation to drop (Figure 2.8d). According to Eq. (2.9) this will result in a stronger calcium fractionation, which changes from the initial value of -0.92‰ to -1.09‰ (Figure 2.8f), affecting the $\delta^{44}Ca_{carb}$ and causing a larger negative excursion (faster input tempo (25 ky as opposed to 50 ky) of carbon produces only a slightly larger drop in $[CO_3^{2-}]$ and therefore does not affect the change in $\delta^{44}Ca$ significantly). Lower $[CO_3^{2-}]$ then leads to a reduction of shallow water carbonate deposition according to eq. (2.6). Also, 12,000 Pg C with an isotopic composition of -5‰ was added to the ocean-atmosphere system over 50ky in order to reproduce the full 0.2‰ change in $\delta^{44}Ca_{carb}$ (Figure 2.8f). The combination of the carbon input and the shut down of the biological carbon pump leads to an increase of pCO_2 from the initial 850 μatm to $\sim$4000 μatm, which translates into $>6^oC$, warming assuming the canonical value of the fast-feedback sensitivity of 3^oC [*IPCC*, 2007]. This temperate increase is consistent with temperature proxies for the end-Permian [*Magaritz and Holser*, 1991]. The amount of carbon introduced in this simulation (as calculated above) and its isotopic composition [-5‰; *McLean*, 1986; *Kump and Arthur*, 1999] are also in line with the estimates associated with the Siberian Trap volcanism [*Wignall*, 2001; *Lightfoot and Keays*,

2005; *Ivanov et al.*, 2013]. Therefore, we propose the combined effect of the eruption of the Siberian Traps large igneous province, cessation of biological carbon export, and variable calcium isotope fractionation as a plausible mechanism responsible for the trends observed in $\delta^{13}C$, $\delta^{44}Ca$ and temperature across the end-Permian extinction event.

2.6.1 Discussion

It is important to note that the $\delta^{44}Ca$ of seawater and $\delta^{44}Ca$ of carbonate rocks exhibit opposite trends (compared to one another) when the fluctuations are driven by changes in the fractionation factor (if the change in fractionation factor occurs over the time period that is shorter than the residence time of calcium). Therefore, during this transient period, the $\delta^{44}Ca_{carb}$ is not representative of the calcium isotopic composition of seawater [Figure S2; *Fantle*, 2010; *Fantle and Tipper*, 2014]. This is different from the scenario in which fluctuations in $\delta^{44}Ca_{sw}$ are driven by changes in $\delta^{44}Ca$ of the weathering flux (or calcium imbalance between inputs and output fluxes) (Figure S3). Hence, in order to successfully reconstruct the $\delta^{44}Ca$ of the past and gain a better understating of the calcium cycle, it would be necessary to have measurements of at least two distinct phases. One, so called "passive" tracer that would reflect the changes in seawater $\delta^{44}Ca$ and the other, that would constrain the $\delta^{44}Ca$ of buried carbonates [*Fantle and Tipper*, 2014]. *Hinojosa et al.* [2012] made such an attempt by measuring $\delta^{44}Ca$ of hydroxy-apatite conodont microfossils ($\delta^{44}Ca_{conod}$) across the end-Permian ("passive" tracer) complemented with $\delta^{44}Ca$ data of carbonate rock from the same time interval reported by *Payne et al.* [2010] (Figure 2.1). According to *Hinojosa et al.* [2012] the conodont calcium isotope data are representative of the seawater $\delta^{44}Ca$ variability across the end-Permian. The conodont data are offset from seawater value and thus do not

represent the absolute $\delta^{44}Ca_{sw}$ but rather the relative change. Because of rather large error bars, the data had to be statistically analyzed in order to make a meaningful comparison with the model results. A mean of $\delta^{44}Ca_{conod}$ data along with the standard error of the mean before the extinction event was calculated (-0.73 ± 0.03‰) and compared to the mean of the data (-0.83 ± 0.05‰) that mark the isotope excursion (4 data points right after the extinction horizon) (Figures 2.1 and S4). According to the statistical analysis, the change in $\delta^{44}Ca_{conod}$ and therefore a change in $\delta^{44}Ca_{sw}$ could be anywhere between 0.02 to 0.18‰. This was then compared with the $\delta^{44}Ca_{sw}$ evolution predicted by the LOSCAR in our preferred scenario (Figure 2.8 and 2.9). The model calculated $\delta^{44}Ca_{sw}$ has the initial value of 0.32‰ which then exhibits a small negative excursion of about 0.04‰. The LOSCAR predicted change in seawater isotopic composition presented here is therefore also consistent (within errors) with $\delta^{44}Ca_{sw}$ change predicted by the conodont microfossil data.

Additional model runs (Figure S5) were performed in order to test the model sensitivity to: 1) different residence times of calcium in the ocean as the residence time may have been different in the past and 2) different $\delta^{44}Ca$ of the weathering flux as it might have also been different or it could change during the transient perturbation events by less than 0.3‰ [*Fantle and Tipper*, 2014]. The sensitivity runs indicate that neither different residence times of calcium nor a variable $\delta^{44}Ca$ of the weathering flux can significantly impact the model results on time scales of the end-Permian perturbation (see Supporting Information).

2.7 Conclusions

Several previous studies have employed a simple calcium-only model (following *Payne et al.* [2010]) with the attempt to resolve the dynamics and links between carbon and calcium

cycles as well as the cause of the mass extinction during the end-Permian [*Payne et al.*, 2010; *Hinojosa et al.*, 2012] and more recently during the Toarcian oceanic anoxic event (Early Jurassic) [*Brazier et al.*, 2015]. Here, we have identified the deficiencies in such a simplified approach and showed the importance of a fully coupled calcium-carbon cycle model.

The modeling framework presented here successfully reconciles the end-Permian trends in δ^{13}C and δ^{44}Ca recorded in carbonate sediments. The model also predicts a 50 ky rise in atmospheric CO_2 causing a global temperature increase of more than 6^oC. Our model results suggest that the end-Permian mass extinction and the perturbation in carbon-calcium cycling was due to a combination of several factors, including introduction of about 12,000 Pg of carbon through Siberian Trap volcanism, the collapse of ocean primary productivity, and a variable calcium isotope fractionation between seawater and buried carbonates during inorganic precipitation due to changing $[CO_3^{2-}]$. Most importantly, accelerated weathering rates alone that arise due to the perturbation in the carbon cycle are most likely insufficient to directly produce a significant impact on the calcium cycle, contrary to the claims of previous studies.

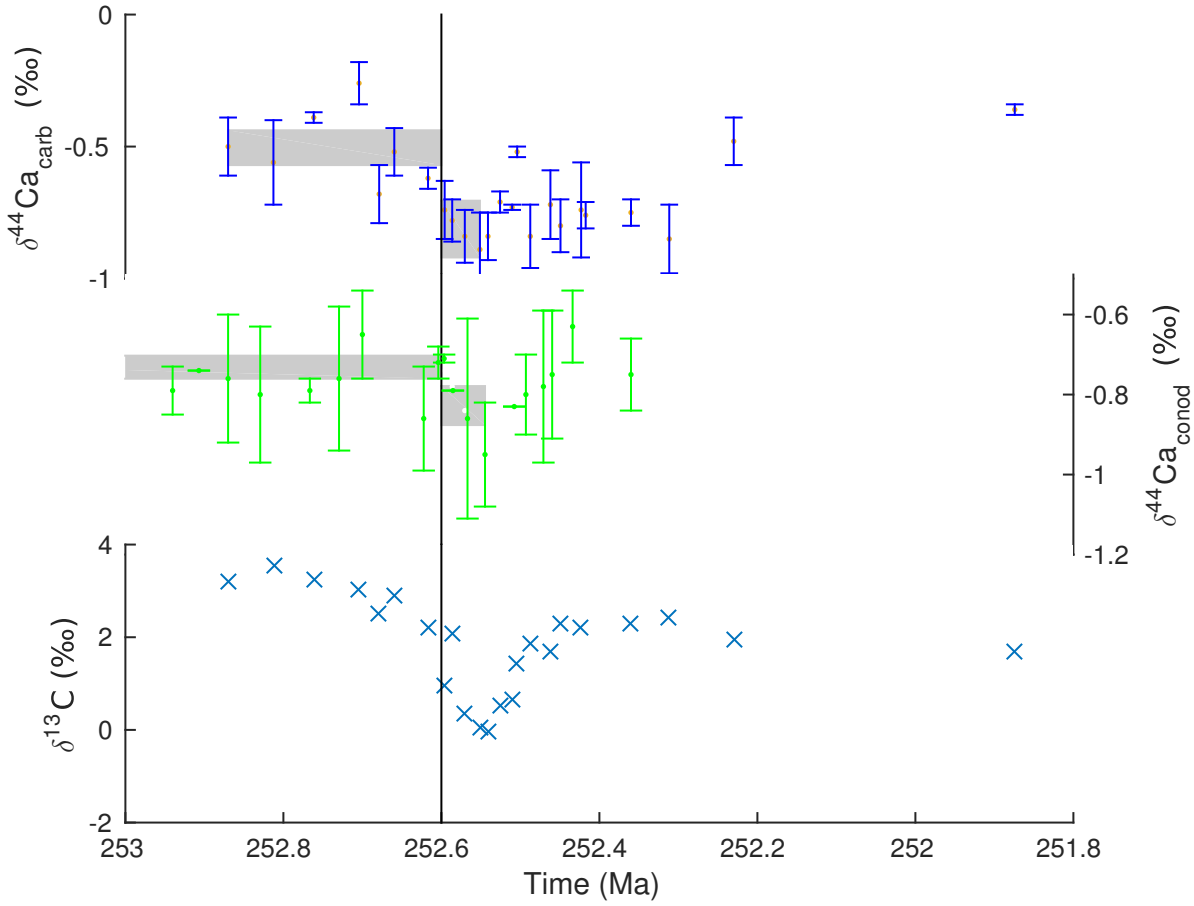

Figure 2.1: Calcium and carbon isotope data across the Permian-Triassic boundary. The black vertical line indicates the extinction horizon [*Payne et al.*, 2010], which corresponds to t=0 in LOSCAR simulations. $\delta^{44}Ca_{carb}$ and $\delta^{13}C_{carb}$ are calcium and carbon isotopic data, respectively, from marine limestone in south china reported by *Payne et al.* [2010]. $\delta^{44}Ca_{conod}$ is δ^{44}Ca of hydroxy-apatite conodont microfossils measured by *Hinojosa et al.* [2012], which are indicative of seawater δ^{44}Ca (see Section 6.1). δ^{44}Ca ($\delta^{44/40}Ca$) values are normalized to a bulk Earth standard. The gray bands show the standard error of the mean within 95% confidence interval ($2S_e$) for period before the extinction horizon ($\delta^{13}C_{carb}$: -0.5 ± 0.07‰, $\delta^{44}Ca_{conod}$: -0.73 ± 0.03‰) and during the isotope excursion ($\delta^{13}C_{carb}$: -0.81 ± 0.11‰, $\delta^{44}Ca_{conod}$: -0.83 ± 0.05‰).

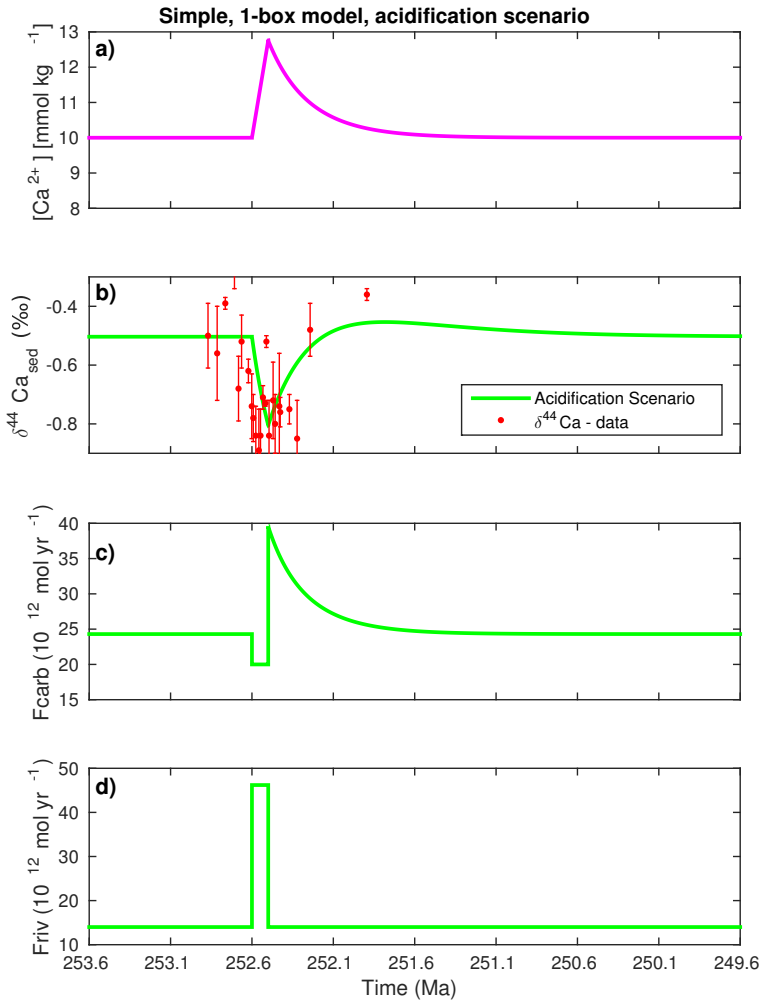

Figure 2.2: Accelerated weathering and reduced burial simulation. This is the preferred scenario of *Payne et al.* [2010]. The model was forced by enhancing the riverine flux by a factor of 3.3 times the initial value over 100 ky while at the same time reducing carbonate burial by 17.7%. (a) Calcium ion concentration. (b) Calcium isotope response of buried carbonates. (c) Carbonate burial flux. (d) Riverine flux of calcium.

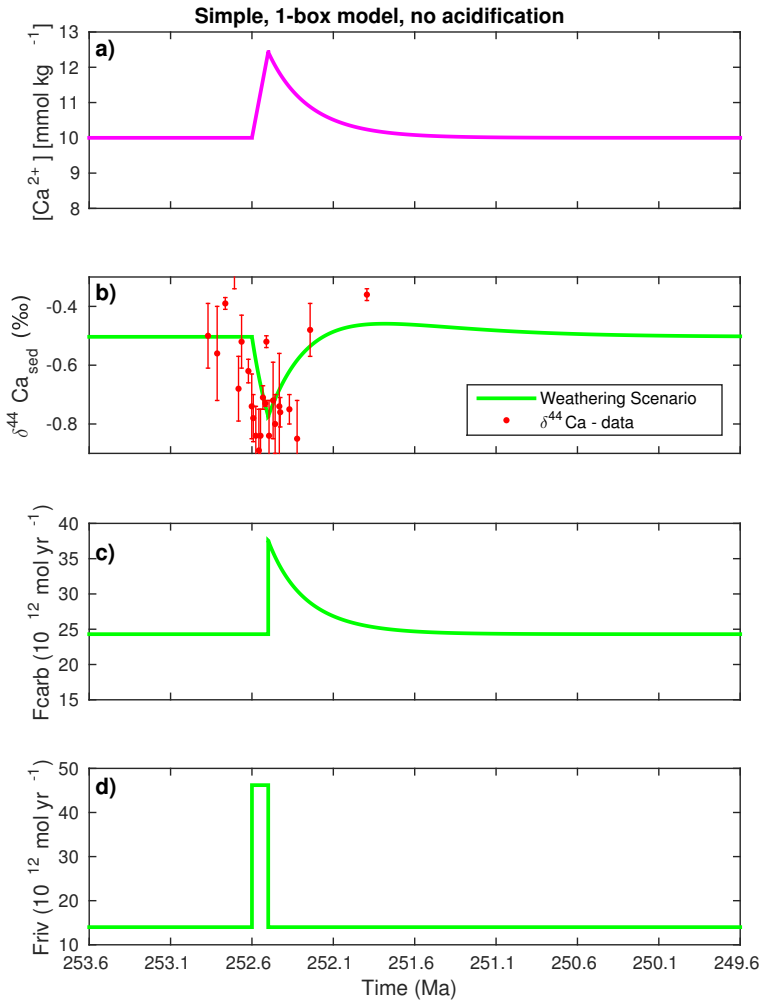

Figure 2.3: Accelerated weathering only scenario (no reduced burial). The riverine forcing used is the same as in Fig 2.2. (a) Calcium ion concentration. (b) Calcium isotope response of buried carbonates. (c) Carbonate burial flux. (d) Riverine flux of calcium.

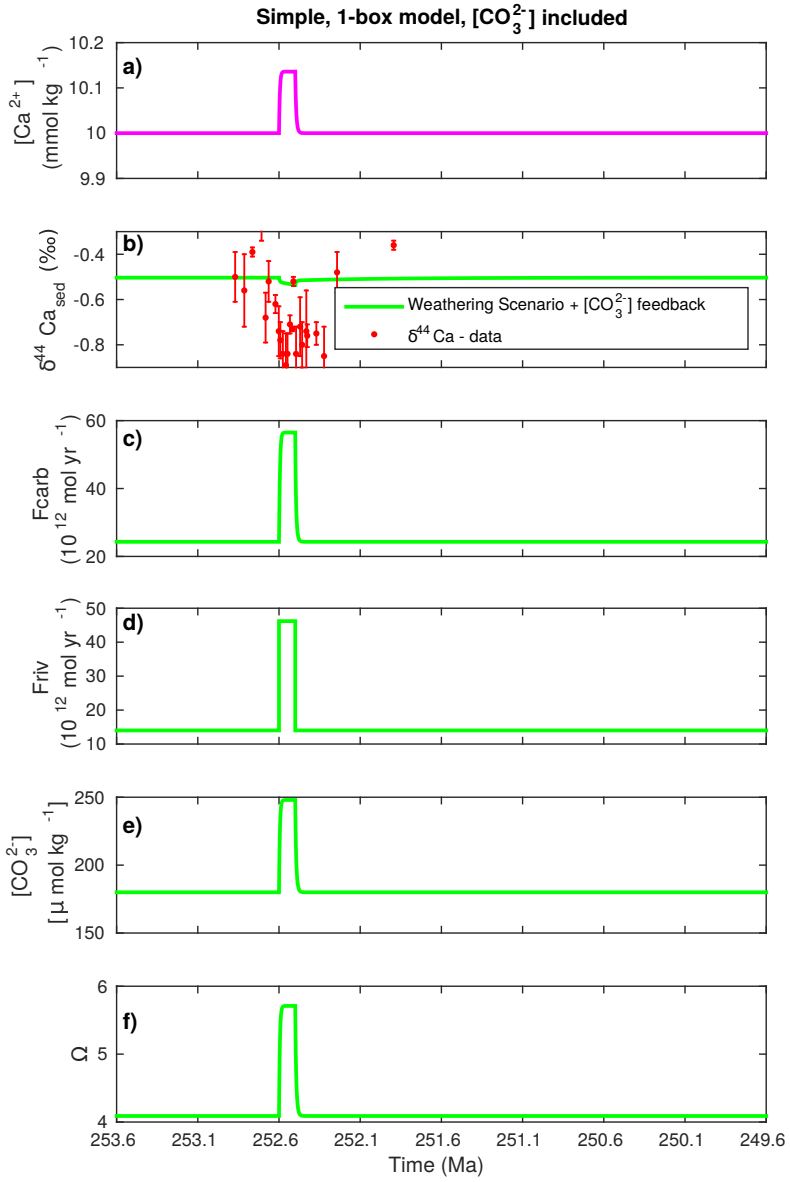

Figure 2.4: Model results using the calcite saturation state (Ω) in the carbonate weathering feedback. The riverine forcing used is the same as in Figures 2.2 and 2.3. (a) Calcium ion concentration. (b) Calcium isotope response of buried carbonates. (c) Carbonate burial flux. (d) Riverine flux of calcium. (e) Carbonate ion concentration. (f) Calcite saturation state.

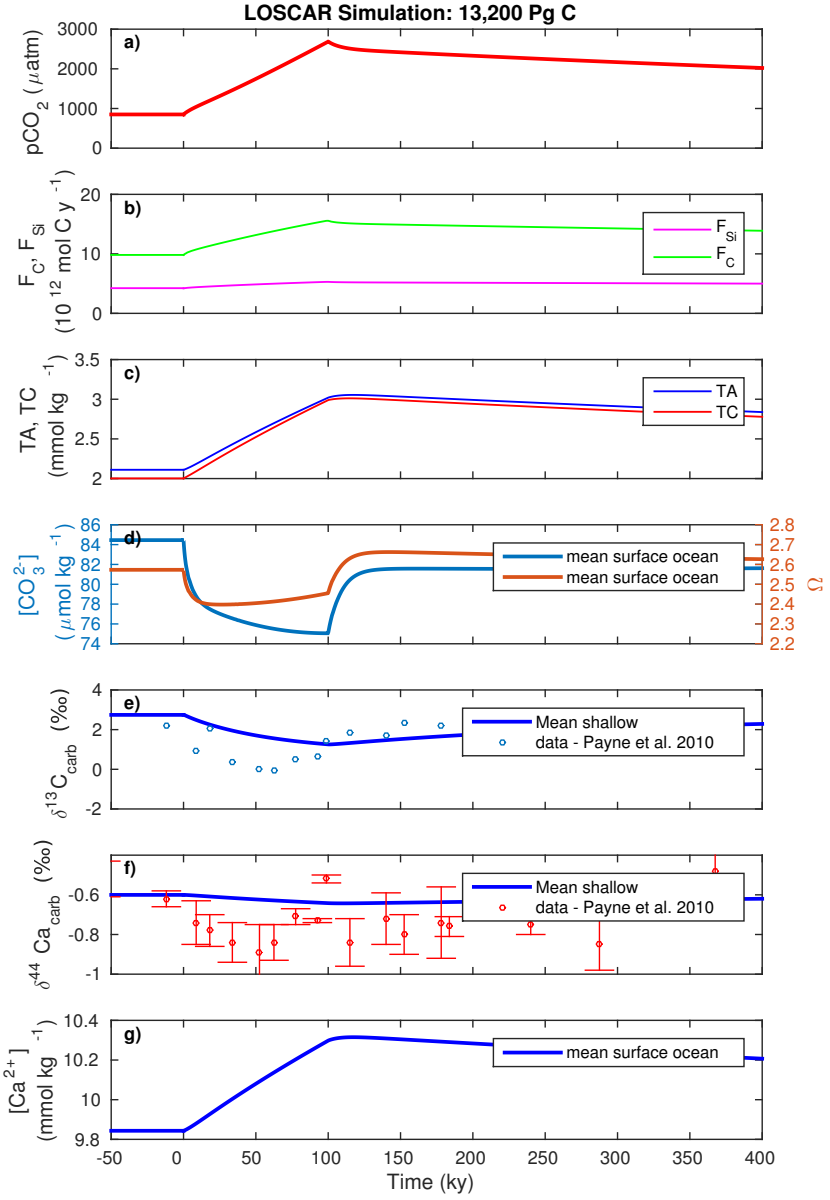

Figure 2.5: Forcing: 13,200 Pg C over 100ky (lower estimate proposed by *Payne et al.* [2010]). Weathering feedback parameters: n_{CC}=0.4, n_{Si}=0.2. a) predicted atmospheric CO_2, b) Carbonate and Silicate weathering fluxes (initial F_C and F_{Si} equal 9.8 and 4.2×10^{12} mol C y^{-1}, respectively), c) Total Alkalinity and Total Dissolved Carbon, d) Mean surface ocean $[CO_3^{2-}]$ and calcite saturation, e) Mean $\delta^{13}C$ of shallow sediments, f) Mean $\delta^{44}Ca$ of shallow sediments, g) Mean $[Ca^{2+}]$ of surface ocean.

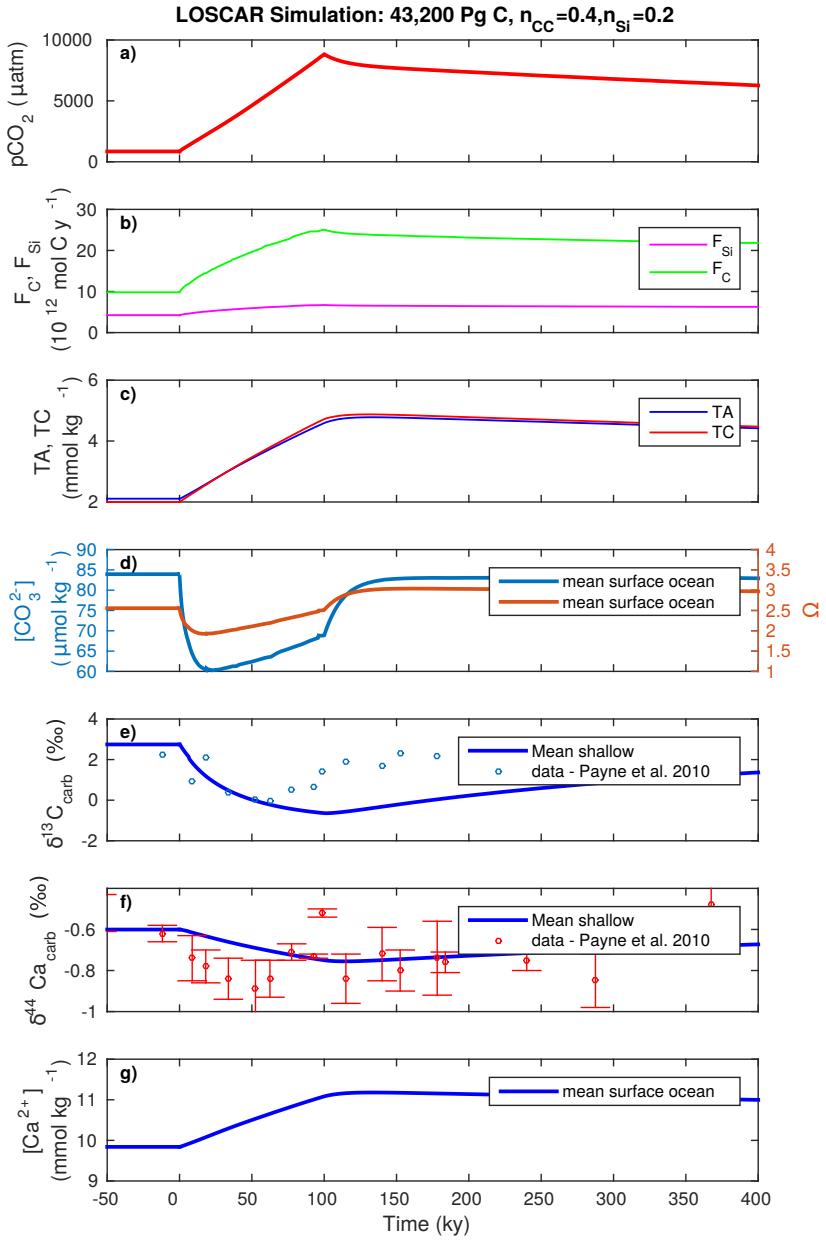

Figure 2.6: Forcing: 43,200 Pg C over 100ky (upper estimate proposed by *Payne et al.* [2010]). Weathering feedback parameters: n_{CC}=0.4, n_{Si}=0.2. a) predicted atmospheric CO_2, b) Carbonate and Silicate weathering fluxes (initial F_C and F_{Si} equal 9.8 and 4.2×10^{12} mol C y^{-1}, respectively), c) Total Alkalinity and Total Dissolved Carbon, d) Mean surface ocean $[CO_3^{2-}]$ and calcite saturation, e) Mean $\delta^{13}C$ of shallow sediments, f) Mean $\delta^{44}Ca$ of shallow sediments, g) Mean $[Ca^{2+}]$ of surface ocean.

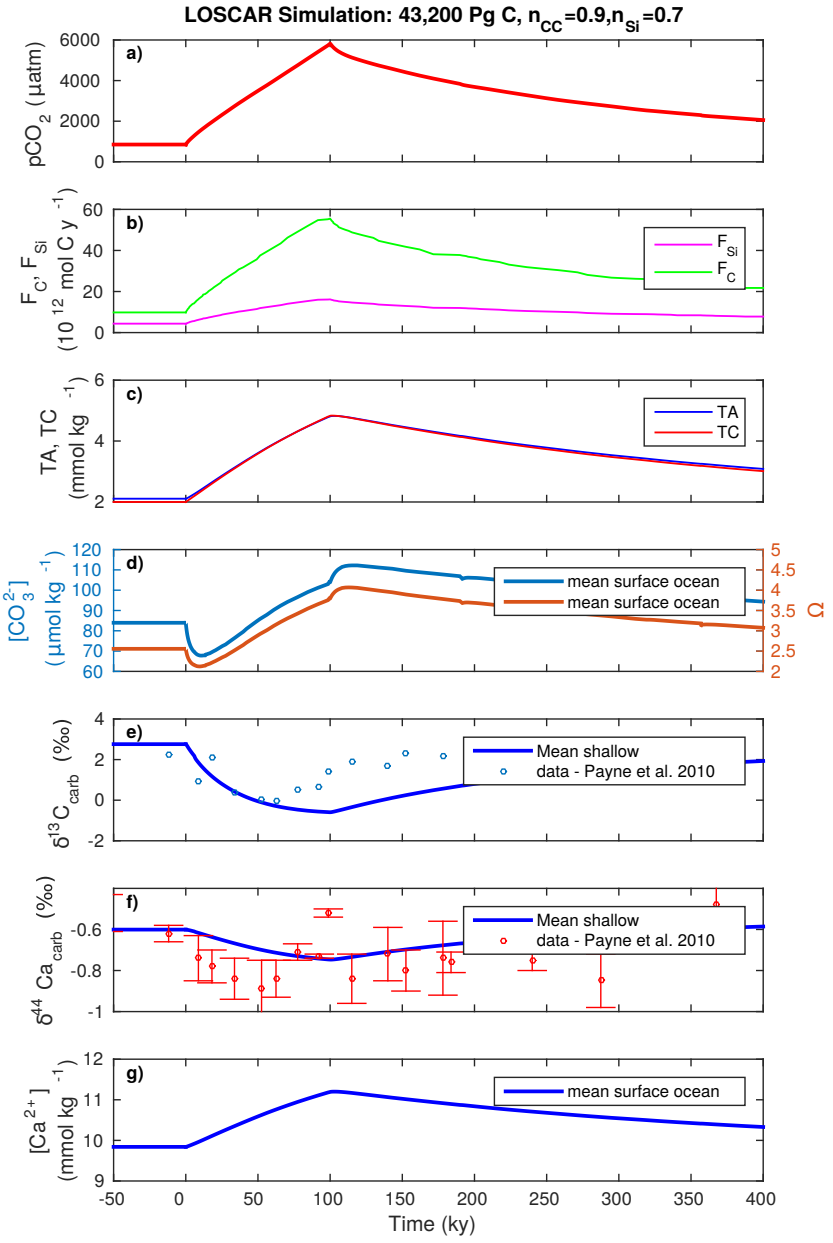

Figure 2.7: Forcing: 43,200 Pg C over 100ky (upper estimate proposed by *Payne et al.* [2010]). Weathering feedback parameters: n_{CC}=0.9, n_{Si}=0.7 (stronger feedback in order to get the same absolute increase in riverine fluxes as in *Payne et al.* [2010]). a) predicted atmospheric CO_2, b) Carbonate and Silicate weathering fluxes (initial F_C and F_{Si} equal 9.8 and 4.2×10^{12} mol C y^{-1}, respectively), c) Total Alkalinity and Total Dissolved Carbon, d) Mean surface ocean $[CO_3^{2-}]$ and calcite saturation, e) Mean $\delta^{13}C$ of shallow sediments, f) Mean $\delta^{44}Ca$ of shallow sediments, g) Mean $[Ca^{2+}]$ of surface ocean.

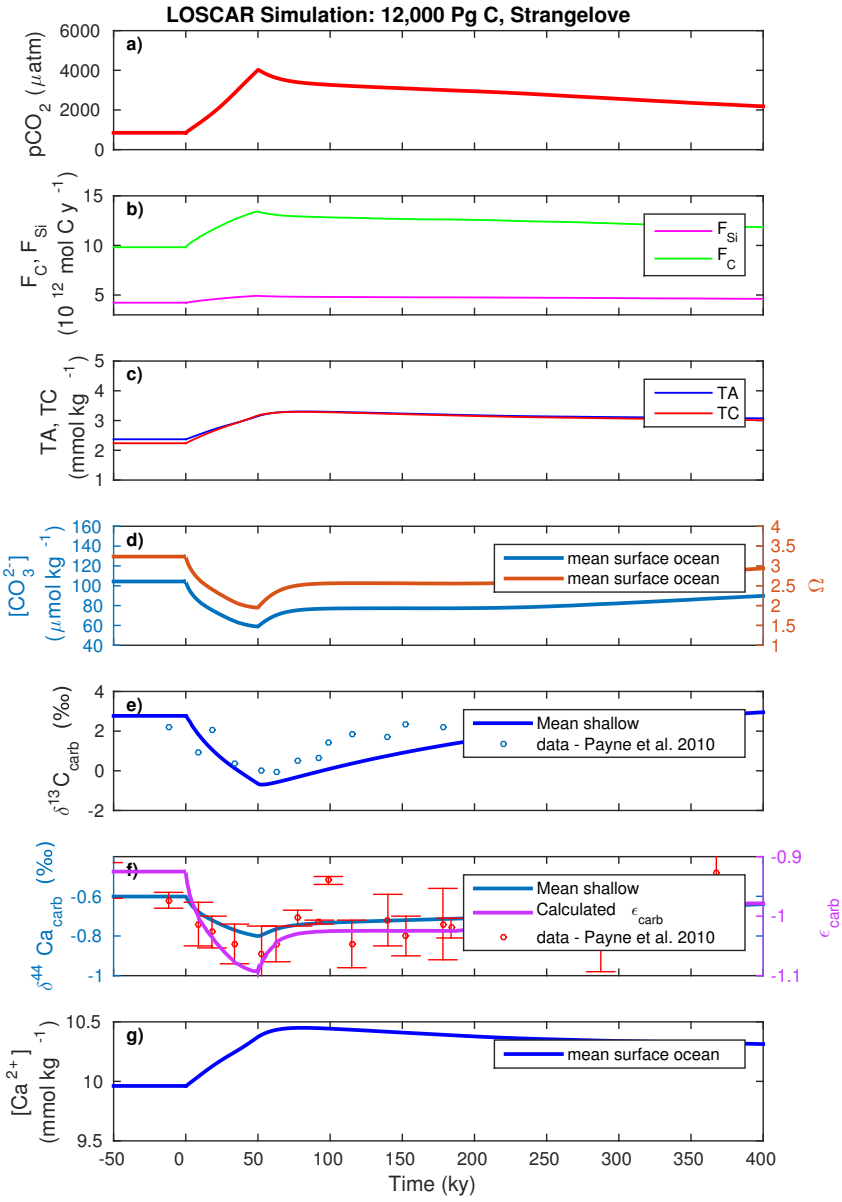

Figure 2.8: Simulation including Strangelove Ocean, C input (12 000 Pg), and variable calcium isotope fractionation (eq. (2.9)). Weathering feedback parameters: n_{CC}=0.2, n_{Si}=0.1. a) predicted atmospheric CO_2, b) Carbonate and Silicate weathering fluxes (initial F_C and F_{Si} equal 9.8 and 4.2×10^{12} mol C y^{-1}, respectively), c) Total Alkalinity and Total Dissolved Carbon, d) Mean surface ocean $[CO_3^{2-}]$ and calcite saturation, e) Mean $\delta^{13}C$ of shallow sediments, f) Mean $\delta^{44}Ca$ of shallow sediments and calculated calcium isotope fractionation based on Eq.(2.9), g) Mean $[Ca^{2+}]$ of surface ocean.

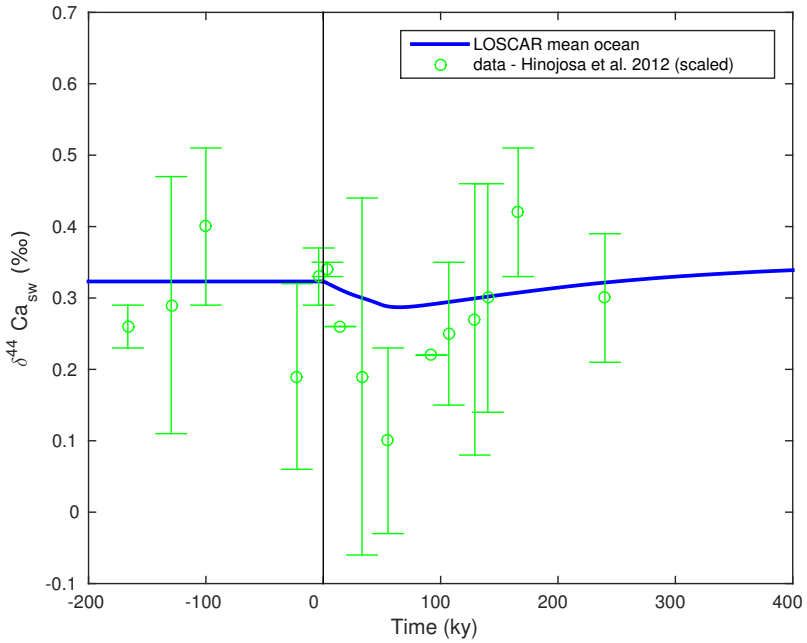

Figure 2.9: Evolution of δ^{44}Ca of seawater in LOSCAR for the simulation shown in Figure 2.8. Vertical black line marks the end-Permian extinction horizon. Open green circles are data from *Hinojosa et al.* [2012], shown in Figure 2.1, scaled to the model output by adding 1.05‰ to the measured values, so that the mean value of the pre extinction data matches the pre-extinction value (0.32‰) of the model (see Section 6.1). The conodont data are offset from seawater value and thus do not represent the absolute $\delta^{44}Ca_{sw}$ but rather the relative change.

Table 2.1: Parameter values used in the model. δ^{44}Ca values are normalized to a bulk Earth standard.

Parameter	Value	Unit	References
$\left[Ca^{2+}\right]_0$	10	mmol kg^{-1}	*Horita et al.* [2002]
F_{riv}	14	10^{12} mol Ca yr^{-1}	*Pilson* [2012]
F_{hyd}	4	10^{12} mol Ca yr^{-1}	*Elderfield and Schultz* [1996]
F_{pw}	6.3	10^{12} mol Ca yr^{-1}	*Pilson* [2012]
k_{carb}	24.3	10^{12} mol Ca yr^{-1}	calculated to balance fluxes
F_{carb}	see eq. (2.2)	10^{12} mol Ca yr^{-1}	*Payne et al.* [2010]
δ_{sw}	0.9	‰	Steady-state value with $\varepsilon = 1.4$‰
δ_{riv}	-0.6	‰	Assumes that carbonate weathering is predominant source of Ca [*Fantle and Tipper*, 2014]
δ_{hyd}	-0.25	‰	*Amini et al.* [2008]
δ_{pw}	-0.45	‰	*Payne et al.* [2010]
ε_{carb}	-1.4	‰	*Fantle and DePaolo* [2007]

Table 2.2: Additional parameters used in the expanded calcium model, which accounts for the change in [CO_3^{2-}] and calcite saturation state.

Parameter	Value and unit	Notes
Temperature	20°C	
Salinity	35	
Pressure	15 bar	shallow ocean
K^*_{sp}	4.4×10^{-7}	based on T, S, P and initial [Mg^{2+}] and [Ca^{2+}]
k_{cr}	10.8 $\times10^{12}$ mol yr^{-1}	calculated to balance fluxes
$[CO_3^{2-}]_0$	180 μmoles kg^{-1}	arbitrary, see text
Ω_0	4	calculated initial calcite saturation state

2.8 Supporting Information for "Calcium and calcium isotope changes during carbon cycle perturbations at the end-Permian"

Contents of this file

1. Text S1
2. Text S2
3. Figure 2.10
4. Figure 2.11
5. Figure 2.12
6. Figure 2.13
7. Figure 2.14

Introduction This supporting information provides a more detailed description of the LOSCAR model mentioned in the main article as well as its schematic representation. It also gives an array of sensitivity simulations and statistical analysis of the data, as mentioned in the manuscript.

Text S1. LOSCAR is designed to efficiently compute the partitioning of carbon between ocean, atmosphere, and sediments on time scales ranging from centuries to millions of years. LOSCAR includes various biogeochemical tracers such as total dissolved inorganic carbon (TCO_2), total alkalinity (TA), Calcium (Ca), phosphate (PO_4), oxygen (O_2), stable carbon isotopes ($\delta^{13}C$), stable calcium isotopes ($\delta^{44}Ca$) and $CaCO_3$ in sediments. Based on the

predicted tracer distributions, different variables are computed including atmospheric CO_2, ocean pH, calcite and aragonite saturation state, calcite compensation depth (CCD) and more [*Zeebe*, 2012a]. LOSCAR also allows for changes in the major ion composition of seawater, including the seawater Mg/Ca ratio, which is critical for paleo-applications. The major ion seawater composition affects thermodynamic quantities such as equilibrium constants and solubility products, which in turn affect the predicted ocean carbonate chemistry and atmospheric CO_2.

LOSCAR's main components include ocean, atmosphere, and marine sediments. The global ocean is geometrically divided in LOSCAR into separate ocean basins representing Atlantic, Indian, and Pacific Ocean (plus Tethys in the paleo-version). In turn, each ocean basin is subdivided into surface, intermediate, and deep ocean (Fig. S1). In addition, the model includes a generic high-latitude box (H-box), representing cold surface waters without reference to a specific location. As a result, the total number of ocean boxes is NB = 10 in the modern version and NB = 13 in the paleo-version. To find more details about architecture, main components, model variables, and process parameterizations visit `http://www.soest.hawaii.edu/oceanography/faculty/zeebe_files/LoscarModel.html`

Text S2. As mentioned in the manuscript, a result of variable calcium isotopic fractionation is a distinct evolution of $\delta^{44}Ca_{sw}$ and $\delta^{44}Ca_{carb}$. To demonstrate this, we prescribe a linear increase in isotopic fractionation of calcium in LOSCAR of 0.5‰ over 50ky (from the initial ~ -0.9 to ~ -1.4‰) after which the fractionation is kept constant at ~ -1.4‰ (Figure 2.11a). As a consequence of increased fractionation, lighter calcium isotope (^{40}Ca) is preferentially buried in the sediments, while heavier isotope (^{44}Ca) is left behind, enriching the ocean water (Figure 2.11b). During the transient, perturbation period (over the first 50ky), $\delta^{44}Ca_{sw}$ trend

is in the opposite direction when compared to the $\delta^{44}Ca_{carb}$ trend (Figure 2.11c). On the other hand, if the fluctuations are driven by changing the $\delta^{44}Ca$ of the the weathering flux (Figure 2.12a), then the trend in $\delta^{44}Ca_{carb}$ (Figure 2.12c) is mimicked by the change in $\delta^{44}Ca_{sw}$ (Figure 2.12b). This mechanism was originally described in *Fantle* [2010] and *Fantle and Tipper* [2014], addressing the importance of using a proxy material that is a "passive" tracer of seawater $\delta^{44}Ca_{sw}$, which reflects $\delta^{44}Ca_{sw}$ + offset between the tracer and $\delta^{44}Ca_{sw}$, when reconstructing seawater calcium isotope evolution driven by a change in fractionation factor.

Calcium isotope trends of seawater in simulations other than our preferred scenario are not shown. In these simulations, the $\delta^{44}Ca_{carb}$ and $\delta^{44}Ca_{sw}$ are driven solely by Ca mass imbalances between the input and output fluxes and therefore the $\delta^{44}Ca$ of seawater mimics that of $\delta^{44}Ca$ of carbonates. The relative change of the two is the same, it is only offset by the fractionation factor. However, in our alternative scenario (Figure 8), the change in $\delta^{44}Ca$ of both seawater and carbonates is a combined effect of variable fractionation and Ca mass flux imbalance and therefore exhibits different and a more complex behavior. A stronger isotope fractionation caused by a change in $[CO_3^{2-}]$ drives the $\delta^{44}Ca_{sw}$ towards heavier values while at the same time accelerated weathering forces $\delta^{44}Ca_{sw}$ in the opposite direction, towards lighter values. The combined result is a slight negative excursion of about 0.04‰ (Figure 9). In order to compare modeled excursion of $\delta^{44}Ca_{sw}$ with the $\delta^{44}Ca_{conod}$, the conodont data had to be statistically analyzed. We calculated mean of the pre-extinction event conodont microfossil data to be -0.73‰, with the standard error of the mean within the 95% confidence interval to be 0.03‰ (total of 13 data points) (Figure 2.13 marked in green). The mean value of the data that marks the negative excursion (total of 4 data points right after the extinction

horizon) is −0.83‰ with the standard error of the mean of 0.05‰ (Figure 2.13 marked in red). Therefore, the mean negative excursion is −0.1‰, with a possible range of 0.02‰ to 0.18‰. For easier comparison, the data were then scaled by +1.05‰ so that the model calculated pre-extinction $\delta^{44}Ca_{sw}$ matches the mean $\delta^{44}Ca_{conod}$ for the same time period.

Because the residence time of calcium in the ocean might have changed in the past and changes in the biosphere can influence the isotopic composition of riverine flux of calcium by up to 0.3‰ [*Fantle and Tipper*, 2014], additional LOSCAR sensitivity analyses were performed and displayed in Figure 2.14. Blue line in Figure 2.14a is the evolution of carbonate rock δ^{44}Ca displayed in Figure 8, which is our preferred scenario (marked by word "standard" in the parentheses). The residence time of calcium (τ_{Ca}) in the standard run is about 1 Ma, with Ca concentration of 10 mmol kg^{-1}. Sensitivity of $\delta^{44}Ca_{carb}$ was then tested by doubling and halving the residence time of Ca in the ocean, attained by increasing the Ca concentration to 20 mmol kg^{-1} and reducing it to 5 mmol kg^{-1}, black and green lines, respectively. In standard run, isotopic fractionation is governed by $[CO_3^{2-}]$, which goes from the initial value of −0.92‰ to the maximum of −1.09‰ (total change of 0.17‰). In order to only test for the effects of different residence times on $\delta^{44}Ca_{carb}$, the fractionation factor in sensitivity runs was independent of $[CO_3^{2-}]$. It was rather prescribed, so that the relative maximum change in the fractionation factor in all three simulation was the same (0.17‰ between t=0 and t=50ky). The $\delta^{44}Ca_{carb}$ in the standard run exhibits a negative excursion of 0.2‰. Simulation with a doubled residence time displays a slightly smaller negative excursion (about 0.18‰), which is primarily due to a larger calcium reservoir and therefore the changes in $\delta^{44}Ca_{carb}$ are dampened. Likewise, shorter than standard residence time simulation exhibits an insignificantly more pronounced negative excursion (0.21‰) due to a smaller calcium

reservoir compared to the standard run.

Next, we tested for the effects of different δ^{44}Ca of the weathering flux (Figure 2.14b). Again, blue line represent the preferred scenario with (τ_{Ca}) of 1 Ma. Black line is the result of abruptly changing the standard initial δ^{44}Ca from -0.6‰ to -0.3‰ over the first 50ky of the simulation, after which it was returned back to the initial value. Because now the input flux of calcium is isotopically slightly heavier compared to standard run, the change in $\delta^{44}\text{Ca}_{carb}$ is reduced and equals 0.18‰. On the other hand, changing the standard initial δ^{44}Ca from -0.6‰ to -0.9‰ over the first 50ky results in a slightly amplified response of $\delta^{44}\text{Ca}_{carb}$, which changes by 0.22‰ (green line Figure 2.14b).

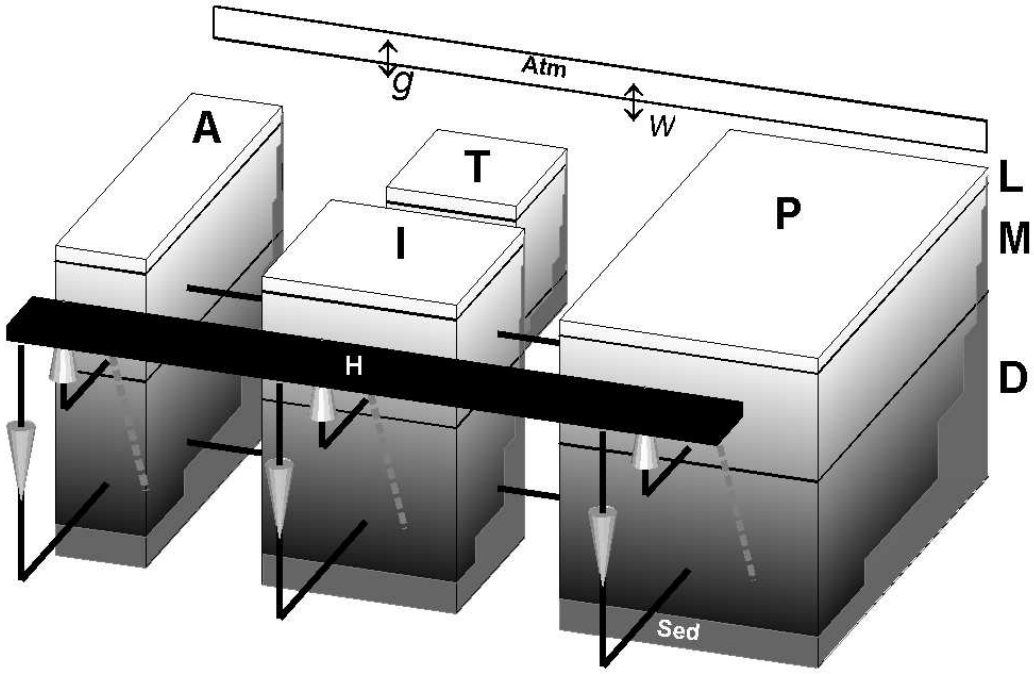

Figure 2.10: Schematic representation of the LOSCAR model (Paleocene/Eocene configuration). A = Atlantic, I = Indian, P = Pacific, T = Tethys ocean, H = High-latitude surface, L = Low-latitude surface, M = interMediate, D = Deep box. Weathering fluxes and gas exchange with the atmosphere (Atm) are indicated by "w" and "g", respectively. Steps on the faces of ocean boxes indicate sediments (Sed).

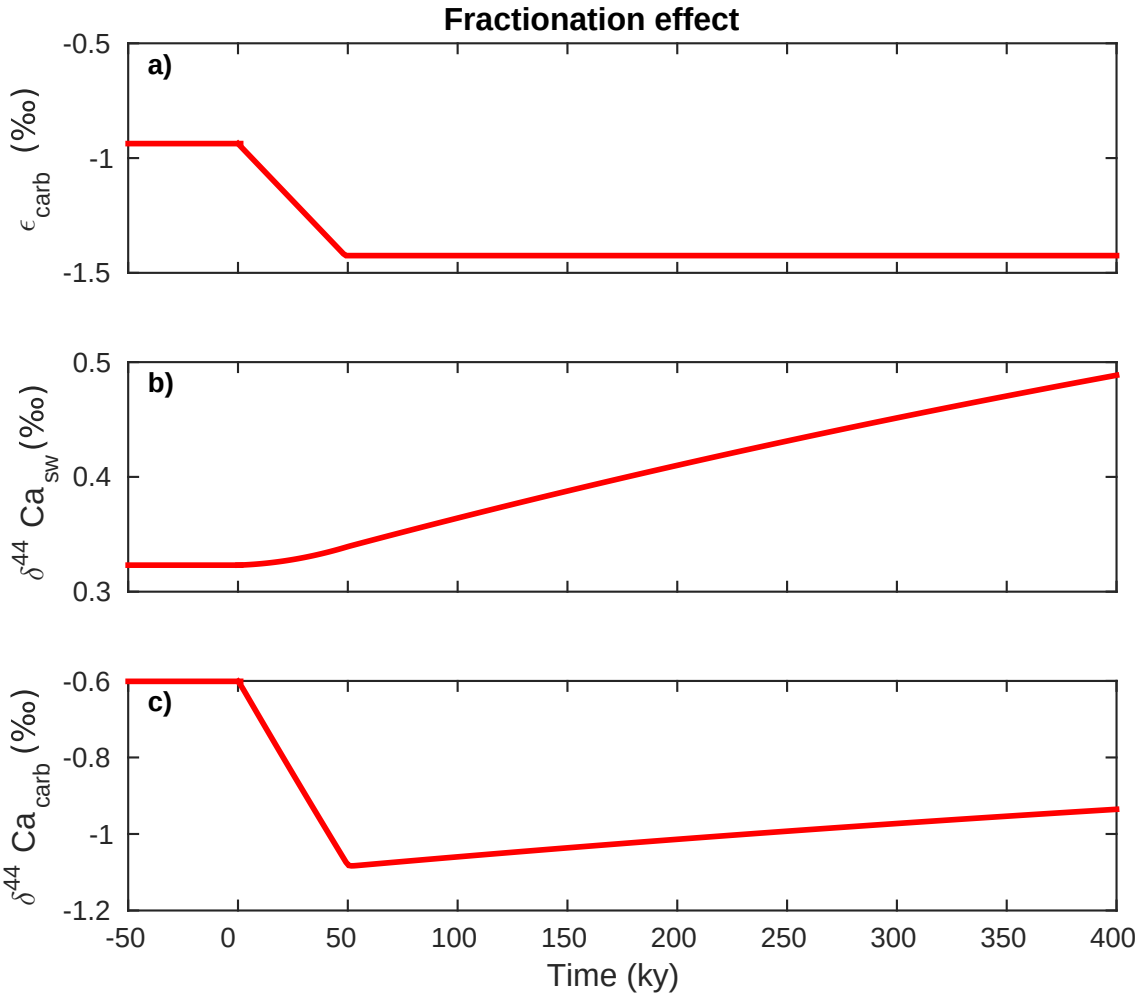

Figure 2.11: The effect of changing the global fractionation factor (ε_{carb}) on the $\delta^{44}Ca_{sw}$ and on the $\delta^{44}Ca_{carb}$. a) Prescribed change in calcium fractionation factor, b) response of the $\delta^{44}Ca_{sw}$ to the change in ε_{carb}, c) response of the $\delta^{44}Ca_{carb}$ to the change in ε_{carb}.

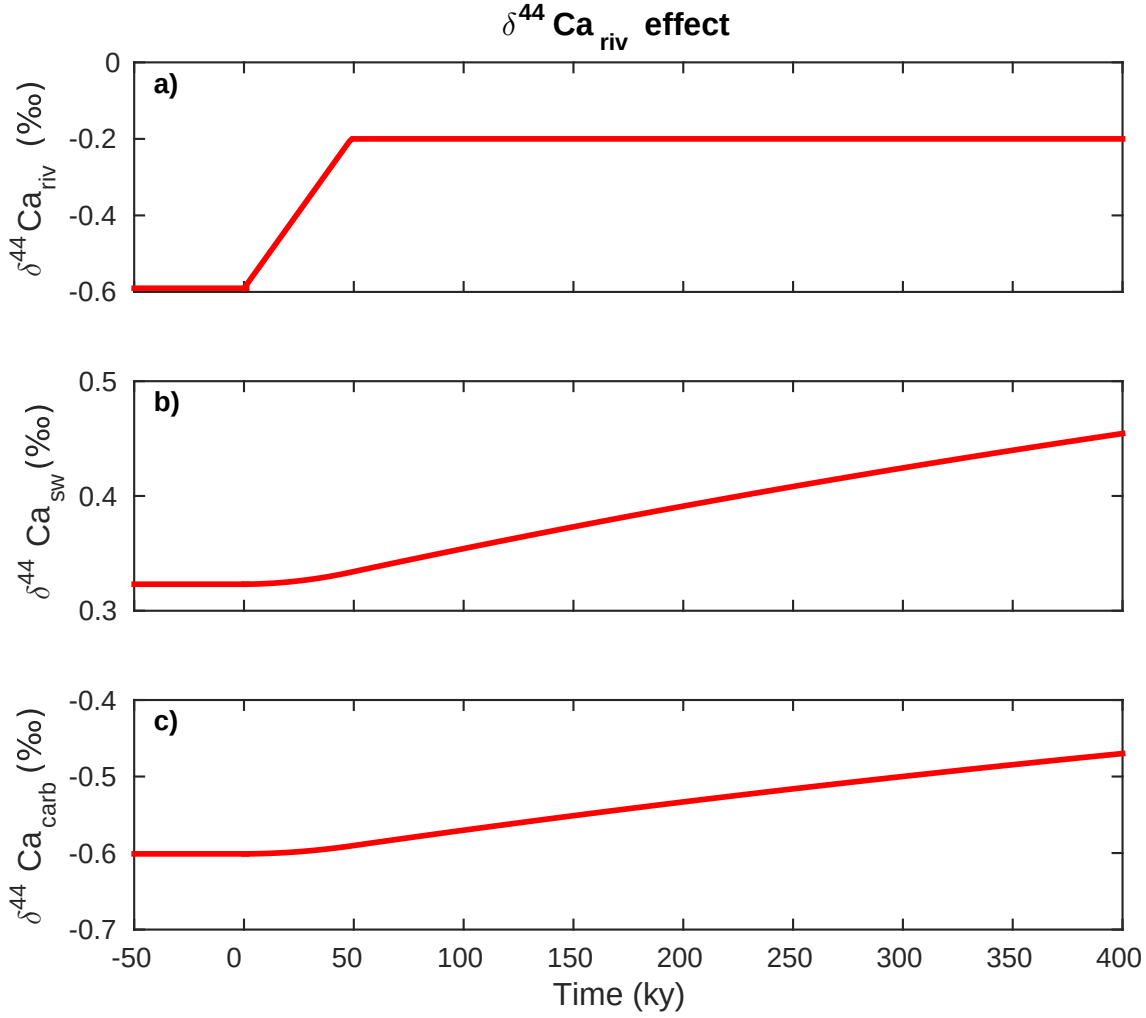

Figure 2.12: The effect of changing the isotopic composition of the input flux ($\delta^{44}Ca_{riv}$ - combined carbonate and silicate flux) of calcium on the $\delta^{44}Ca_{sw}$ and the $\delta^{44}Ca_{carb}$.

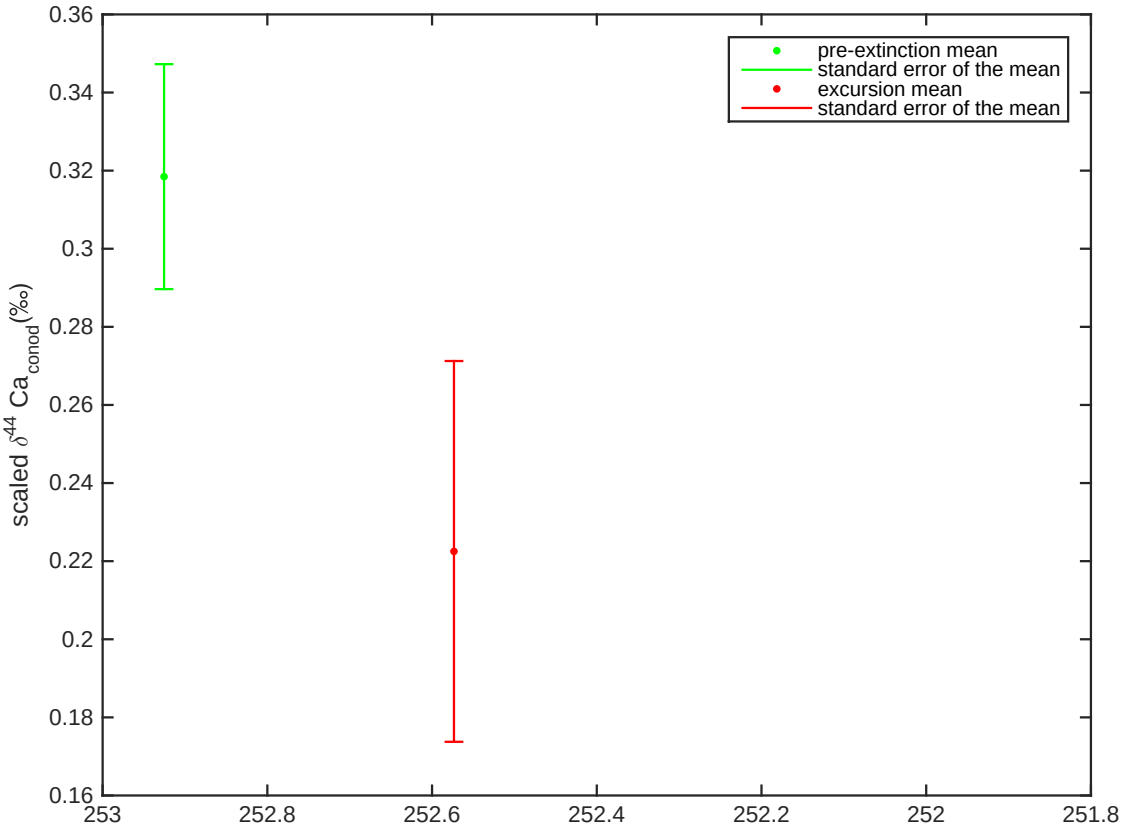

Figure 2.13: Mean of all data points preceding the extinction horizon and their standard error of the mean (green) compared to the mean of the 4 data points that mark the negative excursion just after the extinction horizon and their standard error of the mean (red).

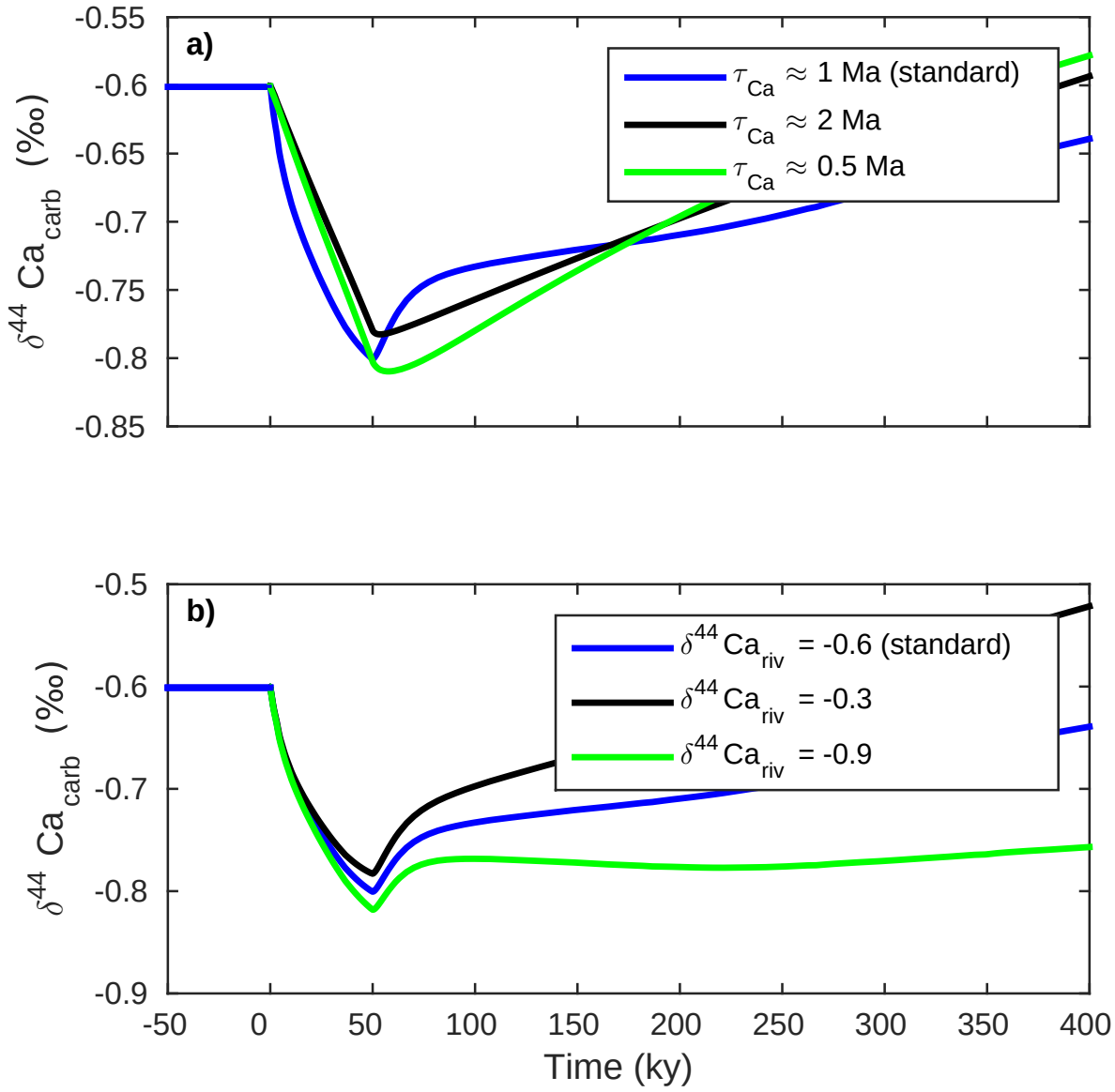

Figure 2.14: Additional LOSCAR results and sensitivity runs. a) Model sensitivity to different residence times of calcium τ_{Ca} in the ocean. The blue line is our standard, preferred scenario shown in Figure 8. In order to attain different residence time, the initial ocean calcium concentration was doubled and halved, black and green lines, respectively. b) Model sensitivity to different δ^{44}Ca of the weathering flux. Blue line is the standard model output of our preferred scenario (Figure 8). Black and green lines are results of a 0.3‰ heavier or lighter input flux, respectively.

CHAPTER 3
REDOX-CONTROLLED CARBON AND PHOSPHORUS BURIAL: A MECHANISM FOR ENHANCED ORGANIC CARBON SEQUESTRATION DURING THE PETM

Published in Earth and Planetary Science Letters

Komar, N., and R. E. Zeebe (2017), Redox-controlled carbon and phosphorus burial: A mechanism for enhanced organic carbon sequestration during the PETM, Earth and Planetary Science Letters, 479, 71-82, doi:10.1016/j.epsl.2017.09.011.

ABSTRACT

Geological records reveal a major perturbation in carbon cycling during the Paleocene-Eocene Thermal Maximum (PETM, ∼56 Ma), marked by global warming of more than 5^{o}C and a prominent negative carbon isotope excursion of at least 2.5‰ within the marine realm. The entire event lasted about 200,000 years and was associated with a massive release of light carbon into the ocean-atmosphere system over several thousands of years. Here we focus on the terminal stage of the PETM, during which the ocean-atmosphere system rapidly recovered from the carbon cycle perturbation. We employ a carbon-cycle box model to examine the feedbacks between surface ocean biological production, carbon, oxygen, phosphorus, and carbonate chemistry during massive CO_2 release events, such as the PETM. The model results indicate that the redox-controlled carbon-phosphorus feedback is capable of producing enhanced organic carbon sequestration during large carbon emission events. The locale of carbon oxidation (ocean vs. atmosphere) does not affect the amount of carbon sequestered. However, even though the model produces trends consistent with oxygen, excess accumulation rates of organic carbon (∼1700 Pg C during the recovery stage), export production and δ^{13}C data, it fails to reproduce the magnitude of change of sediment carbonate content and the CCD deepening during the recovery stage. The CCD and sediment carbonate content overshoot during the recovery stage is muted by a predicted increase in $CaCO_3$ rain. Nonetheless, there are indications that the $CaCO_3$ export remained relatively constant during the PETM. If this was indeed true, then an initial pulse of 3,000 Pg C followed by an additional, slow leak of 2,500 Pg C could have triggered an accelerated nutrient supply to the surface ocean instigating enhanced organic carbon export, consequently increasing organic carbon

sequestration, resulting in an accelerated restoration of ocean-atmosphere biogeochemistry during the termination phase of the PETM.

3.1 Introduction

One of the most abrupt and prominent decreases in $\delta^{13}C$ throughout the Cenozoic has been documented ubiquitously in both terrestrial and marine geological records during the Paleocene-Eocene Thermal Maximum (PETM; ∼56 Ma). A negative carbon isotope excursion of 2.5‰ or more *Kennett and Stott* [1991]; *McInerney and Wing* [2011] coincided with a global temperature increase of 5 to 8^oC *Zachos et al.* [2003]; *Tripati et al.* [2009]; *McInerney and Wing* [2011], suggesting that the PETM was caused by an extraordinary input of isotopically light C into the ocean-atmosphere system. The massive (> 3,000 Pg C) input of ^{13}C-depleted carbon during the onset of the PETM was injected into the system over at least 4,000 years (e.g., *Zachos et al.* [2005]; *Zeebe et al.* [2016]). Although the exact source of the light carbon remains unknown, several potential mechanisms have been posited, including methane hydrate dissociation on the sea floor *Dickens et al.* [1995, 1997]; *Zachos et al.* [2005], terrestrial carbon sources *Kurtz et al.* [2003]; *Pancost et al.* [2007]; *DeConto et al.* [2012] and oxidation of sedimentary organic carbon *Svensen et al.* [2004]. The entire event, including the onset, main phase and recovery, spanned a period of about 150,000 - 200,000 years *Farley and Eltgroth* [2003]; *Murphy et al.* [2010]; *Röhl et al.* [2007], during which the excess carbon was ultimately removed from the ocean-atmosphere system through various biogeochemical feedbacks.

On long time scales, the primary restoring mechanism of excess carbon is via accelerated silicate weathering due to higher pCO_2, temperature and an intensified hydrological cycle. However, the recovery of $\delta^{13}C$ during the PETM was more rapid than anticipated for removal through enhanced silicate weathering alone *Dickens* [2001]; *Bowen and Zachos* [2010]; *Bowen* [2013]. The rapid nature of the PETM recovery is often attributed to enhanced burial of

organic matter *Bains et al.* [2000]; *Dickens* [2001]; *Bowen and Zachos* [2010]; *Bowen* [2013] or explained by increased net organic carbon storage (refueling of a putative organic carbon reservoir; e.g. methane hydrate capacitor) *Dickens* [2003]. The biological production and removal of carbon from the surface ocean and its export and sequestration at the ocean bottom (biological carbon pump) might play an important role in regulating climate on multi-millennial time scales *Broecker* [1982], and it might have governed the pace and the duration of the PETM recovery. On long time scales, dissolved phosphorus (P) in the ocean is the nutrient that limits biological production *Tyrrell* [1999]. The dissolved P concentration in the ocean depends on P inputs from the continents and burial in the sediments *Wallmann* [2010], as well as on the ambient redox conditions, which determine the rate of P burial/regeneration *Van Cappellen and Ingall* [1994]; *Slomp and Van Cappellen* [2007]; *Wallmann* [2003].

The riverine input of P is proportional to the silicate and carbonate weathering fluxes *Flögel et al.* [2011]. Hence, the elevated CO_2 and temperature during the PETM, and therefore globally enhanced continental weathering rates *Ravizza et al.* [2001]; *Penman* [2016], should in theory entail greater primary production in surface ocean through an increased nutrient supply from the continents. Data from various locations worldwide indicate that the nutrient supply was amplified during the PETM (e.g., *Gibbs et al.* [2006]; *Sluijs et al.* [2006]; *John et al.* [2008]; *Sluijs et al.* [2009]; *Schulte et al.* [2011]). Consequently, increased marine paleo-production *Dickson et al.* [2014] may have instigated a draw-down of bottom water oxygen. Indeed, there is evidence for reduced oxygen concentration during the PETM (e.g., *Chun et al.* [2010]; *Dickson et al.* [2012]; *Pälike et al.* [2014]; *Sluijs et al.* [2014]), which does not directly implicate enhanced production as the sole cause of the draw-down. Other mechanisms, such as oxidation of methane in the water column, might have been responsible.

Regardless of mechanism, anoxic bottom waters may enhance P remineralization, leading to a higher dissolved P content of the surface ocean and therefore further increase in marine production and oxygen depletion (a positive feedback loop), while at the same time withdrawing more CO_2 from the atmosphere *Van Cappellen and Ingall* [1994]. Furthermore, a lower O_2 concentration would lead to a greater organic carbon preservation and carbon burial. Therefore, increased CO_2 emissions during the PETM might have stimulated biological production, which would ultimately act as a mechanism for removing excess carbon from the ocean-atmosphere system. This hypothesis is consistent with the evidence of increased ocean primary production and carbon export during this time interval as inferred from marine barite accumulation rates *Bains et al.* [2000]; *Ma et al.* [2014] and cocolith Sr/Ca *Stoll and Bains* [2003].

Here, we utilize the LOSCAR (Long-term Ocean-atmosphere-Sediment CArbon cycle Reservoir) model to analyze the biogeochemical feedbacks between biological production, carbon (C), oxygen (O), phosphorus (P), and carbonate chemistry during massive CO_2 release events, such as the PETM. The original LOSCAR model was expanded to include a phosphorus cycle combining the works of *Slomp and Van Cappellen* [2007], *Tsandev and Slomp* [2009] and *Flögel et al.* [2011]. The key objective is to investigate the role of combined C-O-P feedback during the PETM and thus, provide a potential mechanism for the rapid removal of excess C from the ocean-atmosphere system consistent with the available PETM data and current understanding of the biogeochemical cycles involved. The PETM is dubbed the closest analogue for the ongoing anthropogenic climate change *Pagani et al.* [2006]; *Zachos et al.* [2008]; *Zeebe and Zachos* [2013]. Therefore, quantifying the changes in phosphorus, biological production, oxygen concentration, and carbon removal as well as

identifying the mechanisms initiating rapid carbon sequestration during the PETM may offer insight into future changes of biogeochemical processes in the ocean.

3.2 Model Description

The model used in this study is an expanded version of the LOSCAR model *Zeebe* [2012a]. LOSCAR is comprehensively documented in *Zeebe* [2012a] and has been used and tested in numerous earlier studies (e.g, *Zeebe et al.* [2008, 2009]; *Komar et al.* [2013]; *Komar and Zeebe* [2016]). Thus, aside from briefly covering the major features of LOSCAR (below), we abstain from explaining the model in greater detail here. However, the expansion of the model, pertaining to the P cycle will be thoroughly discussed.

LOSCAR is a 13-box (paleo-version) ocean model with an additional box representing the atmosphere, coupled to a sediment model. It efficiently computes the partitioning of carbon between ocean, atmosphere and sediments on a wide range of time scales, from centuries to millions of years. The volumes of ocean boxes are based on realistic Paleocene/Eocene ocean basin topography *Bice et al.* [1998]. The model includes a variety of biogeochemical tracers such as total carbon (TC), total alkalinity (TA), phosphate, oxygen, calcium and stable carbon and calcium isotopes. Using the model predicted evolution of TC and TA values, numerous seawater carbonate parameters ([CO2], [CO32-], pH, calcite and aragonite saturation state) are computed using algorithms explained in *Zeebe and Wolf-Gladrow* [2001]. Weathering of carbonate and silicate rocks is parameterized as a function of atmospheric CO_2 *Uchikawa and Zeebe* [2008]; *Zeebe* [2012a].

The main components of the reactive phosphorus cycle include river input (F_{PW}), primary production, remineralization and sediment burial. The latter involves burial of particulate

organic P (POP; associated with living and detritus marine biomass), which is comprised of organic material that rains down from the surface ocean, escapes remineralization, and reaches the sediments where it is buried (F_{OPB}). Phosphorus is also buried in the sediments associated with authigenic ferric iron oxides (F_{FeP}) or precipitated as authigenic carbonate fluorapatite (F_{CaP}) *Slomp and Van Cappellen* [2007] (see Table 5.1). There is no explicit diagenetic sediment model associated with the P burial and the LOSCAR P cycle version (LOSCAR-P for short) does not account for biogenic P burial fluxes from fish debris. Therefore, in addition to the original internal LOSCAR phosphate fluxes *Zeebe* [2012a], the change of the phosphate concentration ($[PO_4]$) is governed by four additional external terms as described above:

$$\left.\frac{d[PO_4]}{dt}\right|_{ex} = F_{PW} - (F_{OPB} + F_{CaP} + F_{FeP}). \tag{3.1}$$

In LOSCAR, primary production rates are parameterized based on the phosphate concentration in the ocean surface layer. The biological uptake fluxes of PO_4 are related to the primary production via the Redfield-ratio (C/P = 130). The total initial export production from the surface ocean, controlled by $[PO_4]$ and the biopump efficiency (f_{epl} =80%), *Zeebe* [2012a] is around 460 Tmol C/yr, which is almost identical to the value estimated for the pre-PETM period (*Ma et al.* [2014]; value estimated from barite accumulation rates using a modern relationship). In the default LOSCAR-P set-up (control run), a large fraction (99%) of the carbon export flux (F_{Cexp}) is remineralized in the intermediate and deep ocean boxes, while the remainder (fraction of organic carbon buried (f_{OC}); initially set to 1%) is lost to the sediments. On the other hand, the C/P ratio in buried organic matter depends on the

redox state of bottom waters *Van Cappellen and Ingall* [1994]; *Tsandev and Slomp* [2009] and is initially about twice as large (∼250) as the ratio in the surface water (see below). In order to achieve this C/P in buried organic matter in LOSCAR-P, the fraction of the export flux of P (f_{OP}) from the surface ocean buried in sediments was set to half (0.5%) the fraction of organic C export (f_{OC} = 1%) buried in sediments. Therefore, the organic C burial flux is initially 260 times larger than the organic P burial flux (Table 5.1); 130 times larger at the surface due to Redfield and additional two times larger due to the burial ratios (see f_{OC} and f_{OP} fractions).

Nitrate (N) in LOSCAR is parameterized based on the C to N Redfield-ratio (C/N = 130/15). Uptake and release of nitrate contributes to alkalinity changes in the model. In LOSCAR-P, the changes in alkalinity due to changes in the above mentioned P fluxes (and hence N) also need to be accounted for. The original LOSCAR version (without the P burial cycle) assumes that the export from the surface ocean of the elements P and N is completely remineralized in the intermediate and deep boxes. In LOSCAR-P, a portion of the export flux is buried in the sediments and therefore not remineralized (in order to balance the riverine input flux). Due to the Redfield ratio link between N and P, also nitrate taken up from the surface that reaches the deep ocean is not fully respired, which creates an alkalinity imbalance. The nitrate and phosphate portion of the export flux that is not respired (remineralized) represents an alkalinity source *Wolf-Gladrow et al.* [2007]. This additional source of alkalinity is balanced by the riverine input of nitrate and phosphate which acts as an alkalinity sink.

Unlike the P model of *Tsandev and Slomp* [2009], *Slomp and Van Cappellen* [2007], and *Flögel et al.* [2011], LOSCAR-P does not include a separate representation of the shelf and

deep oceans. In other words, the entire P that is buried is removed from the deep boxes. The burial of P (and C), which is redox dependent, is therefore based on the mean deep ocean oxygen concentration *Lenton and Watson* [2000].

3.2.1 Redox-controlled reactive P and organic C burial

The organic phosphate burial flux (F_{OPB}) is assumed to be proportional to the export flux (F_{Pexp}) from the surface ocean *Tsandev and Slomp* [2009]:

$$F_{OPB} = f_{OP} \times F_{Pexp} \times \left(0.25 + 0.75\frac{[O_2]}{[O_2]_0}\right), \tag{3.2}$$

where f_{OP} is the fraction of the export flux that is buried in the sediments, initially set to 0.5%. This flux is also dependent on water column oxygenation *Slomp and Van Cappellen* [2007]; *Tsandev and Slomp* [2009]. $[O_2]_0$ is the bottom water oxygen concentration at time t = 0, which corresponds to modern deep ocean oxygen concentration *Slomp and Van Cappellen* [2007]. However, in our model $[O_2]_0$ represents the pre-PETM steady-state concentration. Burial of organic P is reduced by up to 75% under full anoxia, while the burial of organic carbon increases [Eq. (3.3); *Slomp and Van Cappellen*, 2007; *Tsandev and Slomp*, 2009].

The F_{OPB} and F_{OCB} fluxes are coupled through the organic matter C to P burial ratio, which is significantly larger than the Redfield value [*Slomp and Van Cappellen*, 2007; *Tsandev and Slomp*, 2009, and references therein]. This ratio also depends on the redox-state of the bottom waters *Tsandev and Slomp* [2009]:

$$\frac{F_{OCB}}{F_{OPB}} = \frac{\left(\frac{C}{P}\right)_{oxic} \times \left(\frac{C}{P}\right)_{anox}}{\frac{[O_2]}{[O_2]_0} \times \left(\frac{C}{P}\right)_{anox} + \left(1 - \frac{[O_2]}{[O_2]_0}\right) \times \left(\frac{C}{P}\right)_{oxic}}, \tag{3.3}$$

where $\left(\frac{C}{P}\right)_{oxic} = 260$ and $\left(\frac{C}{P}\right)_{anoxic} = 4000$ *Ingall et al.* [1993], represent end-member values for organic matter buried under completely oxic and fully anoxic deep water conditions, respectively.

The P flux associated with ferric iron oxides is linearly correlated to changes in oxygen concentration of the deep water *Tsandev and Slomp* [2009]:

$$F_{FeP} = F^0_{FeP} \times \frac{[\mathrm{O_2}]}{[\mathrm{O_2}]_0}, \tag{3.4}$$

where F^0_{FeP} is F_{FeP} at time t = 0 (pre-PETM steady-state rate).

Precipitation of authigenic CaP is formulated as follows *Tsandev and Slomp* [2009]:

$$F_{CaP} = f_{CaP} \times POP_{remin} \times \left(0.1 + 0.9\frac{[\mathrm{O_2}]}{[\mathrm{O_2}]_0}\right) \tag{3.5}$$

where f_{CaP} is a fraction of reactive P that is produced by decomposition of organic matter and is converted into CaP. Its value is 0.005 and is set to satisfy the steady-state condition. POP_{remin} is remineralization flux of P, which is equal to the difference between export and burial. Thus:

$$POP_{remin} = F_{Pexp} \times (1 - f_{OP}). \tag{3.6}$$

The phosphorus weathering flux is assumed to be regulated by the rates of chemical weathering and should therefore scale with the change in cumulative carbonate and silicate

weathering rates *Flögel et al.* [2011]:

$$F_{pw} = F^0_{pw} \times \frac{F_{wc} + F_{Si}}{F_{wc_0} + F_{Si_0}}, \tag{3.7}$$

where F^0_{pw}, F_{wc_0}, and F_{Si_0} are riverine input of dissolved phosphorus, carbonate, and silicate weathering at time t = 0 (pre-PETM steady-state rate), respectively.

3.3 PETM Simulations

The carbon perturbation used in this study involves a C input of 3,000 PgC (δ^{13}C= -50‰) in the form of methane to the deep Atlantic and/or atmosphere over 5,000 years. For simplicity and easier quantification of biogechemical effects and mechanisms, an additional continuous release of carbon (referred to as "leak"), described as the preferred PETM scenario *Zeebe et al.* [2009], in the amount of 1480 PgC over ∼40 kyr was initially omitted (Figures 3.1-3.4). For the same reason, the prescribed circulation change in the original LOSCAR simulation *Zeebe et al.* [2009] was also turned off. However, the leak feature in combination with new P burial model will be included later (Figure 3.5) to model the PETM more realistically and in order to constrain the amount of carbon drawdown during the PETM recovery phase.

We first perturb the ocean-atmosphere system and compare the responses of different LOSCAR versions in order to demonstrate the effect of the newly introduced P burial cycle. The three different versions of LOSCAR are color-coded so that colors are consistent between panels (Figure 3.1). Time $t = 0$ corresponds to the onset of the PETM (Paleocene-Eocene boundary), when the simulation is initiated by perturbing the system with the input of light carbon. Because the original LOSCAR version (red lines, Figure 3.1) does not include a P

burial cycle and there is no redox feedback between P and C, both P and organic C burial fluxes remain constant over time (Figure 3.1c and 3.1d). On the other hand, LOSCAR-P accounts for the redox dependency and thus displays a variable trend in P and C burial. It is apparent that the LOSCAR-P version exhibits a more rapid pCO_2 drop as well as a faster $\delta^{13}C$ recovery. This is due to an increase in organic carbon burial as a consequence of both increased $[PO_4]$ (and consequently larger carbon export flux; Figure 3.2) and a decrease in oxygen concentration (Figure 3.3a). The amount of excess carbon buried in the control LOSCAR-P simulation due to the C-O-P feedback (black line, Figure 3.1) over the entire 200 ky period is ∼1800 PgC. The details of the feedbacks is discussed in section 4.4.

The response of the phosphate concentration to the carbon perturbation in different ocean boxes (Figure 3.2a) in the LOSCAR-P control run is a combination of increased weathering fluxes as well as changes in P burial fluxes due to variable deep ocean oxygen concentration (Figure 3.3a). All ocean boxes display an increase in $[PO_4]$, which in turn affects the amount of carbon export from the surface ocean (Figure 3.2b). The initial burial fluxes, F_{Cap}, F_{OPB}, F_{FeP} are set in proportion of 50%, 25%, 25% of total reactive P burial based on preindustrial conditions *Ruttenberg* [1993] (Figure 3.3b). Initially, the F_{OPB} is set as a fraction (which we vary in sensitivity experiments, see below) of the export from the surface (Eq. (3.2)). Using the proportion stated, the other two P burial fluxes (F_{Cap} and F_{FeP}) are calculated. Therefore in order to achieve a steady-state, the riverine input of P is set to match to total P burial flux. The total inventory of dissolved PO_4 in the ocean in the control run is $\sim 3\times10^{15}$ mol P and the total burial flux is $\sim 7\times10^{10}$ mol yr^{-1}, hence the residence time of P in the ocean is ∼43,000 years.

The main controls on oceanic oxygen concentration in the model are seawater tempera-

ture, productivity and nutrient cycling, as well as oxidation of reduced carbon (Figure 3.3a). The combined effect of these processes results in a general oxygen decrease over time in all ocean boxes (Figure 3.3a). The sudden and more pronounced drop in $[O_2]$ in the deep Atlantic ocean is due to the oxidation of methane injected into this model box. The control run assumes that 40% of carbon is oxidized in the deep Atlantic, Deep Atlantic Oxidation (DAO) in the following *Zeebe et al.* [2009]. Sensitivity experiments revealed that the DAO fraction has a negligible effect on overall excess carbon burial and carbon isotope recovery during the PETM (see Supplement). We also explored the model sensitivity to a wide range of global P weathering and burial fluxes as well as kerogen oxidation and carbon burial. Since we assumed that the light carbon was injected in methane form (potentially from an organic carbon capacitor such as methane hydrates), an additional scenario is considered. This scenario takes into account the change in net organic C flux of the aforementioned capacitor (capacitor recharge) that would arise during the recovery phase of the PETM. Due to length constraints, the model runs outlined above are presented in the Supplement but a brief synopsis of the results is presented in Section 3.4.1.

Next, we include the additional carbon leak of 1,480 PgC over 42,000 years *Zeebe et al.* [2009], mentioned above, to investigate the main and recovery phase of the PETM and compare the results of the original LOSCAR and LOSCAR-P models (Figure 3.5). For LOSCAR-P, we also added a scenario with a stronger leak (2,500 PgC between 20 and 62 ky after the onset; our preferred scenario, see below) in order to get a prolonged carbon isotope excursion (Figure 3.5, green line) during the PETM main phase, which is more consistent with the $\delta^{13}C$ data (Figure 3.13). The initial P and C burial fluxes in the strong-leak scenario (leak = 2,500 Pg C) are identical to those used in the standard leak scenario (leak = 1,480

Pg C; $f_{OP} = 1.00\%$ and $f_{OC} = 2.00\%$; Figure 3.5, red line). In the original LOSCAR model, the organic carbon burial remains constant, for the reasons explained earlier. The calculated excess C burial, using the same set of conditions as in the control LOSCAR-P run but with the leak included, is ∼2,500 PgC (Figure 3.5, dashed black line). Doubling the initial carbon and phosphorus burial rates results in an overall excess C burial of about 4,300 PgC. The excess C burial during the entire PETM period in the "stronger-leak" scenario is ∼5,400 PgC.

Out of the four scenarios outlined above, the "stronger-leak" scenario, combined with enhanced initial carbon and phosphorus burial rates produces the swiftest $\delta^{13}C$ recovery (Figure 3.5c). Depending on the age model used, the recovery phase of the PETM appears to have lasted between 30,000-40,000 years [^{3}He age model; *Farley and Eltgroth*, 2003; *Bowen and Zachos*, 2010] or in the excess of 100 ky [cyclostratigraphic age model; *Röhl et al.*, 2007] (see Supplement). In our model, the recovery starts at around 60 ky after the onset, when the system is no longer perturbed by the input of light carbon. The integrated excess C burial between 60 ky and 100 ky (recovery phase duration according to the ^{3}He model) in our model in the strong leak scenario is 1,700 Pg C, which is close to the proposed amount of 2000 PgC needed to explain the observed $\delta^{13}C$ recovery rate *Bowen and Zachos* [2010].

Additionally, we compare the responses of the calcite compensation depth (CCD) as well as $CaCO_3$ wt% at two different depths for different "leak" scenarios described above (Figure 3.6). The simulation of the CCD evolution can be used as an additional model benchmark by reproducing the CCD trends that are consistent with observations. Particularly, examining whether a certain scenario produces an over-deepening (overshoot) of the CCD during the PETM recovery phase, which is evident in many sediment sections *Zachos et al.* [2005]; *Leon-*

Rodriguez and Dickens [2010]; *Kelly et al.* [2005]; *Slotnick et al.* [2015]; *Penman et al.* [2016]. The most notable difference in the CCD response between the original LOSCAR (Figure 3.6, solid blue line) and LOSCAR-P during the recovery stage is that the CCD overshoot in the LOSCAR-P model is muted or not present at all (Figure 3.6, dashed black line). The mechanism responsible for the reduced CCD deepening during the recovery stage and implications of the result are discussed in more detail in Section 3.4.3.

3.4 Discussion

3.4.1 The feedback between Carbon, Oxygen and Phosphorus

Our results imply that the feedback between carbon, oxygen, and phosphorus cycling in the ocean-atmosphere system may ultimately lead to enhanced organic carbon sequestration during large carbon emission events. The feedback mechanism is set in motion once the system is perturbed with a large enough quantity of carbon, which triggers a series of events, starting with an increase in atmospheric CO_2 (Figure 3.1a) and global warming. Warmer temperatures lead to an intensified hydrological cycle and accelerated weathering of phosphate minerals, eventually resulting in higher phosphate concentration in the sea (Figure 3.2a). Being the limiting nutrient, higher phosphorus content in the surface ocean instigates a stronger biological production and larger carbon export to the deep ocean (Figure 3.2b), which is consistent with paleo-export production data derived from marine barite accumulation rates for the PETM *Bains et al.* [2000]; *Ma et al.* [2014] and cocolith Sr/Ca *Stoll and Bains* [2003].

Concurrent with the phosphate content increase is a decline in oxygen concentration (Figure 3.3a). There are two different processes in the model that both contribute to the

oxygen draw-down. First, the rising global temperature reduces the amount of dissolved oxygen in the water column by lowering the solubility of oxygen *Weiss* [1970], thus we observe a long-term oxygen drop in all ocean basins (Figure 3.3a). Second, due to a carbon input in the deep Atlantic, simulated oxygen concentration in this basin plunges temporarily as a result of carbon input and its subsequent oxidation. This model behavior is in line with many previous studies that indicate a reduction in oxygenation of seawater during the PETM (e.g., *Chun et al.* [2010]; *Dickson et al.* [2012]; *Pälike et al.* [2014]; *Sluijs et al.* [2014]).

The dependence of C and P burial on the redox state of the ocean is described mathematically in Section 3.2.1 (Eqs.(3.2-3.6)). Lowered oxygen concentration diminishes the organic carbon remineralization rate and therefore results in a higher organic carbon preservation and burial (e.g., *Hartnett et al.* [1998]). At the same time, lowered oxygen content allows for enhanced P regeneration (e.g. *Ingall et al.* [1993]) and the eventual refueling of the surface ocean with more nutrients, which then amplifies the primary production and carbon export and preservation, thus accelerating CO_2 and $\delta^{13}C$ recovery even further in a positive feedback loop. It is worth mentioning that the warming ($\sim 3.5^oC$ at most) predicted by LOSCAR (using the canonical climate sensitivity of 3 K per CO_2 doubling) through the radiative forcing of the CO_2 underestimates the warming reconstructed from proxies ($>5^oC$) *Zeebe et al.* [2009]. Therefore the long-term O_2 decline caused be the solubility decrease would have been even more pronounced in reality, which would have resulted in a higher excess organic C burial through the redox dependence.

The variations in phosphorus burial fluxes are primarily driven by the redox feedbacks and/or the export production from the surface ocean. Burial of phosphorus bound to iron oxides (Figure 3.3b, dotted-dashed red line) has a direct linear relationship to the mean

oxygen concentration of the deep ocean (Eq. (3.4)) and thus follows a similar trend to that of oxygen. Therefore, less P is buried (more regenerated) through F_{FeP} as oxygen concentration decreases and in theory, no P could be buried at all in completely anoxic waters *Tsandev and Slomp* [2009]. The burial flux of the organic phosphorus (Figure 3.3b, solid green line), unlike F_{FeP}, not only depends on the oxygenation but also on the export production from the surface ocean. As the O_2 concentration plummets over the first several thousands years, due to methane oxidation, so does the organic phosphorus burial. However, as the export production increases due to rising surface ocean [PO_4] (Figure 3.2), the organic P burial starts to recover, eventually reaching rates slightly higher than the initial, even though the oxygen concentration remains below the initial levels. The removal of P via authigenic F_{CaP} exhibits a different behavior from the other two previously described P burial fluxes by staying elevated for the entire duration of the run (Figure 3.3b, dashed blue line). Although F_{CaP} is also redox dependent (Eq. (3.5)) and thus expected to decrease during the water deoxygenation, the burial rate remains above the initial value even during the strongest oxygen depletion that takes place throughout the first several thousand years of the simulation. This is due to the fact that F_{CaP} also depends on P regeneration, which is the difference between the export and burial rate of phosphorus (Eqs. (3.5) and (3.6)). As the burial rate of P is attenuated in the first several thousand of years while the export simultaneously increases, the regeneration rate is intensified and overpowers the reduction in F_{CaP} that results from a decrease in oxygen concentration. The total P burial is simply the sum of all three P burial fluxes accounted for in the model (Figure 3.3b, dotted black line).

Organic carbon burial and P burial in the deep ocean are linked through the C to P burial ratio of the buried organic matter (Eq. (3.3)). Eq. (3.3) accounts for the effect of oxygen

on the C to P ratio based on observations, which suggests ratios considerably higher than Redfield, especially under anoxic conditions (e.g., *Ingall et al.* [1993]; *Filippelli* [2001]). Thus, according to the equation, organic C burial is directly proportional to organic P burial and inversely related to oxygen concentration. Therefore, as the deep ocean oxygen concentration drops, the rate of carbon burial increases, as shown across all of our LOSCAR-P simulations (e.g. Figure 3.1c). The amount of cumulative excess carbon burial during the entire duration of the PETM is sensitive to the initial C burial/kerogen oxidation flux and P burial/riverine flux (Figures 3.4 and 3.11) but the relationship is not linear. For example, quadrupling both the initial P and C fluxes increases the overall excess C burial by a factor of 3.3. The modeled overall excess C burial is less sensitive to the initial P burial than C burial (Figure 3.4), however it is important since it directly affects the residence time of P in the ocean. With higher throughput of P, and therefore shorter residence time of phosphorus in the ocean, the peak P burial fluxes, and consequently C burial fluxes, are achieved much earlier when compared to simulations with initially lower P burial (Figure 3.11c and 3.11d). The rates also recover faster in simulations with high initial P burial (compare red lines in Figure 3.11c), so the excess accumulation period of C is shortened, producing less C burial over the last 75 ky compared to the low initial P simulations. This is the reason for the non-linearity and for a decrease in C sequestration sensitivity at higher initial P burial rates (Figure 3.4).

3.4.2 Organic carbon burial and δ^{13}C in the sediment record

Data from certain paleo-locations support the idea that the PETM might have gone through a phase of elevated organic carbon burial, compared to the pre-PETM conditions *John et al.* [2008]; *Sluijs et al.* [2006], which is a behavior predicted by our model. Using the present day

continental shelf area, *John et al.* [2008] extrapolated the excess cumulative mass accumulation rates data of organic carbon from the North American continental margin to provide a very crude estimate of the global excess cumulative carbon burial during the PETM. Their estimates shows that about 2200 to 2900 Pg C could have been sequestered, this number is even larger if the actual Eocene continental shelf area is used, considering a higher sea level. They show that organic carbon mass accumulation rates remained elevated throughout the entire duration of the PETM. Furthermore, the peak excess accumulation lags the peak in carbon isotope excursion and it stays intensified even during the PETM recovery phase, similar to the shape of organic C burial predicted by LOSCAR-P (Figure 3.7).

It has been suggested that a transient increase in organic burial during the recovery stage of the PETM is necessary in order to produce the rapid CIE recovery observed in the record *Bowen and Zachos* [2010]. *Bowen and Zachos* [2010] explain the rapid recovery by assuming an ad-hoc increase in organic carbon burial without providing a process-based mechanism for accelerated carbon storage. Our model indicates that significant sequestration of organic carbon can arise due to the C-O-P feedback, without employing any ad-hoc, temporary increases in carbon removal (Figure 3.5d, green line; 1,700 Pg C stored during the recovery stage). During the PETM main phase (between ∼20 ky and 60 ky) δ^{13}C is in quasi-steady-state, since the external input of light carbon is temporarily in balance with its removal via carbon burial and thus the δ^{13}C remains close to constant (Figure 3.5c, green line). The leak of light carbon ceases after ∼60 ky, while the organic C burial rate is at its highest at this point due to C-O-P feedbacks explained above. Hence, δ^{13}C starts to recover rapidly, owing to a massive draw-down of light carbon that comes from accelerated organic carbon burial, until a new steady-state is achieved. The general trend and behavior of the

modeled δ^{13}C is consistent with observations but the amount of carbon sequestered during the PETM recovery-phase (1,700 Pg C) is slightly smaller than that calculated by *Bowen and Zachos* [2010] (2,000 Pg C, which might be an upper limit). However, the value they calculated depends heavily on the age model and the location of δ^{13}C data used. This is problematic because of large inconsistencies associated with the actual data and age models (see Supplement).

3.4.3 The CCD and $CaCO_3$ content

Simulation of adequate CCD changes during the PETM may serve as an additional model constraint *Zeebe et al.* [2009]; *Penman et al.* [2016]. In carbon cycle models accounting for the feedback between atmospheric CO_2 and carbonate and silicate weathering, the CCD exhibits a behavior in which its position deepens during the recovery stages of the PETM compared to prior to the event (e.g., *Zeebe et al.* [2009]; *Zeebe and Zachos* [2013]). The CCD over-deepening is caused by the pCO_2-weathering feedback. The carbon input during the PETM main phase raises the atmospheric pCO_2 which remains elevated even after the carbon input has stopped (Figure 3.5a-3.5b), temporarily diminishing the carbonate saturation state of the ocean and reducing the burial of $CaCO_3$. Simultaneously, the elevated atmospheric CO_2 (and accompanying changes in temperature, hydrological cycle, plant productivity, pH of the soil etc.) accelerates the weathering of carbonate and silicate rocks, resulting in enhanced input of calcium and carbonate ions to the ocean. The imbalance between the inputs and outputs during the recovery stage of the PETM creates a surplus of Ca^{2+} and CO_3^{2-}, raising the saturation state of the ocean. The saturation state of the ocean continues to rise until a temporary steady-state between the influx and burial is established. This quasi-steady

state of carbonate saturation is higher than initially, because it is maintained at higher pCO_2 levels, and therefore the CCD is deepened in order to accommodate a larger carbonate burial rate needed to balance an enhanced input from weathering (see section 3.4.4).

Indirect lines of evidence support the model prediction and suggest that the carbonate preservation during the PETM recovery was noticeably higher than prior to the event (e.g., *Kelly et al.* [2010]), implying a suppressed CCD. Until recently, however, there was no direct evidence of a transient CCD over-deepening during the recovery stage of the PETM because all sediment sections recovered from this time period were positioned above the CCD. The carbonate content data recently presented in *Penman et al.* [2016] provide the first validation for the CCD overshoot, which appears in the record 70 ky after the onset of the PETM (based on a cyclo-stratigraphic age model) at IODP sites U1403 and U1409 in the North Atlantic. This CCD overshoot feature along with a slight increase in carbonate content in the recovery stage of the PETM are present in LOSCAR-P simulations that have high initial C and P burial fluxes (Figure 3.6, solid red and green lines). Nevertheless, for the same carbon input scenario and the same weathering feedback the over-deepening of the CCD in LOSCAR-P is muted compared to that of the original LOSCAR (Figure 3.6). The CCD muting in LOSCAR-P arises as a result of the increased phosphate concentration in the surface ocean. Higher PO_4 concentration yields higher organic carbon export and since the ratio between organic C rain and $CaCO_3$ is fixed in LOSCAR, the $CaCO_3$ rain to the sediments also increases. Because the flux of $CaCO_3$ per unit area is now larger, the CCD does not have to deepen as much (or at all) in order to balance the riverine input, hence the deepening is not as prominent or completely absent. It is important to mention that the magnitude of the CCD overshoot in the model also depends on the strength of the weathering feedback,

which itself is uncertain. The same simulation with a different weathering feedback strength (which is within the uncertainty envelope) could produce a scenario in which there is no CCD overshoot or a scenario with a more pronounced deepening (Figure 3.8). However, even when a strong weathering feedback is employed, the CCD over-deepening is not as prominent as indicated by the North Atlantic data.

LOSCAR-P produces a $CaCO_3$ content overshoot in the Atlantic ocean at both corresponding depths (which approximate sites U1403 and U1409, see below) but the overshoot at the deeper sediment box (4,500 m, which approximates site 1403) greatly underestimates the data (Figure 3.6b). The carbonate content at the deeper site (Site 1403: 4374m) is elevated by more than 20% around 70 ky after the onset of the PETM. This indicates that the CCD during the termination stage of the PETM likely reached below 4400 meters (at least in the North Atlantic). In contrast, LOSCAR-P produces only a 1% increase in carbonate content during the recovery in the Atlantic sediments box located at 4,500 m. Such a small increase is a result of the muted CCD signal as explained above (the CCD in LOSCAR-P is never deeper than 3,800 m). However, the deep Atlantic in LOSCAR is presented as a single box (i.e. extremely coarse spatial resolution). Therefore, the interpretation of LOSCAR results and their comparison to the data from a specific region should be taken with caution. Thus, we show the response of two additional sediment boxes in the model, between the depths of 3,000 m and 4,500 m, which exhibit an increase in carbonate content during the recovery stage of the PETM of 6% and 2%, at 3,500 m and 4,000 m sediment boxes, respectively, also indicating a slight overshoot but still underestimating the actual data.

Until more sediment sections are recovered from different regions that were positioned below the CCD prior to the PETM, there is no way of knowing for certain if the overshoot

was a global event nor is it possible to know the extent and the magnitude of over-deepening *Penman et al.* [2016], which would help validate the model results. If the overshoot was indeed global and of similar magnitude as observed in the North Atlantic ocean (which is very likely), then it would be difficult to reconcile the rapid recovery by an enhanced marine sequestration of organic carbon without assuming a constant (or decreased) $CaCO_3$ and alkalinity export during the recovery-stage of the PETM. Note that when such an assumption is invoked, as was the case in the original LOSCAR *Penman et al.* [2016], the CCD and $CaCO_3$ overshoot is more consistent with the data than the one produced in LOSCAR-P. This is because in simulations performed by *Penman et al.* [2016] the PO_4 concentration remains constant throughout the entire model run and therefore the $CaCO_3$ rain also stays unchanged, resulting in a deeper CCD (the mechanism explained above) during the recovery phase. Additionally, their initial CCD depth is around 600-700 m deeper than in LOSCAR-P, which contributes to a more pronounced $CaCO_3$ overshoot at the 4,500 m sediment box.

To show the effect of $CaCO_3$ rain on the CCD and $CaCO_3$ content overshoot we ran our preferred carbon emission scenario with the $CaCO_3$ rain constant (Figure 3.9). We additionally slightly reduce the initial $CaCO_3$ rain in order to get an initially deeper CCD, to be more consistent with *Penman et al.* [2016] simulations. The constant $CaCO_3$ rain scenario yields a more pronounced CCD over-deepening and a stronger $CaCO_3$ content overshoot. The 4,500 m sediment box produces an overshoot of 15% during the recovery stage, which is more consistent with the data (Figure 3.9, dotted-black line).

The question is whether the constant $CaCO_3$ rain assumed in the original LOSCAR or the increasing $CaCO_3$ rain predicted by LOSCAR-P is more representative of reality. *Gibbs et al.* [2010] reconstructed calcareous nannoplankton production at ODP Sites 690, 1209 and Bass

River based on nannoplankton counts coupled with taxon-specific Sr/Ca data. According to *Gibbs et al.* [2010], there was no significant change in biogenic carbonate production during the PETM. If $CaCO_3$ rain indeed did not increase during the PETM, and this assumption is incorporated into the model, then LOSCAR-P produces trends consistent with the current available data. As the validity of this scenario depends on the assumption from only one study, the model results should be interpreted with caution. Also, constant $CaCO_3$ rain requires decoupling, to some degree, from organic carbon rain.

3.4.4 LOSCAR sediment module and respiratory-driven carbonate dissolution

It has been suggested that the organic carbon rain and its subsequent oxidation near the sediment surface might also promote calcium carbonate dissolution within the sediments (even if the bottom water is super-saturated) by reducing the saturation state of the porewater (e.g., *Archer et al.* [1989]; *Emerson and Archer* [1990]). This respiratory-driven calcite dissolution has been implemented in some sediment models (e.g. *Emerson and Archer* [1990]; *Archer* [1996]; *Ridgwell* [2007]). LOSCAR, however, does currently not account for the effect of organic carbon respiration on $CaCO_3$ dissolution. Here, we argue that the lack of the respiratory-driven dissolution in LOSCAR's sediment model does not significantly impact the model results.

The two different model types, the respiratory-driven model (e.g. GENIE; *Ridgwell* [2007]) versus non-respiratory model (e.g. LOSCAR), exhibit different wt% $CaCO_3$ and the CCD behavior during the PETM aftermath *Penman et al.* [2016]. During the PETM recovery, in LOSCAR, the elevated saturation state, and therefore the enhanced carbonate

burial (see section 3.4.3), is accommodated by an increase in the $CaCO_3$ content of the deep-sea sediments. The $CaCO_3$ content of the shallow sediments, located above the lysocline (e.g. 3000 m depth), however, are already at their maximum carbonate "holding capacity" and therefore the carbonate content of the shallow sediments cannot increase any further. On the other hand, respiratory-driven models such as GENIE, simulate dissolution of $CaCO_3$ even in the sediments above the lysocline. The $CaCO_3$ depletion of shallow sediments (as observed during the PETM onset and main phase) in such models , caused by organic carbon respiration, increases the potential of those sediments to hold more carbonate during the high saturation events (as observed during the PETM recovery). For those reasons, LOSCAR accommodates the increase in carbonate burial during the recovery-phase of the PETM mainly by increasing the depth of the CCD (compared to the pre-event depth). Whereas respiratory-driven sediment models can accommodate such change in the shallow sediments, thus not producing the CCD over-deepening or the $CaCO_3$ overshoot. According to data, both mechanisms or the combination of the two may be representative of the real world *Penman et al.* [2016].

The respiratory-driven sediment models suggest that the rate of $CaCO_3$ accumulation/dissolution in the deep sea depends heavily on the ratio between the organic carbon and calcium carbonate carbon reaching the sediments (rain ratio) *Emerson and Archer* [1990]; *Archer* [1991, 1996]. It is important to note that there is very little difference in predicted lysocline response between the rain ratio of 0 (essentially no organic carbon reaching the sediments) and rain ratio of 0.5 model scenarios (see Figure 5 in *Archer* [1991]). When this rain ratio is low (org./inorg.$<$ 0.5) the calcite dry content in the sediments is not greatly affected by organic carbon respiration above the saturation horizon *Archer* [1991]. Even in slightly un-

dersaturated waters (just below the saturation horizon) the rate of $CaCO_3$ accumulation is not significantly altered by organic carbon respiration when the organic to inorganic carbon rain ratio is low *Archer* [1991]. We examined the amounts of organic and inorganic carbon reaching the sediments in LOSCAR at the relevant depth (4,000 m; see below) in order to determine whether the absence of the respiratory-driven sediment model would significantly alter the results of this study.

Because the CCD in LOSCAR during the recovery phase of the PETM is around 4,000 m, which is in good agreement with the CCD reconstructed from data *Slotnick et al.* [2015], and because the paleodepth of the sediment core recovered from site U1403 was around 4,000 m, we define this as the depth of interest. The organic carbon flux from the surface ocean is attenuated with depth, thus knowing the export flux of organic carbon at the surface allows for approximation of the flux at any ocean depth using, e.g., the Martin curve *Martin et al.* [1987]:

$$F = F_{100} \times \left(\frac{z}{100}\right)^{-b} \tag{3.8}$$

where F is the organic carbon flux at the depth z (meters) and F_{100} is the particulate organic carbon export at 100 meters, and b is the attenuation factor with the standard value of 0.858 *Martin et al.* [1987].

According to the Martin curve, about 4% of the organic carbon production in the surface ocean reaches the depth of 4,000 m. In the default LOSCAR-P simulation this translates to $\sim$0.05 mol C m^{-2} yr^{-1} in the low latitude ocean. The revisited carbon flux study for the modern ocean suggests that the attenuation factor in warmer waters (among other factors),

at the Hawaii Ocean time series, can be as high as 1.33 *Buesseler et al.* [2007], meaning that only 0.7% ($\sim$0.008 mol C m^{-2} yr^{-1} in LOSCAR) of the surface ocean production could be reaching the depth of 4,000 m. Total inorganic carbon rain to sediments in LOSCAR is around 0.11 mol C m^{-2} yr^{-1} (40 $\times 10^{12}$ mol C yr^{-1}, comparable to the modern day value of 32 $\times 10^{12}$ mol C yr^{-1} *Milliman* [1993]), and specifically in the Atlantic ocean at 4,000 m depth is $\sim$0.10 mol C m^{-2} yr^{-1}. Thus, the standard Martin curve produces a rain ratio of 0.5 in LOSCAR's deep ocean. The Martin curve with strong attenuation, pertaining to a subtropical gyre yields even a smaller ratio ($\sim$0.1 for $b = 1.33$) of organic to inorganic C. The revised Martin curve study was based on the export flux measurements from two different environments. One located in colder waters of Northwest Pacific subartic gyre, and the the other located in warm waters north of a subtropical gyre north of Hawaii. The stronger attenuation factor ($b = 1.33$) belongs to the warmer site, while the colder locality showed a significantly weaker attenuation with depth ($b = 0.51$) *Buesseler et al.* [2007]. In the modern ocean, the majority of organic carbon export to the deep sediments takes place within 30 degrees of the equator *Jahnke* [1996], meaning that the globally averaged attenuation factor in the Martin curve should be skewed towards the higher value. It has been argued that the export flux differences between the two sites might have arisen due to different heterotrophic metabolic rates, influenced by contrasting water temperatures *Olivarez Lyle and Lyle* [2006]; *Buesseler et al.* [2007]; *Matsumoto* [2007]. If this is in fact the reason, then due to warmer global temperatures during the PETM the Martin curve for the modern ocean subtropical region ($b = 1.33$) is more representative of the mean global organic carbon export attenuation during the PETM. In that case, the $CaCO_3$ dissolution caused by organic carbon respiration would be even more diminished. As stated above, for Corg/$CaCO_3$ ratios < 0.5, respiratory-

driven dissolution is essentially negligible *Archer* [1991].

Even if respiratory-driven dissolution was important during the PETM, would the respiration rate significantly change for varying phosphate concentration and organic carbon export in our model scenarios? It turns out that even though the carbon export in LOSCAR increases with time (Figure 3.2b), respiration does not change significantly. It decreases by less than 1% at the peak carbon export. This is due to the fact that an increase in carbon export is accompanied by an increase in organic carbon burial, thus the difference between the two nearly constant. In summary, because of the relatively constant respiration rate and a low ratio of organic to inorganic carbon reaching the deep sediments our CCD over-deepening and $CaCO_3$ sediment weight content overshoot results can be used as a model constraint, even though the model is lacking respiratory-driven carbonate dissolution in the sediments.

3.5 Summary and Conclusions

The Paleocene-Eocene Thermal Maximum (∼56 Ma) was an event characterized by a major carbon cycle perturbation manifested in the geological record as a large negative $\delta^{13}C$ excursion (e.g., *McInerney and Wing* [2011]), global warming of more than 5^oC (as inferred from $\delta^{18}O$ isotopes) *Zachos et al.* [2003]; *Tripati et al.* [2009], and severe dissolution of carbonate sediments (e.g., *Zachos et al.* [2005]). These anomalies can collectively only be generated by a large and rapid introduction of carbon into the ocean-atmosphere system. As such, the PETM is considered the most important analog to the ongoing anthropogenic carbon emissions and thus has been intensively studied. The majority of the studies were focused on resolving the source and the magnitude of carbon input (onset phase) (e.g., *Dickens et al.* [1995]; *Zachos et al.* [2005]; *Zeebe et al.* [2009]), as well as the duration of the emissions (onset

+ main phase) (e.g., *Zeebe et al.* [2016]) or the event as a whole (e.g., *Farley and Eltgroth* [2003]; *Murphy et al.* [2010]; *Röhl et al.* [2007]), while relatively few studies were centered around the recovery-stage of the PETM *Bowen and Zachos* [2010].

Here, we primarily focus on the termination stage of the PETM and the mechanisms responsible for restoration of the earth-ocean system biogeochemistry after a major carbon perturbation. We show that a coupled carbon-phosphorus model with a redox-controlled reactive P and organic C burial produces enhanced carbon sequestration during the PETM. The total amount of carbon sequestered is independent of the locale (Atlantic ocean vs. atmosphere) of the simulated methane oxidation (see Supplement). In order to explain the accelerated δ^{13}C restoration during the recovery-phase of the PETM a larger initial throughput of P is required, resulting in the residence time of dissolved phosphate in the ocean of $\sim$21 ky, which is within the range estimated for the modern ocean [16 ky - 38 ky; *Ruttenberg*, 1993].

Our preferred scenario produces trends consistent with oxygen (e.g., *Chun et al.* [2010]; *Dickson et al.* [2012]; *Pälike et al.* [2014]; *Sluijs et al.* [2014]), excess accumulation rates of organic carbon *John et al.* [2008], export production *Bains et al.* [2000]; *Ma et al.* [2014], sediment carbonate content *Penman et al.* [2016] and δ^{13}C data. Unlike *Bowen and Zachos* [2010], we do not assume an ad-hoc, transient increase in organic carbon burial. The burial is rather predicted and driven by the redox-dependency between organic carbon and phosphorus. However, the standard LOSCAR-P model fails to quantitatively recreate the magnitude of the CCD and carbonate content overshoot observed in the North Atlantic as the model mutes the overshoot signal by predicting an increase in carbonate rain from the surface ocean. The accelerated earth-system biogeochemical recovery during the PETM could be ascribed

to the rise in nutrient supply and enhanced primary production and consequential increase in organic carbon sequestration only if the $CaCO_3$ rain remained constant (or decreased) during the termination stage of the PETM.

3.6 Figures

Figure 3.1: Comparison of responses of different LOSCAR model versions to a 3000 Pg C perturbation. a) Atmospheric CO_2 b) Mean surface $\delta^{13}C$ c) Organic carbon burial flux d) Total P burial flux (F_{Cap} + F_{OPB}+ F_{FeP}). Solid red line: the original LOSCAR model without P burial. Dashed blue line: LOSCAR-P burial but with constant P riverine input. Dotted black line: LOSCAR-P burial and CO_2 dependent P weathering (LOSCAR-P control run). The results displayed in red, blue and black lines correspond to LOSCAR without P burial cycle, LOSCAR that includes P burial cycle but P weathering is constant, and LOSCAR version with P cycle in which P weathering is pCO_2-dependent (LOSCAR-P), respectively. The black line represents the LOSCAR-P control run, with steady-state fluxes outlined in Table 5.1.

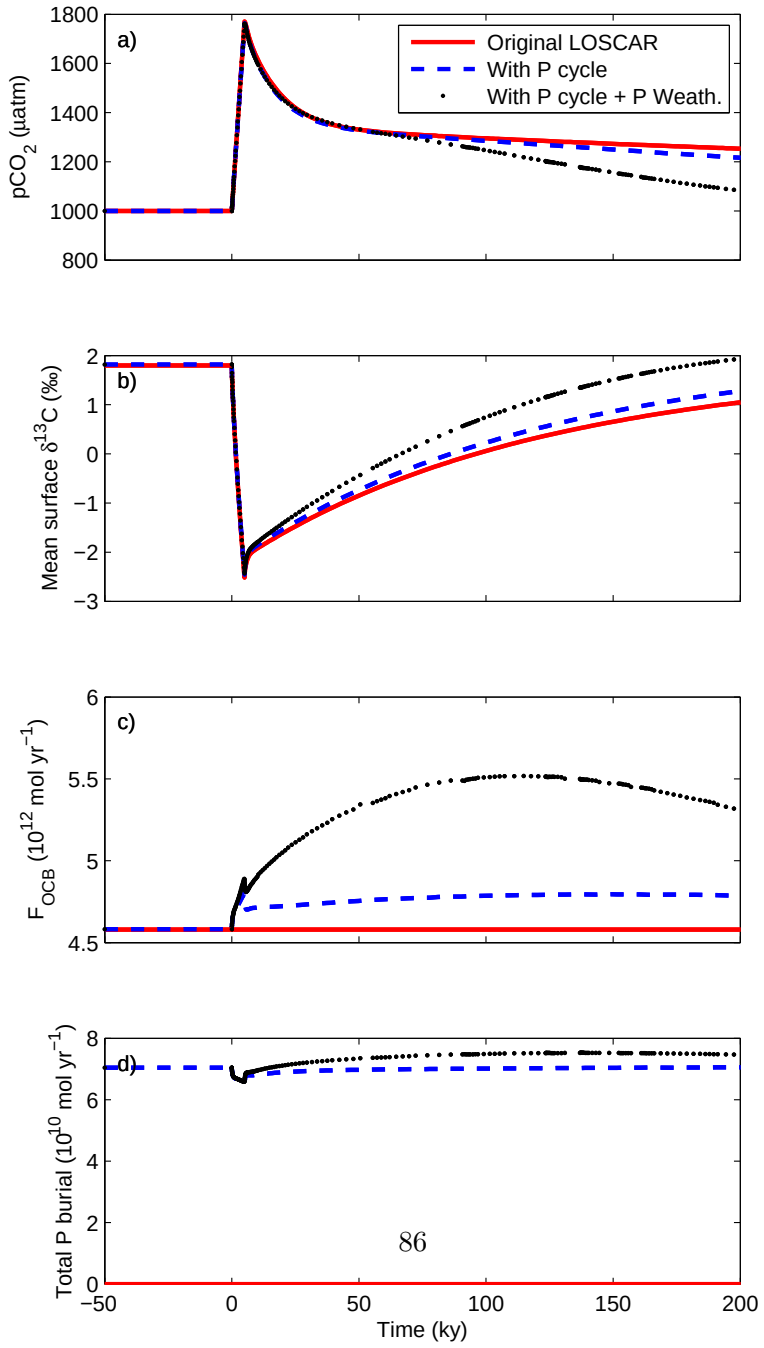

Figure 3.2: Oceanic phosphate concentration (a) and global export production (b) in response to a 3000 Pg C perturbation in the control LOSCAR-P run. L, I, and D correspond to surface, intermediate, and deep ocean boxes, respectively. A, I, P, and T represent Atlantic, Indian, Pacific, and Tethys ocean, respectively.

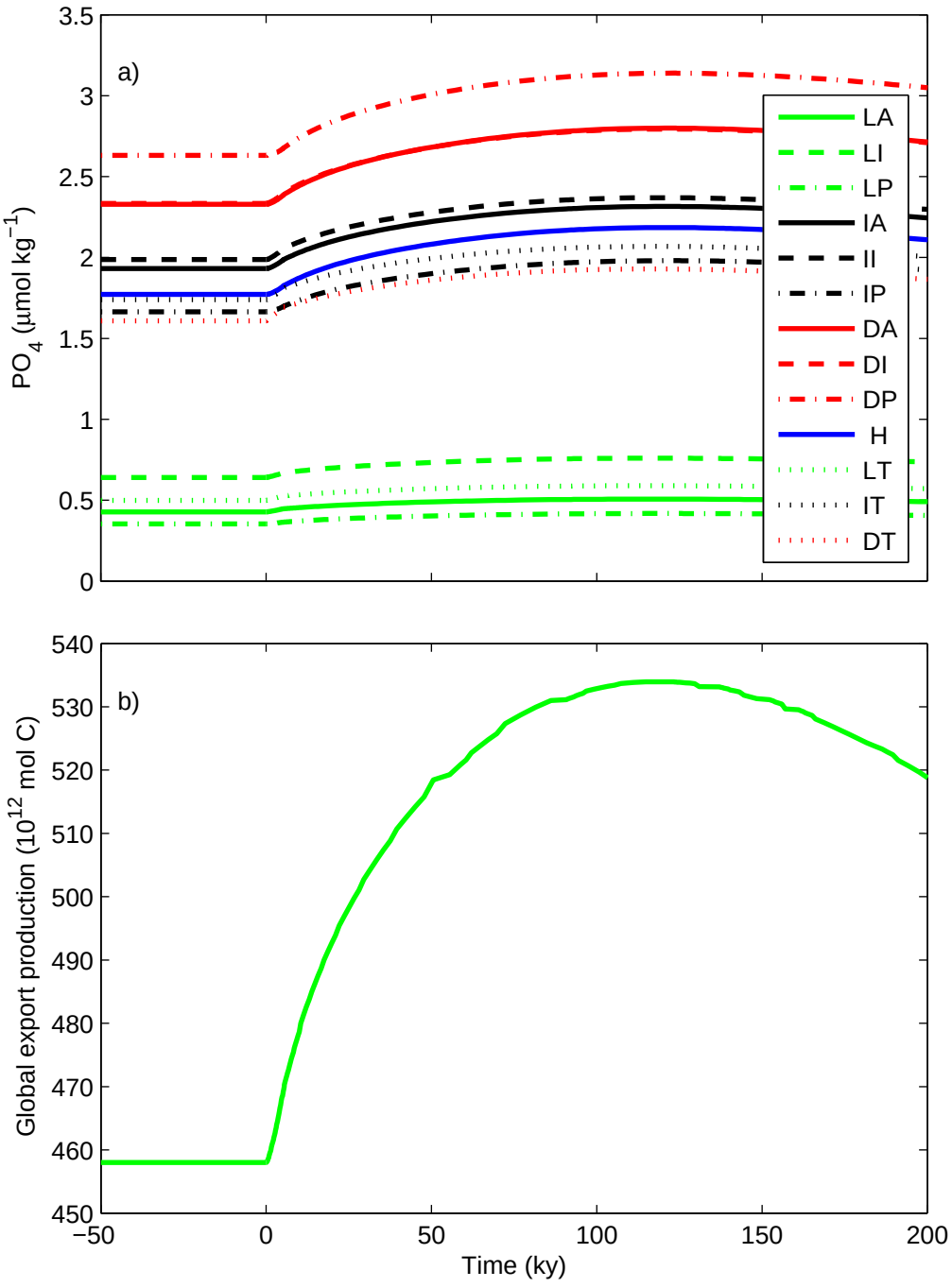

Figure 3.3: Evolution of the dissolved oxygen concentration (a) and phosphorus burial fluxes (b) to a 3000 Pg C perturbation in the control LOSCAR-P run.

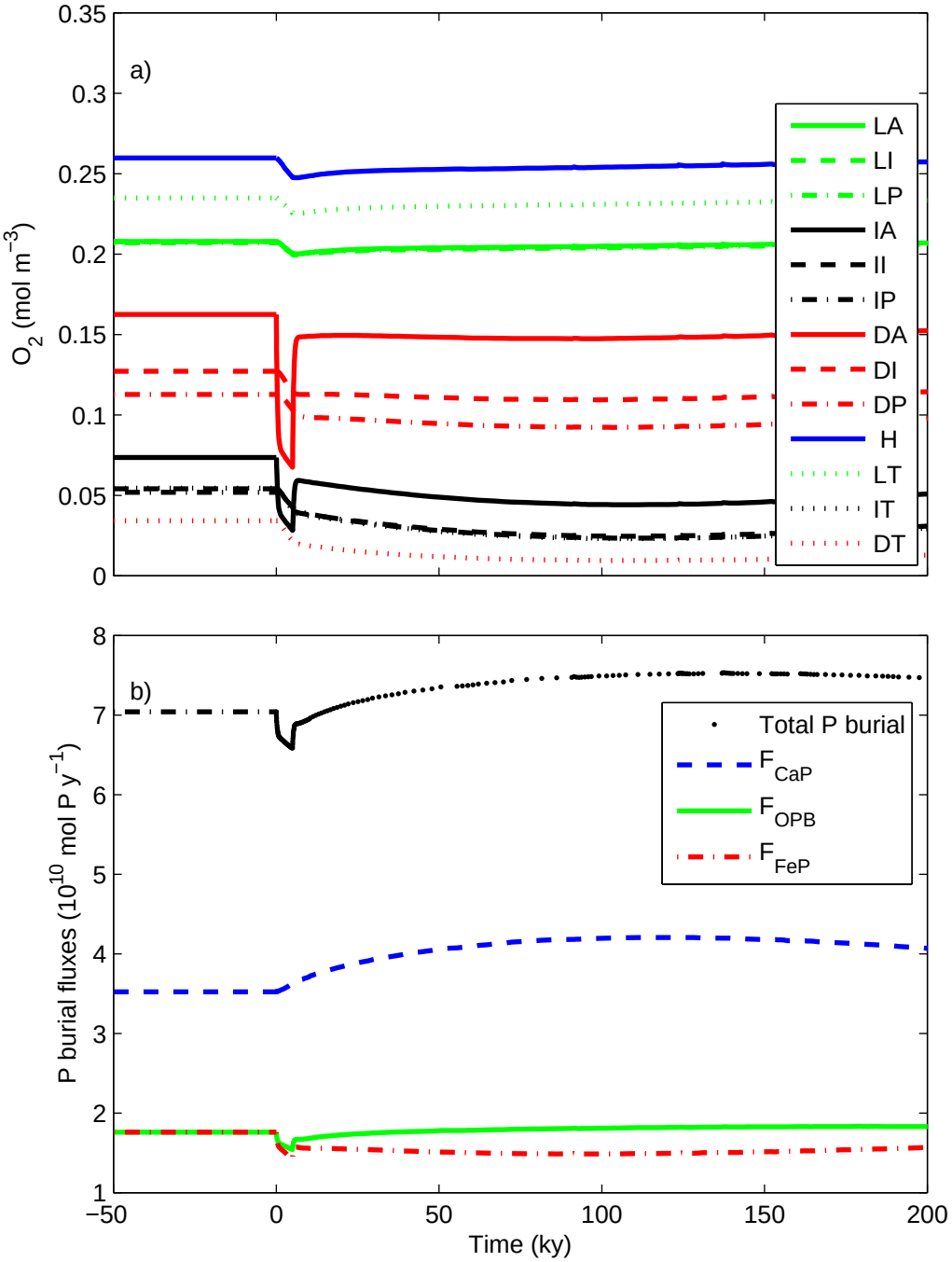

Figure 3.4: Summary of LOSCAR-P sensitivity experiments to the initial fraction of organic phosphorus (f_{OP}) and organic carbon buried (f_{OC}) in the deep ocean shown in the Supplement (Figure 3.11). a) Excess carbon burial over 200 ky as a function of the initial organic carbon burial flux b) Excess carbon burial over 200 ky as a function of the initial organic phosphorus burial flux c) The combined effect of f_{OC} and f_{OP} on excess carbon burial over 200 ky. The same color coding for f_{OC} is applied as in Figure 3.11: diamonds, circles and crosses correspond to $f_{OP} = 0.25$, 0.50, and 1.00%, respectively; green, black, and red colors correspond to $f_{OC} = 0.50$, 1.00, and 2.00%, respectively.

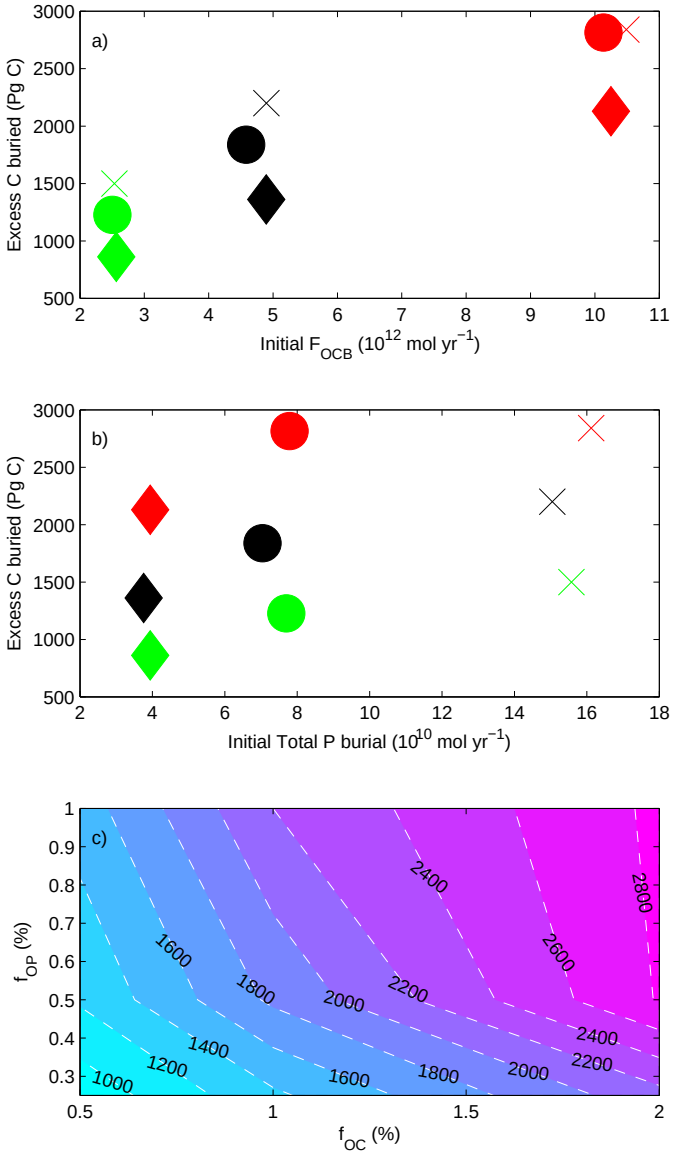

Figure 3.5: Comparison of responses of original LOSCAR and LOSCAR-P to the PETM scenario including the "leak" of carbon over 42,000 years during the main phase. a) Carbon release scenarios: Every simulation shown here has a main emission of 3000 Pg C over 5 ky, followed by an additional leak of 1,480 Pg C, except for the "strong leak" simulation (denoted in green), which has a leak of 2,500 Pg C. b) Atmospheric CO_2 c) Mean surface δ^{13}C d) Organic carbon burial flux e) Total reactive P flux (F_{Cap} + F_{OPB}+ F_{FeP}).

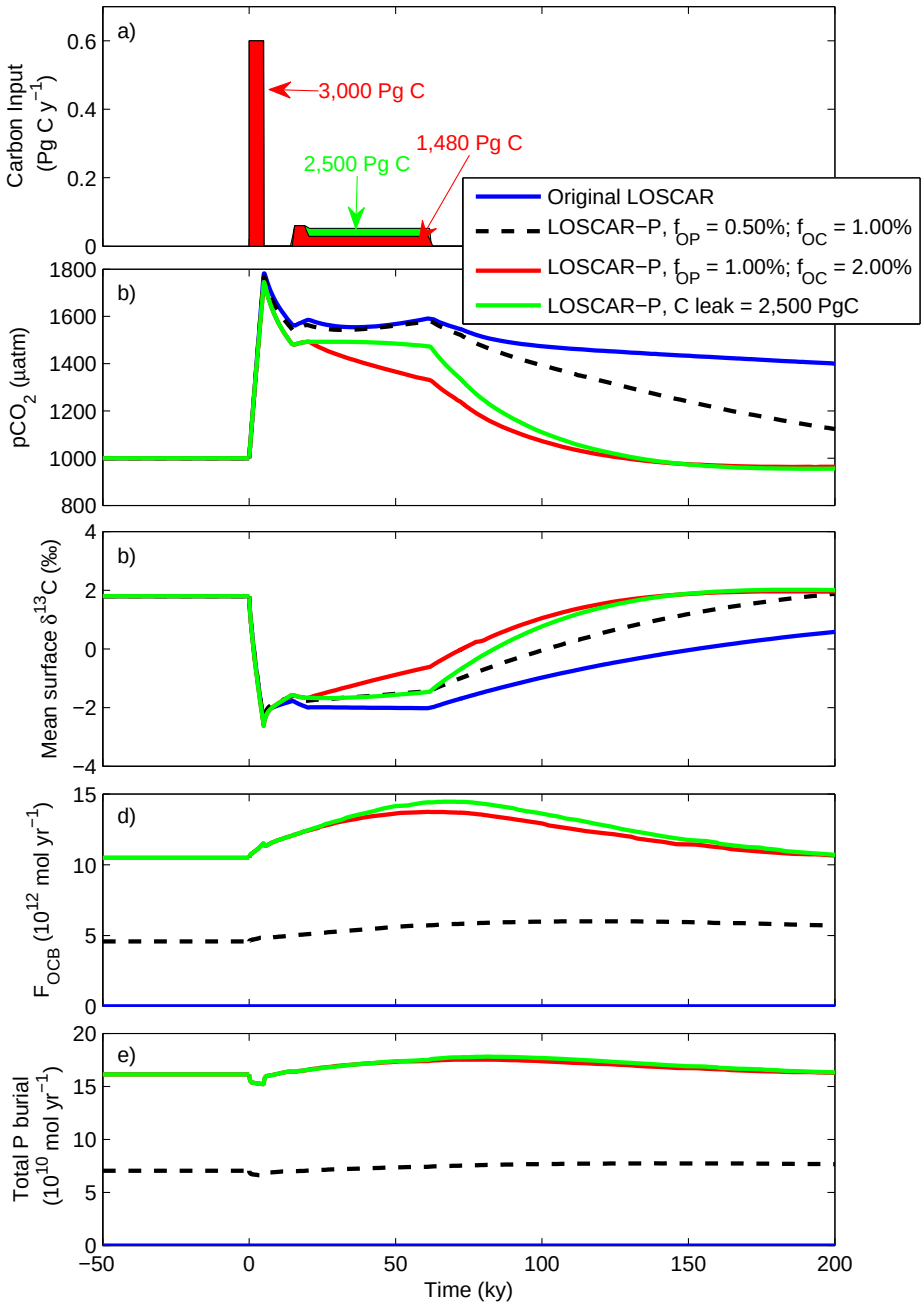

Figure 3.6: CCD and sediment $CaCO_3$ wt% evolution in the Atlantic ocean (corresponding to runs shown in Figure 3.5). a) Atlantic CCD. b) Atlantic $CaCO_3$ content of the 3000, 3500, 4000, and 4500 m sediment boxes for the"stronger leak" scenario (green line in panel "a"; leak = 2,500 Pg C). Red lines are $CaCO_3$ weight content data from *Penman et al.* [2016].

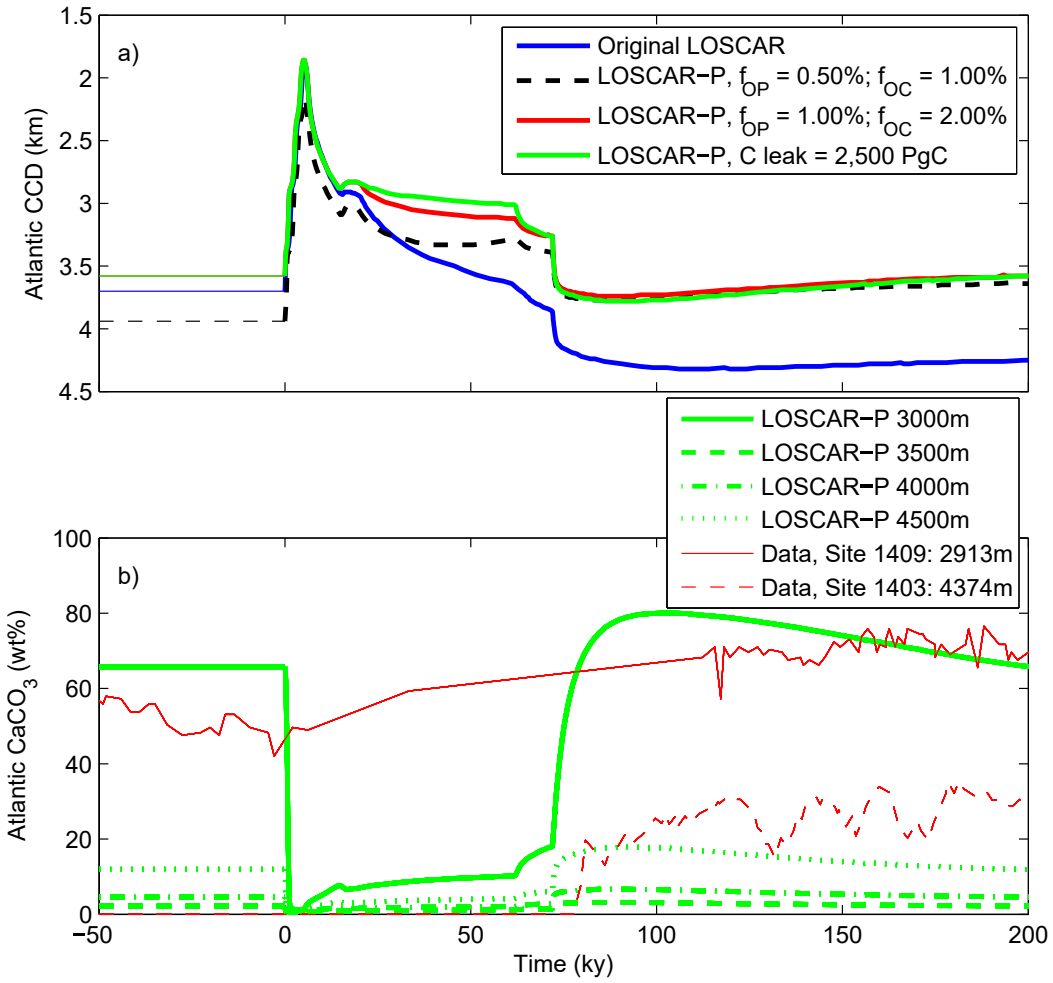

Figure 3.7: Excess cumulative burial of organic carbon. The black and red lines represent data collected from Bass River and Lodo Gulch, respectively (data from *John et al.* [2008] that they used to calculate upper and lower global organic C burial across the PETM). The green line is the cumulative accumulation rate of organic C predicted by LOSCAR-P preferred scenario, assuming the continental shelf area of Eocene was twice that of present day. Present day shelf area = 26×10^6 km^2 *Walsh et al.* [1991].

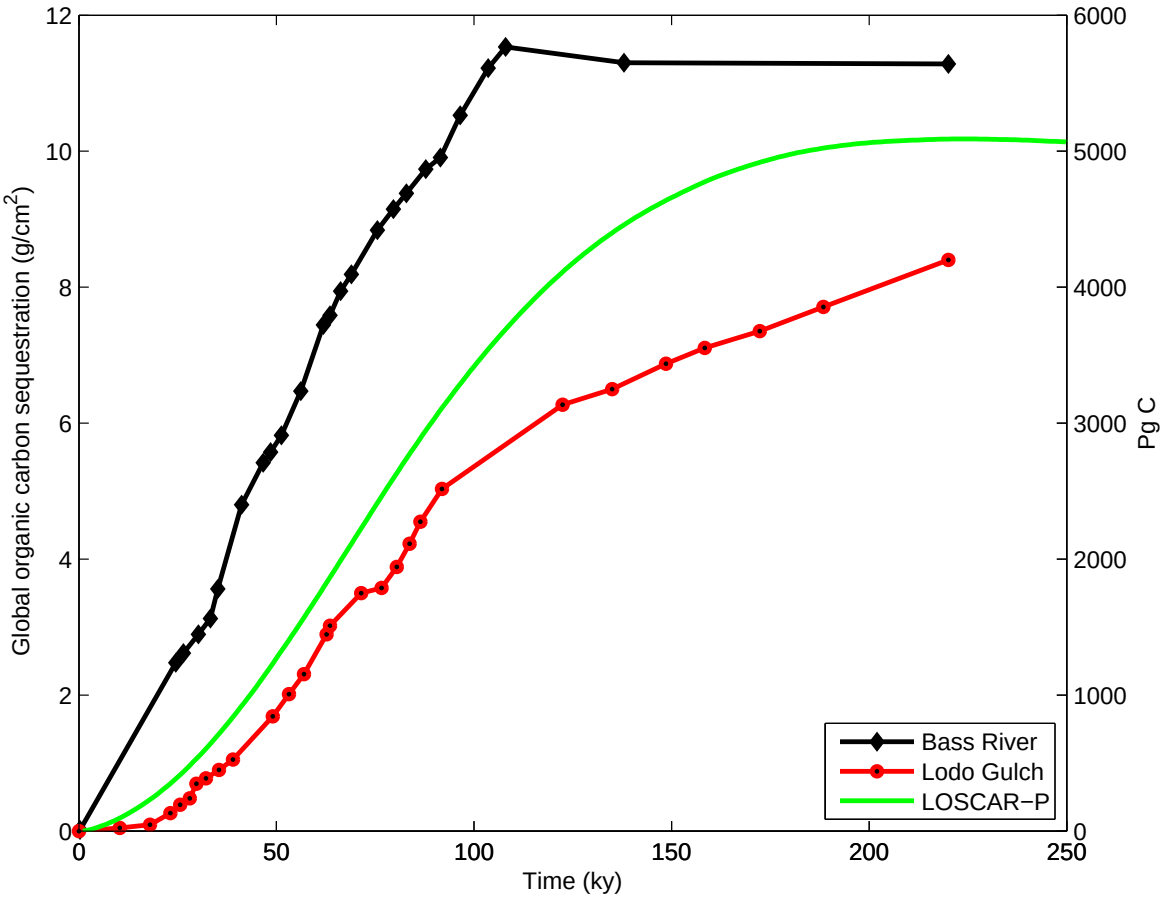

Figure 3.8: Sensitivity of LOSCAR-P to the weathering feedback strength. Each of the simulation has the same carbon input scenario, which is identical to the "stronger leak" scenario displayed in Figures 3.5 and 3.6. nC and nS are carbonate and silicate weathering feedback parameters, respectively. nC and nS are by default set to 0.4 and 0.2, respectively, and the default value is used in all other simulations. a) Atlantic CCD sensitivity to the weathering feedback strength. b) Atlantic $CaCO_3$ content in sediments at depth of 4500 and its sensitivity to the weathering feedback strength.

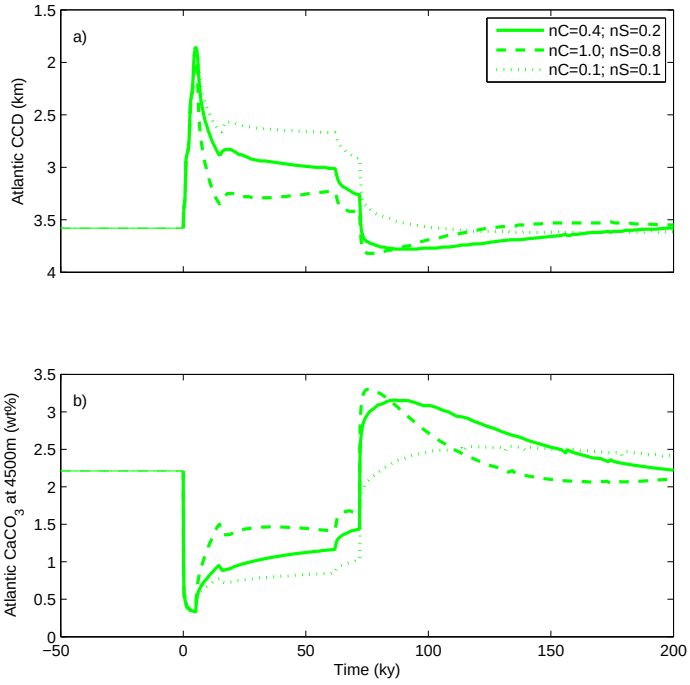

Figure 3.9: CCD and sediment $CaCO_3$ wt% sensitivity to $CaCO_3$ rain. Green line represents the preferred scenario, C leak = 2,500 Pg C. Black lines represent a scenario in which $CaCO_3$ is kept constant at the initial value. a) Atlantic CCD. b) Atlantic $CaCO_3$ content of the 3000, 3500, 4000, and 4500 m sediment boxes for the"stronger leak" scenario. Red lines are $CaCO_3$ weight content data from *Penman et al.* [2016].

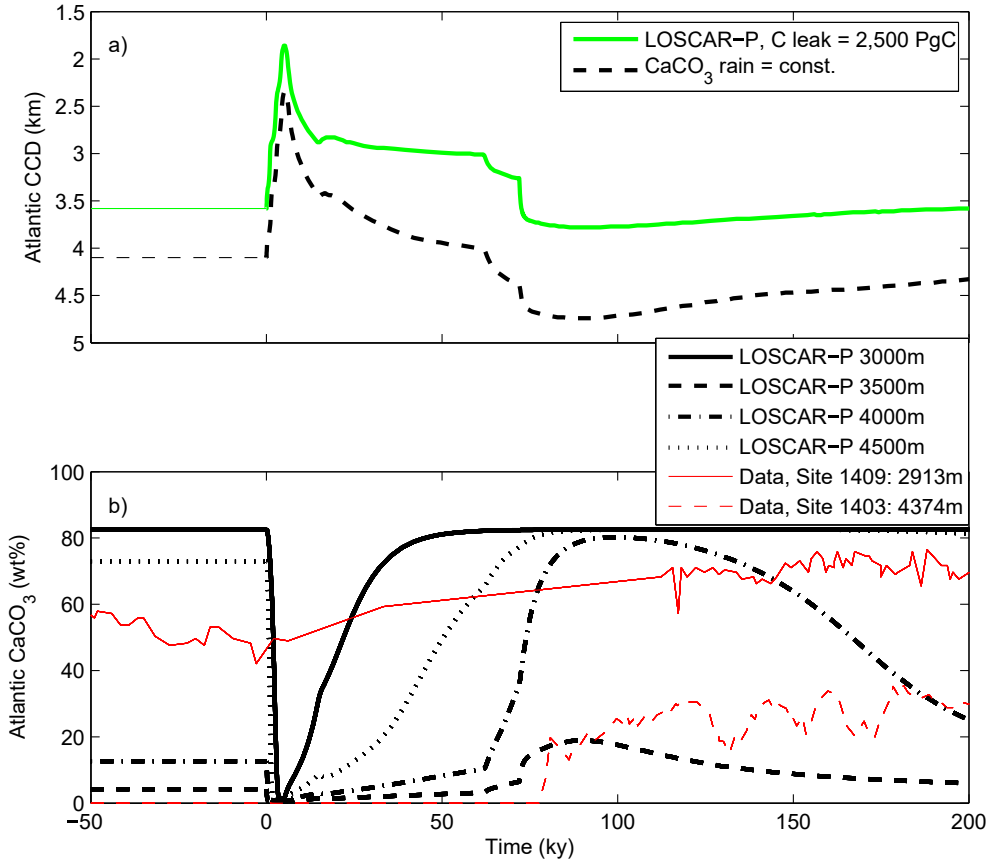

Table 3.1: Steady-state fluxes for the standard model run.

Fluxes:			
F_{Cexp}	Carbon export flux	4.6 $\times 10^2$ Tmol yr^{-1}	
F_{Pexp}	Biological fixation of reactive P	3.52 Tmol yr^{-1}	$\frac{F_{Cexp}}{130}$
F_{OCB}	Org. C burial	4.6 Tmol yr^{-1}	1% of F_{Cexp}
F_{OPB}	Org. P burial	1.76 $\times 10^{10}$ mol yr^{-1}	$\frac{F_{ocb}}{260} = 0.5\%$ of F_{Pexp}
F_{CaP}	CaP burial	3.52 $\times 10^{10}$ mol yr^{-1}	50% of total POP
F_{FeP}	FeP burial	1.76 $\times 10^{10}$ mol yr^{-1}	25% of total POP burial
F_{OCW}	Kerogen oxidation	4.6 Tmol yr^{-1}	for steady-state
F_{PW}	Phosphate weathering flux	7.04 $\times 10^{10}$ mol yr^{-1}	for steady-state

3.7 Supplementary Material for Redox-controlled carbon and phosphorus burial: A mechanism for enhanced organic carbon sequestration during the PETM

3.7.1 Sensitivity studies

3.7.2 Oxygen sensitivity

We assessed the sensitivity of the model to the Deep Atlantic Oxidation (DAO), by varying DAO from 0% (the entirety of carbon is oxidized in the atmosphere, Figure 3.10) to 100% (carbon is fully oxidized in the deep Atlantic ocean). It turned out that DAO has a negligible effect on overall excess carbon burial and carbon isotope recovery during the PETM (Figure 3.10).

3.7.3 Initial organic C and organic P burial sensitivity

Because of the uncertainty associated with the magnitude of the global P weathering and burial fluxes as well as kerogen oxidation and carbon burial, we cover a wide range of scenarios by doubling or halving (relative to the control run) the amount of organic P and/or C that is initially buried in the sediments (Figure 3.11). Note that in the control run f_{OP} and f_{OC} were set to 0.50% and 1.00%, respectively. Larger initial organic carbon burial rates result in greater excess organic carbon burial during the entire PETM. Also, for the same initial organic carbon burial rate, more carbon is buried with increasing initial P burial rate. Overall, the model is more sensitive to the initial amount of organic carbon burial than to

the initial P burial, especially at high initial carbon burial rates (see main text). The amount of excess carbon burial over 200 ky ranges from 860 Pg C ($f_{OP} = 0.25\%$ and $f_{OC} = 0.50\%$) to 2,840 Pg C ($f_{OP} = 1.00\%$ and $f_{OC} = 2.00\%$).

3.7.4 The capacitor effect

There might be an alternative explanation for a rapid PETM termination phase. As mentioned in the main text, the carbon during the onset and main phase of the PETM could have been introduced into the ocean-atmosphere system through dissociation of marine methane hydrates *Dickens et al.* [1995]; *Dickens* [2003, 2011]. A more detailed assessment of a methane hydrate capacitor and its dynamics and role during the PETM and during the Late Paleocene-Early Eocene is given in *Dickens* [2011] and *Komar et al.* [2013]. An in-depth description of the capacitor is beyond the scope of this study but information relevant to the model experiments performed below that involve a capacitor are outlined here. A supply of methane to the capacitor comes through methanogenesis (F_{METH}) of conventional organic carbon that is buried in the sediments. Methane from the capacitor returns to the ocean through anaerobic oxidation of methane (F_{AOM}). The balance between the F_{METH} and F_{AOM} fluxes determines the rate at which the capacitor recharges. Therefore, when these two fluxes are equal the mass of the capacitor remains constant. The F_{METH} and F_{AOM} fluxes in previous modeling studies of short-term negative $\delta^{13}C$ excursion during the PETM were assumed to be 0.6 $\times 10^{12}$ mol C yr^{-1} at steady state *Dickens* [2003]. A study of long-term carbon cycle trend during the Late Paleocene and Early Eocene *Komar et al.* [2013] requires these two fluxes to be larger, 1.0 $\times 10^{12}$ mol C yr^{-1}. The isotopic signature of F_{METH} and F_{AOM} flux may be very depleted in ^{13}C (up to $-70‰$ *Dickens* [2011]).

As the massive input of ^{13}C-depleted carbon from a methane hydrate capacitor arrives to the ocean-atmosphere system during the onset and the main phase of the PETM, the capacitor itself becomes depleted, so the steady-state input of ^{13}C-depleted carbon from the capacitor though F_{AOM} has to decrease during the recovery phase of the PETM. In other words, if the F_{AOM} flux decreases and F_{METH} stays the same, the capacitor will begin to recharge. This in turn should cause a rise in δ^{13}C of the ocean. We simulated this behavior by using the aforementioned Paleocene-Eocene F_{METH} and F_{AOM} rates (Figure 3.12). The net organic carbon storage (Figure 3.12a) for the capacitor simulations (magenta and black lines) represents the difference between F_{METH} and F_{AOM}, and for the preferred LOSCAR-P run (green line), it is excess organic carbon storage (organic carbon burial at time t minus the initial, steady-state organic carbon burial rate). To cover a wide range of possible scenarios, the two capacitor experiments (magenta and black lines) assume the upper (F_{AOM} = 1.0 $\times 10^{12}$ mol C yr^{-1}; ^{13}C = -70‰) and lower (F_{AOM} = 0.6 $\times 10^{12}$ mol C yr^{-1}; ^{13}C = -50‰) flux estimates, respectively. To achieve the most extreme response, it was assumed that F_{AOM} completely ceases at the beginning of the recovery interval and remains at 0 throughout the entire recovery phase. The total duration of the interval over which the net storage occurred was set to 40 ky, which is the total duration of the PETM recovery phase (between 60 ky and 100 ky after the onset of the PETM; Figure 3.12). The lower amount of carbon stored in the capacitor during this time interval is ~300 Pg C (Figure 3.12a; black line). The upper amount of carbon stored during the PETM end phase is ~500 Pg C (Figure 3.12a; magenta line). Even though the isotopic value of carbon recharging the capacitor is very negative, the overall relatively small amount of carbon being stored results in a small change in surface ocean δ^{13}C (Figure 3.12c) compared to that caused by the organic C burial that arises from

the C-O-P feedback (Figure 3.12; green). Note also that the C-O-P feedback removes light carbon over a much longer interval than the capacitor because the former can be active while the latter exhibits strong net discharge. A capacitor alone cannot strongly discharge and recharge at the same time, which limits its carbon removal interval to the recovery phase. Unless the rates of capacitor recharge were much higher than assumed here, we conclude that the refilling of the capacitor could not have been solely responsible for the observed fast PETM recovery but might have contributed to the trend.

3.7.5 δ^{13}C Record

Before comparing the modeled δ^{13}C results and observations it is important to discuss discrepancies associated with the data records of δ^{13}C. The δ^{13}C recovery times during the PETM are highly uncertain. Not only do they vary between different age models but also between drilling sites when the same age model is applied. For example, there is an inconsistency in ^{3}He model between sites 690 and 1266 (Figure 3.13). Site 1266 exhibits a 100 ky recovery whereas the recovery time for site 690 is around 30-40 ky using the ^{3}He age model. *Bowen and Zachos* [2010] used the most extreme case based on ^{3}He age model, which produces the most rapid δ^{13}C recovery and thus requires a larger increase in organic C burial in order to explain the observations. As opposed to age models based on ^{3}He concentration, cycle-based models generally display a shorter PETM main phase but a longer recovery period *Murphy et al.* [2010]. This translates into a lower rate of change in δ^{13}C during the termination stage of the PETM and consequently demands a smaller increase in organic C burial to account for observations. Therefore, sequestration of 2,000 Pg C during the end-phase of the PETM calculated by *Bowen and Zachos* [2010] necessary to explain the rate of CIE recovery might

be an upper limit.

Figure 3.10: Sensitivity of the LOSCAR-P model to the fraction of carbon oxidized in the Atlantic deep ocean. a) Atmospheric CO_2 b) Mean surface $\delta^{13}C$ c) Organic carbon burial flux d) Total reactive P burial flux (F_{Cap} + F_{OPB}+ F_{FeP}).

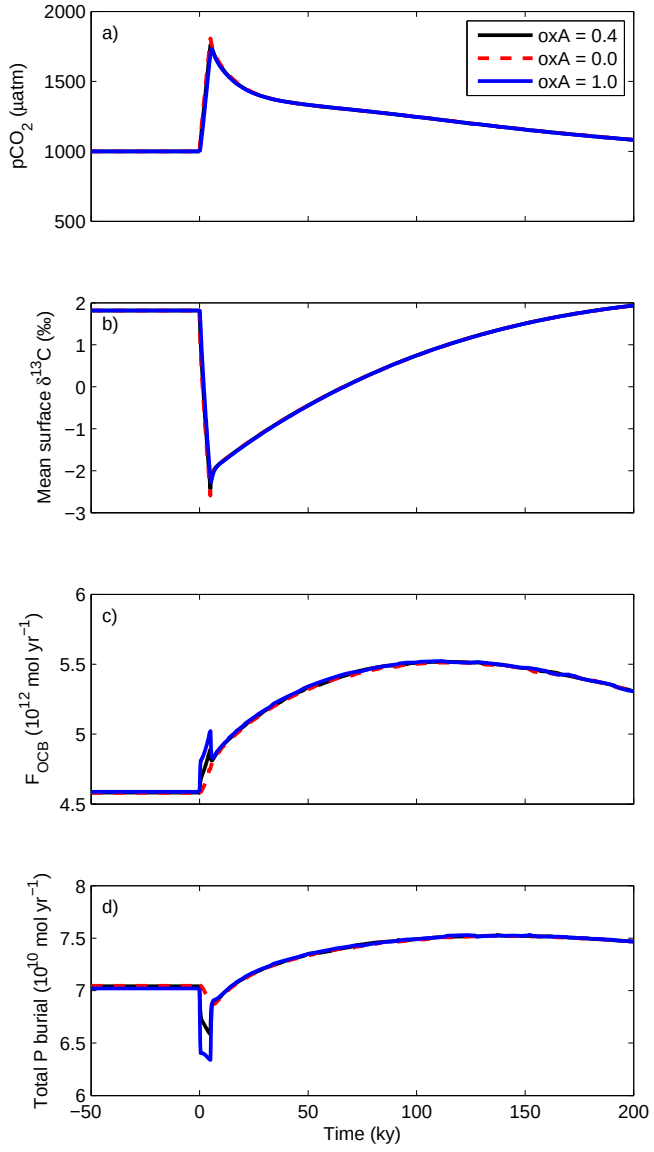

Figure 3.11: LOSCAR-P sensitivity to the initial fraction organic phosphorus (f_{OP}) and organic carbon buried (f_{OC}) in the deep ocean. a) Atmospheric CO_2 b) Mean surface $\delta^{13}C$ c) Organic carbon burial flux d) Total reactive P flux (F_{Cap} + F_{OPB}+ F_{FeP}). Sets of different line styles represent different f_{OP} fractions: solid line=1.00%, dashed line 0.50%, and dotted-dash line = 0.25%. f_{OC} fractions are color coded so that black lines represent 1.00%, green lines correspond to 0.50%, and red lines are 0.25%. Different fractions determine the initial rate of the organic phosphorus and carbon burial fluxes.

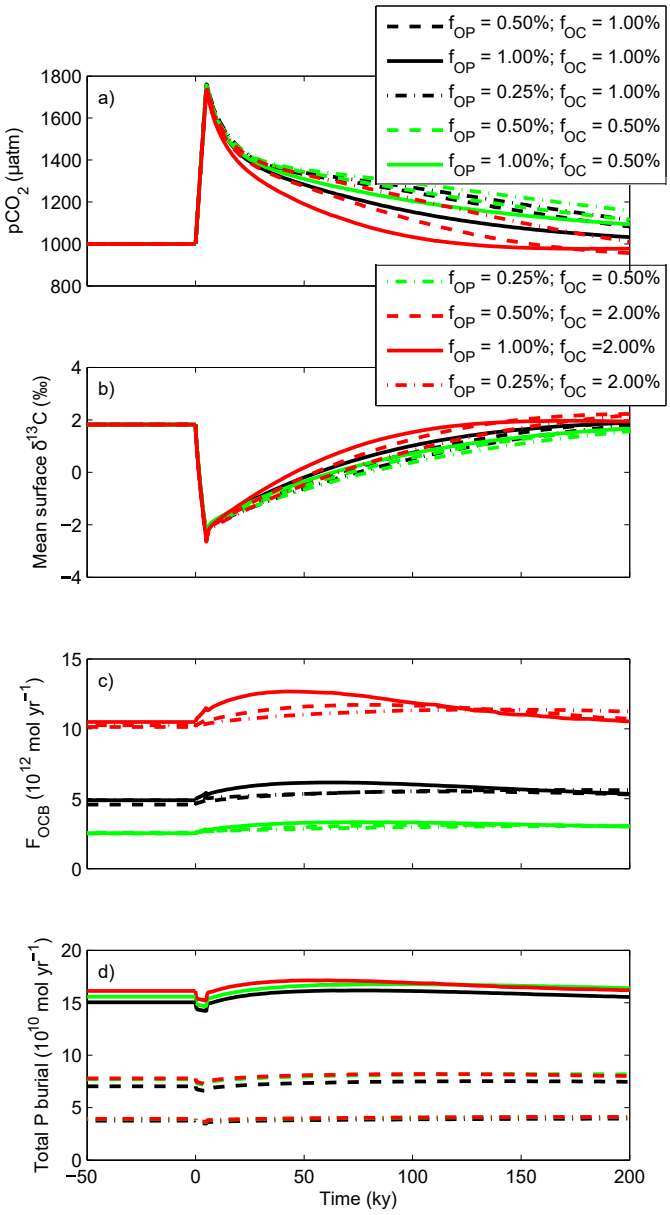

Figure 3.12: The response of the ocean-atmosphere system to an increased net organic carbon storage rate. a) Net organic carbon recharge rate of an organic capacitor b) Atmospheric CO_2 c) Mean surface ocean $\delta^{13}C$. The fast methane capacitor rate of recharge is 1.0 $\times 10^{12}$ mol C yr^{-1} between 60ky and 100ky, amounting to a total of about 500 Pg C and the ^{13}C of the flux is $-70‰$ (magenta). The slow methane capacitor rate of recharge is 0.6 $\times 10^{12}$ mol C yr^{-1} between 60ky and 100ky, amounting to a total of about 300 Pg C and the ^{13}C of the flux is set to $-50‰$ (black).

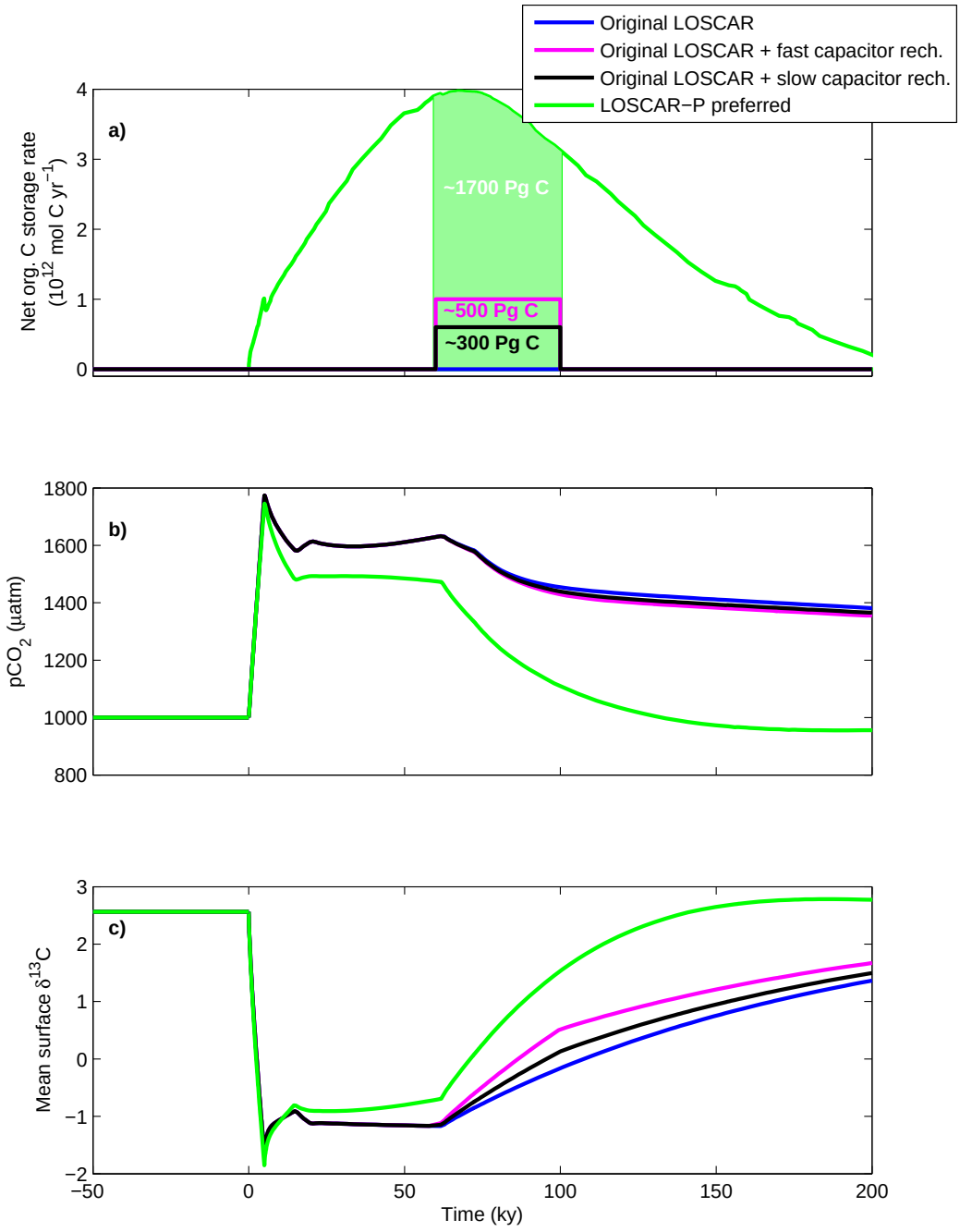

Figure 3.13: Bulk carbonate δ^{13}C record from a) ODP site 690, b) ODP site 1266. Black lines denote ages determined using extraterrestrial ^{3}He concentration *Farley and Eltgroth* [2003]; *Murphy et al.* [2010], green lines represent ages that were resolved based on cycle stratigraphy *Röhl et al.* [2007].

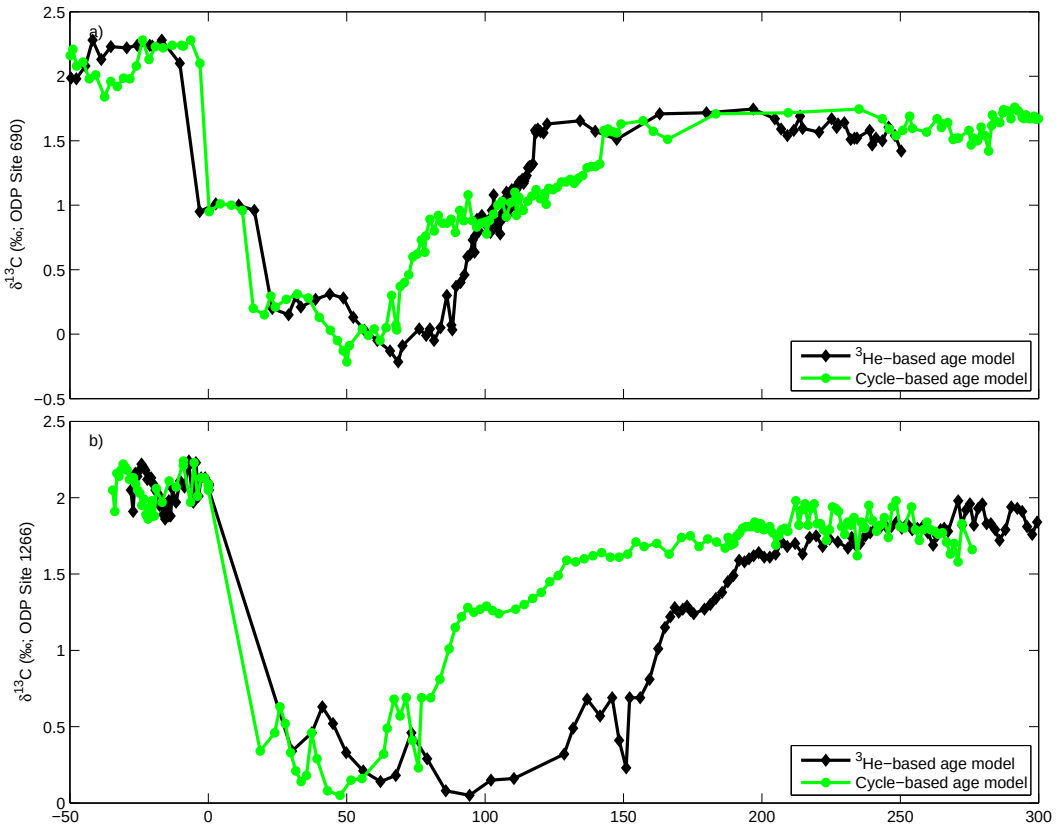

CHAPTER 4
MODELING THE EVOLUTION OF OCEAN CARBONATE CHEMISTRY, CARBONATE COMPENSATION DEPTH, ATMOSPHERIC CO_2, AND CLIMATE OVER THE CENOZOIC

ABSTRACT

The Cenozoic era (66-0 Ma) is marked by significant long-term trends and aberrations in carbon cycling and climate shifts. The most notable long-term features of this epoch include a ∼6 My long warming trend between 58 and 52 Ma (Late Paleocene and Early Eocene, LPEE) characterized by a negative excursion of both oxygen (δ^{18}O) and carbon (δ^{13}C) stable isotopes, indicating global warming (>4^{o}C) and reordering in carbon cycling. Concomitant with the temperature rise was a global deepening of the carbonate compensation depth (CCD) of at least 500 m. However, over the past 50 Ma, δ^{18}O and δ^{13}C evidence, along with atmospheric pCO_2 proxies, and carbonate accumulation rates indicate global cooling and a permanent CCD deepening (>1,000 m). Here, we investigate possible mechanisms responsible for the observed long-term trends by utilizing numerical modeling. The model employed is a combination of the well-established carbon cycle models GEOCARB III and LOSCAR which enables simulation of atmospheric pCO_2, ocean carbonate chemistry, the CCD, and ocean δ^{13}C. The model was expanded to include the long-term phosphorus cycle, which allows predictive organic carbon export and organic carbon burial. We explored several different scenarios, with the goal of achieving data-consistent variations in ocean δ^{13}C, atmospheric pCO_2, and the CCD. The results suggest that organic carbon burial rates were altered due to the universal effect of temperature on metabolic rates. The ability to simulate the CCD changes, along with organic carbon burial rates imposes a significant constraint on carbon fluxes in the model. The results indicate that the pCO_2-weathering feedback operated during the Cenozoic, with weathering rates decreasing as the pCO_2 dropped, while the CCD deepened. This requires a decoupling of the CCD from silicate and carbonate weathering

rates, for which we suggest two dominant mechanisms: (a) shelf-basin carbonate burial fractionation and (b) decreasing respiration of organic matter at intermediate water depths as the Earth transitioned from the greenhouse conditions of the Eocene to the colder temperatures of the Oligocene. Overall, we found that the model is able to capture the first-order changes in reconstructed atmospheric CO_2, surface ocean pH, ocean $\delta^{13}C$, and CCD. Unsurprisingly, however, the details of observed second-order changes in all data records is difficult to reproduce simultaneously.

4.1 Introduction

Global climate and the global carbon cycle have undergone significant change since the Early Eocene (∼50 Ma), the period of peak Cenozoic deep ocean temperatures [*Zachos et al.*, 2001; *Bijl et al.*, 2009; *Cramer et al.*, 2009]. The warming commenced during the Paleocene (∼58 Ma) and the average temperature was steadily rising (high latitude Earth's surface and deep ocean warmed by $\sim 4^{o}$C) until it reached its maximum around 6 million years later (Figure 5.1a) [*Zachos et al.*, 2001; *Bijl et al.*, 2009; *Westerhold et al.*, 2011]. The temperature increase during the Late Paleocene-Early Eocene (LPEE) was accompanied by a long term decrease in δ^{13}C in both surface and deep ocean (Figure 5.1b), probably indicating a drop in the net organic carbon output from the ocean and atmosphere [*Komar et al.*, 2013]. This warming interval of the Cenozoic was punctuated by a series of short-lived hyperthermals, transient warming events superimposed on the long-term warming, with the Paleocene-Eocene Thermal Maximum (PETM) being the most prominent one (see Chapter 3). As we are interested in the long-term trends, the short-lived events, such as hyperthermals will not be the focus of this chapter.

Since the Cenozoic temperature maximum, the Earth system has experienced gradual cooling, which eventually resulted in major glaciation and ice caps forming at high latitudes, as reflected in δ^{18}O [*Zachos et al.*, 2001; *Cramer et al.*, 2009]. Evidence suggests that the primary cause of the long-term cooling was a decreasing concentration of atmospheric CO_2 (Figure 5.1c) [*Beerling and Royer*, 2011; *Zhang et al.*, 2013] but the reason behind the CO_2 decline remains enigmatic. Concurrent with the cooling is a deepening of the calcite compensation depth (CCD). The CCD is the depth where the rain of calcite to the sediments is balanced by dissolution, so that sediments at this depth bear less than 5 or 10 weight percent

$CaCO_3$ [e.g. *Ridgwell and Zeebe*, 2005]. Therefore, the paleo-CCD position can be retrieved by inspecting the $CaCO_3$ content of the sediment cores [*van Andel and Moore*, 1974; *Pälike et al.*, 2012; *Slotnick et al.*, 2015]. As the carbonate preservation in the sediments is mostly a function of the carbonate saturation state of the ocean, the position of the CCD will reflect changes in carbonate saturation. The deep-sea carbonate records indicate that the Pacific CCD deepened over 1 km, from ∼3.0 - 3.5 km in the earliest Eocene to about 4.6 km at present [*van Andel and Moore*, 1974; *Pälike et al.*, 2012]. Similar trends are also observed in the Atlantic and Indian basins (Fig. 5.1d).

On geological time scales, the carbon content of the atmosphere is controlled by the balance of carbon sources and sinks to and from the ocean-atmosphere system (surficial system). The major sources of carbon are mantle degassing (volcanic outgassing/metamorphic activity) and kerogen oxidation. Carbon is removed from the surficial system and stored in rocks (geologic system) via weathering of silicate rocks, and carbonate and organic carbon burial [*Berner et al.*, 1983; *Berner*, 1999]. Thus, as the balance between sources and sinks of carbon governs the atmospheric CO_2 concentration, and therefore the carbonate saturation state of the ocean [*Zeebe and Westbroek*, 2003], the combined effect of carbon cycle dynamics over time is reflected in the variable position of the CCD. Hence, tracing the CCD evolution across the Cenozoic and identifying mechanisms responsible for its fluctuations is important in deconvolving past changes in atmospheric CO_2, weathering, and deep-sea carbonate burial (see below).

The cycling of carbon during the Cenozoic era, especially in the past 50 Ma, is somewhat of a conundrum. While CO_2 degassing rates have stayed constant or decreased over this time period [*Berner et al.*, 1983; *Müller et al.*, 2008; *Van Der Meer et al.*, 2014], atmospheric

CO_2 concentration steadily declined [*Beerling and Royer*, 2011; *Zhang et al.*, 2013]. The concentration of CO_2 in the atmosphere exerts one major control on global temperature. Lower CO_2 concentrations in the atmosphere lead to colder temperatures and a weakened hydrological cycle, which results in decelerated weathering rates. Slower weathering rates would lower ocean alkalinity and ultimately result in the CCD shoaling. Nevertheless, the sediment carbonate records reveal that the Pacific CCD deepened over 1 km since 50 Ma [*van Andel and Moore*, 1974; *Pälike et al.*, 2012], contrary to the expectations.

Numerous modeling studies have modeled the evolution of carbon cycle, long-term climate, and/or oceanic carbonate chemistry during the Cenozoic [e.g. *Berner et al.*, 1983; *Berner and Kothavala*, 2001; *Wallmann*, 2001; *Arvidson et al.*, 2006; *Li and Elderfield*, 2013; *Caves et al.*, 2016]. However, all these studies lack an indispensable part of the long-term carbon cycle, the CCD, which is as noted above, essential for understanding the climate of the past. To the best of my knowledge, this is the first modeling study that investigates carbon cycling across the Cenozoic with a full-fledged ocean carbonate chemistry model that also incorporates a marine sediment component, crucial for the CCD reconstruction. Here, we use an expanded version of the LOSCAR model (Long-term Ocean-Atmosphere Sediment CArbon cycle Reservoir; *Zeebe* [2012a]) called LOSCAR-P, which combines the long-term phosphorus (P) and carbon cycle (*Komar and Zeebe* [2017]; see Chapter 3) coupled to the modified version of GEOCARB III model [*Berner and Kothavala*, 2001]. Because the LOSCAR-P version used in this study is slightly different to that used in Chapter 3 (see Section 4.2.2), we refer to it as LOSCAR-P2.

Any model explaining carbon cycling over multi-million year time scales should account for all aspects of the carbon cycle affecting CO_2 [*Berner and Berner*, 1997]. Both the original

LOSCAR model and GEOCARB lack a long-term P cycle, thus neglecting the influence of the marine biota on long-term C cycling. On long time scales, dissolved phosphorus is a biolimiting nutrient in the ocean [*Tyrrell*, 1999] and therefore the primary regulator of organic matter production [*Sarmiento and Gruber*, 2006]. As such, the C and P cycles are linked because the availability of dissolved P affects the rate of organic carbon burial [*Van Cappellen et al.*, 1996; *Kump et al.*, 2000]. Another link is through atmospheric pCO_2. High pCO_2 and therefore accelerated weathering fluxes could in theory also intensify the supply of nutrients to the ocean [*Flögel et al.*, 2011], potentially leading to higher biological carbon production and export, and ultimately to higher carbon burial. This close connection between the P and C cycles is the rationale for expanding the original LOSCAR model to also include a long-term P cycle.

This modeling exercise reconciles the observed CCD, pCO_2, temperature, and carbon isotope changes during the Cenozoic. Such modeling should allow better understanding of mechanisms responsible for the long-term cooling of the Earth system and will improve our understanding of carbon cycle dynamics across the studied time interval. The model predicted evolution of the CCD imposes a much needed additional constraint on the carbon cycle, allowing for a first order attempt at quantification of weathering fluxes over the past $\sim$60 Ma, which in turn yields a better understanding of the relationship between pCO_2, weathering rates, and $CaCO_3$ burial across the studied period.

4.2 Methods

4.2.1 Model description

The overall modeling framework in this study combines and expands two geochemical models: LOSCAR (Long-term Ocean-atmosphere Sediment CArbon cycle Reservoir) and GEOCARB III. The details of the two models (in their original form) are thoroughly documented in *Zeebe* [2012a] and *Berner and Kothavala* [2001], thus we refrain from providing a detailed description of all of the models' components and designs here. However, the modifications applied to the original versions of each model as well as the connection between the models will be discussed here.

GEOCARB III considers processes of carbon transfer between geologic reservoirs and the atmosphere-ocean system and thus provides information about fluxes of carbon between different carbon pools on long time scales. The fluxes of carbon amongst different carbon reservoirs control the atmospheric CO_2 concentration. Over this time period, the CO_2 is stabilized through the silicate weathering-pCO_2 feedback, in which pCO_2 adjusts in order to balance fluxes. GEOCARB III, however, does not resolve ocean chemistry and does not include sediments and hence cannot predict the CCD. For this reason, GEOCARB was coupled with the LOSCAR model, which accounts for the marine carbon system and sediments.

LOSCAR is a carbon cycle box model that can operate on both short-term (centuries) and long-term (millions of years) time scales, efficiently computing the partitioning of carbon between various model components (ocean, atmosphere and sediments) but unlike GEOCARB, it does not include the geologic carbon cycle, so the two complement each other. In LOSCAR, the world oceans are represented with three (four in the paleo version) major ocean reservoirs

(Atlantic, Indian, Pacific, and Tethys in the paleo set-up). Each of the basins is subdivided into three different boxes (shallow, intermediate, and deep) and there is one generic box representing the high latitude ocean. Thus, there is a total of ten (thirteen in the paleo version) ocean boxes plus an additional box representing the atmosphere. The model keeps track of various biogeochemical tracers (including total carbon-TC, total alkalinity-TA, stable carbon isotopes-$\delta^{13}C$, and others) in the different boxes. Using the model predicted concentrations of TC and TA in the individual ocean boxes, and supplying them to the chemistry routines described by *Zeebe and Wolf-Gladrow* [2001], parameters such as $[CO_2]$, $[CO_3^{2-}]$, pH and calcite saturation state are calculated. The chemical routines allow for variations in the $[Ca^{2+}]$ and $[Mg^{2+}]$ of seawater as well as for the temperature changes. This is critical because varying Mg/Ca ratio and temperature affect the thermodynamics (e.g. equilibrium constants and solubility products of chemical reactions), and therefore can alter the predicted ocean carbonate chemistry and atmospheric pCO_2. As both ocean temperature and Mg/Ca ratio have varied considerably over the simulated period the model had to be adjusted accordingly (see Section 4.2.2).

4.2.2 Model modifications, data acquisition, and model coupling

GEOCARB module

The input data used in the original GEOCARB III model is relatively coarse, with a resolution that exceeds 10 million years. As the primary purpose of the original GEOCARB model was describing the behavior of carbon cycle across the entire Phanerozoic ($\sim$ 570 Ma), this type of accuracy is justified. Nevertheless, any events that occurred on time scales shorter than 10 Ma could not be properly modeled and such a model would be impractical for the purposes

of this study.

One of the main model inputs is the δ^{13}C of bulk sediments [*Veizer et al.*, 1999], which is used to calculate burial rates of carbonate carbon and organic carbon. Using the δ^{13}C data of bulk sediments that have a resolution greater than 1 million years (1 Myr is the time-step of GEOCARB) is therefore crucial. Fortunately, since the model inception, numerous carbon isotope data sets with a higher resolution and updated age models have become available [e.g. *Zachos et al.*, 2001; *Kurtz et al.*, 2003; *Cramer et al.*, 2009; *Westerhold et al.*, 2011; *Dickens and Backman*, 2013]. GEOCARB was thus accordingly modified to utilize the new data sets in order to capture the processes of the long-term carbon cycle during the Cenozoic more accurately. This modified version is referred to as the GEOCARB module.

The δ^{13}C data implemented by the original GEOCARB III model were replaced by two data sets of much higher temporal resolution, placed on a current timescale. For the time period between 58 and 48 Ma we use δ^{13}C records at Deep Sea Drilling Projects Sites 527 and 577 [*Dickens and Backman*, 2013; *Komar et al.*, 2013]. The remainder of the δ^{13}C record (48 Ma to present) comes from the bulk sediment δ^{13}C data presented in *Kurtz et al.* [2003]. To prevent rapid and abnormal model fluctuations produced by abrupt changes in δ^{13}C data caused by the hyperthermal events and other short-lived events during the Cenozoic, the data was smoothed using a local linear kernel estimator with a constant bandwidth of one million years [*Samworth and Poore*, 2005; *Poore et al.*, 2006]. This approach is justified because the focus of this study is on long-term carbon cycle behavior rather than short-term variations.

LOSCAR-P2

As mentioned above, in order to capture all major processes (including biogeochemical feedbacks) affecting atmospheric CO_2 and carbon cycling on long time scales, the original LOSCAR model was modified to include the long-term phosphorus cycle. The expanded version of LOSCAR will be referred to as LOSCAR-P2 (to distinguish it from the LOSCAR-P model used in Chapter 3). The LOSCAR-P model has previously been used to explain the rapid Earth-system recovery following a carbon cycle perturbation during the PETM [see Chapter 3; *Komar and Zeebe*, 2017]. All building blocks of LOSCAR-P and therefore alterations performed on the original LOSCAR model are thoroughly discussed in Chapter 3. The same LOSCAR-P model is utilized here with several important adjustments highlighted below.

Unlike the LOSCAR modeling exercises performed in the first two Chapters, which simulate ocean-atmosphere chemistry over a few hundred thousand years, here simulations span tens of millions of years. Due to the time scale over which the simulations are performed it is crucial to account for changes of parameters which exert great influence on marine carbonate chemistry across the Cenozoic. The original LOSCAR model has two different configurations and thus two sets of boundary conditions; one for modern ocean and the other representing the Late Paleocene conditions. In order to fill the gap, the boundary condition parameters for other time epochs had to be reconstructed from paleo-proxies or by linear interpolation. These parameters include variable oceanic Mg^{2+} and Ca^{2+} concentrations (variable Mg/Ca ratio), and temperature. Other parameters that are considered and that are of great importance are changing bathymetry, thermohaline circulation, vertical mixing rates, the rain ratio between organic and inorganic carbon being exported from the surface ocean (r_{rain}), and the

ratio of shelf to open ocean production.

Magnesium and Calcium concentration in sea water varied throughout Earth's history. Paleo-proxies for Mg and Ca concentration in the world oceans show a monotonously increasing and decreasing trends over the Cenozoic, respectively [*Tyrrell and Zeebe*, 2004]. The changing Mg and Ca concentrations have profound implications for dissolution of $CaCO_3$ in sea water as these ions affect the ocean carbon system. Because of their importance in determining the saturation state of sea water, all simulations incorporate varying $[Mg^{2+}]$ and $[Ca^{2+}]$ based on the data compiled by *Tyrrell and Zeebe* [2004] (Figure 5.2).

Over geologic time the area, depth profiles, and volumes of ocean basins vary noticeably. The original LOSCAR model already implements realistic volumes of ocean boxes for modern ocean [*Menard and Smith*, 1966] and Late Paleocene ocean [*Bice et al.*, 1998]. The basin volumes and the depth profiles for other epochs are missing and were reconstructed by linear interpolation between the two data sets. Changes in areas of individual ocean across Eocene and Oligocene were generated by linearly interpolating between Late Paleocene [*Bice et al.*, 1998] and and Middle Miocene [*Herold et al.*, 2008] bathymetries. The evolution of ocean areas between the Middle Eocene and present was reconstructed by interpolating the Middle Miocene [*Herold et al.*, 2008] and modern [*Menard and Smith*, 1966] bathymetry. For more details on bathymetry, see *Stuecker* [2009] and *Stuecker and Zeebe* [2010] who collected the bathymetry data and performed the above mentioned interpolations.

The next set of LOSCAR parameters described below are not well constrained in deep geologic times and their modern and/or the Late Paleocene values were obtained by model tuning (except for modern thermohaline circulation). These parameters include the conveyor (thermohaline) transport, vertical ocean mixing, and r_{rain}. The modern thermohaline circu-

lation in LOSCAR is 20 Sv (1 Sv = $10^6 m^3 s^{-1}$) [*Toggweiler*, 1999] and the Late Paleocene is set to 25 Sv [*Zeebe*, 2012a]. The thermohaline transport (and other parameters outlined above) across the rest of the Cenozoic was attained by linear interpolation between the two given values (modern vs. Late Paleocene). In the modern ocean, the Thermohaline circulation is powered by sinking cold waters in the North Atlantic (North Atlantic Deep Water formation, NADW for short). This circulation scheme in the Late Paleocene was different, with cold waters forming in the Southern Ocean (SO formation). We implement a gradual shift from primarily NADW formation to SO dominated circulation between time t = 0 to t = 10 Ma. The remainder of the parameter values (vertical ocean mixing, r_{rain}, relative size of shelf versus deep ocean) were kept the same for Late Paleocene and modern ocean (Table 5.2) as in the original LOSCAR. Because of the large uncertainties and the lack of paleo-proxies associated with these parameters, a sensitivity study was performed to show the importance of each of the parameters on the model results (see Section 4.3).

The P cycle in this version of LOSCAR-P is slightly different from the one described in Chapter 3. The modern (pre-industrial) P fluxes and their boundary conditions now follow the range of values provided in *Slomp and Van Cappellen* [2007] (see Table 5.1). Because neither of LOSCAR-P models differentiate between shallow ocean and deep ocean organic P and C burial, the initial P fluxes used in LOSCAR are the sum of shallow and deep fluxes presented in *Slomp and Van Cappellen* [2007]. Unlike in Chapter 3, where the pre-PETM phosphorus fluxes were rather arbitrarily chosen and considered to be in steady-state, here the Late Paleocene (or at any point in the past) P and org C burial fluxes depend on the modern values. The modern LOSCAR-P2 model conditions assume that the P cycle is in steady-state (inputs equal outputs; see Table 5.1). The P and C burial fluxes are redox-dependent

(Chapter 3, Section 3.2.1), and in this model version, the fluxes depend on the modern deep ocean oxygen concentration. The phosphorus weathering flux (F_{pw}) is a function of silicate and carbonate weathering rates with slight modifications:

$$F_{pw} = F^0_{pw} \times \frac{(1-\beta)F_{wc} + \beta F_{Si}}{(1-\beta)F^0_{wc} + \beta F^0_{Si}}, \tag{4.1}$$

where F^0_{pw}, F^0_{wc}, and F^0_{Si} are riverine input of dissolved phosphorus, carbonate, and silicate weathering at time t = 0 (modern steady-state), respectively. The coefficient β scales the relative proportion of silicate and carbonate weathering fluxes to the phosphorus riverine input (see Section 4.3.1).

Furthermore, LOSCAR was modified to adjust for ocean temperature. In the original LOSCAR model the temperature of modern surface, intermediate, and deep ocean boxes are set to 20, 10, and 2^oC, respectively (irrespective of the ocean basin). The high latitude ocean box has the same temperature as the deep ocean boxes (2^oC). The same is true for the version of the model used here. The difference is that the temperature of the ocean in the past is calculated based on the formulation presented in *Berner and Kothavala* [2001]:

$$\Delta T = \Gamma ln(R\mathrm{CO_2}) - Ws\frac{t}{570}, \tag{4.2}$$

where ΔT is the difference between the temperature at time t (millions of years before the present) and the present day temperature. Γ is a constant derived from GCM modeling that describes the dependence of global mean temperature on atmospheric CO_2 and is set to 4.0^o [*Berner and Kothavala*, 2001]. RCO_2 is the ratio between the atmospheric pCO_2 at time t and the modern value (300 ppm, preindustrial concentration). Ws (7.4^o) is factor describing

the effect the changing solar radiation has on the global temperature. Thus the combined term, $\mathrm{Ws}\frac{t}{570}$, simulates the change of the solar energy output through geologic time.

The last important modification in LOSCAR-P2 model follows the Arrhenius pattern for chemical reactions. Namely, LOSCAR-P2 assumes that metabolic rates increase with temperature [e.g. *Stanley*, 2010]. A general rule of thumb is that the reaction rate doubles with every 10^{o}C in temperature increase, often referred to as Q10:

$$Q10 = \left(\frac{R_2}{R_1}\right)^{\frac{10}{T_2 - T_1}}, \tag{4.3}$$

where R_2 and R_1 are respiration rates at temperatures T_2 and T_1, respectively. In its original form, the ratio between R_2 and R_1 represents the ratio (fR) between respiration some time in the past and the modern day respiration, for the given temperature of the deep ocean in the past ($\mathrm{T}_{deep(t)}$) compared with that of the modern deep ocean temperature ($\mathrm{T}_{deep(0)}$) [*Matsumoto*, 2007; *Kwon et al.*, 2009; *Zeebe et al.*, 2017]:

$$fR = Q10^{\frac{T_{deep(t)} - T_{deep(0)}}{10}}. \tag{4.4}$$

However, in LOSCAR-P2, organic carbon and phosphorus burial rates (rather than remineralization) are scaled directly as a function of temperature. This was achieved by multiplying the organic P and organic C burial in the model by 1/fR to account for the temperature effect. Because this approach is only approximation of the Q10 factor we call it Q_r (temperature dependent residual burial factor, see Section 4.3.2).

Phosphorus and organic C burial differs from that of carbonate as there is no explicit diagenetic sediment model associated with the burial of P and organic C. In other words,

once buried P and organic C are permanently stored and cannot be reintroduced back to the water column. Also, LOSCAR-P (and LOSCAR-P2) does not differentiate between burial of C and P in the deep sea vs. margin. However, it is important to note that the burial numbers that the model produces represent the total global burial rates (shelf + deep combined), because organic C and P burial processes are essentially modeled as one box (See Chapter 3). We acknowledge that the model could be further improved upon by modeling shallow and deep ocean C and P burial separately. Nevertheless, the results produced by LOSCAR-P (and LOSCAR-P2) are in line with carbon, phosphorus and oxygen cycle models that include both shelf and open ocean sedimentary burial [e.g. *Tsandev and Slomp*, 2009]. The model of *Tsandev and Slomp* [2009] shows that organic C burial is enhanced in both ocean regions (shallow and deep) during oxygen depletion. On the other hand, P burial rates exhibit different behavior between margins and deep ocean. In the model of *Tsandev and Slomp* [2009], which has a separate representation of the shelf and deep ocean burial, low oxygen conditions promote lower P burial rates in the deep sea (the same behavior as in LOSCAR-P/P2), while on the shelf P burial rates increase [*Tsandev and Slomp*, 2009]. However, the total net burial rate (shelf + deep) of P during the low oxygen conditions is diminished compared to the steady-state oxygen conditions, which matches predictions made by LOSCAR-P/P2. Additionally, on long-time scales ($> \sim$10 kyr), P is well mixed throughout ocean, hence the differences between shelf versus deep ocean are less critical.

Modeling procedure

As mentioned above, LOSCAR does not predict carbon fluxes between the surficial and geologic carbon reservoirs. On the other hand, GEOCARB does not include sediments or marine

carbonate chemistry. Coupling and combining these two models complements each other and eliminates the deficiencies of each model and provides a more superior tool (compared to when each model is used separately) for investigation of all major components of carbon cycling during multi-million year time periods.

Numerically, the GEOCARB module has been implemented as a function that is called from within LOSCAR (Figure 5.3). At time t = 0 (modern, pre-industrial ocean) all GEOCARB and LOSCAR fluxes match. Once LOSCAR is initiated, it uses the GEOCARB module to obtain carbon fluxes (except organic C burial) for any particular point in the past in one million-year step intervals (the time step of GEOCARB). LOSCAR then uses its own boundary conditions for a particular point in the past (e.g. 58 Ma; thus vertical mixing, temperature, $[Ca^{2+}]$ and $[Mg^{2+}]$ and other parameters all change, see Table 5.2) and is run for 1 million years to calculate a new value for organic carbon burial (which depends on the feedback between carbon, oxygen and phosphorus as well as on Q_r). The newly calculated organic carbon burial flux is then supplied to the GEOCARB module, where a Newton-Raphson method is invoked in order to calculate a new $\delta^{13}C$ value necessary to balance all the fluxes at the given time step. The calculated $\delta^{13}C$ value is then compared with the actual $\delta^{13}C$ input data of GEOCARB to see how far the LOSCAR-P2 $\delta^{13}C$ (and thus LOSCAR-P2 organic C burial rate) deviates from observations (and thus from organic C burial rate predicted by GEOCARB). Because both LOSCAR-P2 and GEOCARB use the same pCO_2-weathering feedback, once the organic carbon burial is the same in both models, so will be carbonate (F_{wc}) and silicate weathering (F_{Si}) fluxes:

$$F_{wc} = fbb(CO_2) \times f_{LA} \times f_D \times f_E \times F^0_{wc}, \tag{4.5}$$

$$F_{Si} = fb(\mathrm{CO_2}) \times f_R \times f_E \times f_D^{0.65} \times F_{Si}^0, \tag{4.6}$$

where fbb and fb are functions that account for the effects of pCO_2 on carbonate and silicate weathering rates (see *Berner* [1994]), respectively. F_{wc}^0 and F_{Si}^0 are modern carbonate and silicate weathering rates, respectively (see Table 5.1 for modern values). f's are dimensionless parameters accounting for various biogeochemical process through geologic time (see Figure 5.4 for details).

4.3 Results and Discussion

All simulations were initiated with modern steady-state fluxes and boundary conditions (Tables 5.1 & 5.2) and with the initial, modern atmospheric CO_2 concentration of 300 ppmv, as provided by GEOCARB. Many LOSCAR-P parameters have uncertainties, especially in deep time (see Section 4.2). This allows for parameter tuning (within a reasonable range) until a scenario with consistent CCD, pCO_2, and $\delta^{13}C$ is produced. In the simulations performed here, GEOCARB parameters were not modified, therefore all the adjustments were performed on the LOSCAR-P2 side of the model (Table 5.2). The future version of the model will include new GEOCARB parameters as they were recently updated in *Royer et al.* [2014]. The following is the list of simulations performed:

Simulation 1: Control run − all parameters were set according to Table 5.2, $Q_r = 1$ (burial not temperature dependent), $\beta = 1$ (Figures 5.5 and 5.6).

Simulation 2: All parameters same as above except $Q_r = 2$ (Figures 5.7 and 5.8).

Simulation 3: Preferred run − All parameters same as above except $Q_r = 4$ (Figures 5.9 and 5.10).

Simulation 4: High Q_r run − All parameters same as above except $Q_r = 8$ (Figures 5.11 and 5.12).

The results of each simulation are presented in two sets of figures. The first set shows the GEOCARB supplied temperature (same for Simulations 1−4, temperature essentially acts as a model forcing), and important carbon and phosphorus related fluxes and/or concentrations (Figures 5.5, 5.7, 5.9, and 5.11). The second set displays the model output that is validated against the various paleo-proxies for atmospheric pCO_2, $\delta^{13}C$ data, pH, and the Pacific and the Atlantic ocean CCDs (Figures 5.6, 5.8, 5.10, and 5.12).

4.3.1 Control run

The control run (Simulation 1) uses conditions outlined in Tables 5.1 and 5.2. For all simulations, we make an additional assumption regarding the continental input of phosphorus: the phosphorus riverine input is completely dependent on the silicate weathering flux ($\beta = 1.0$). This is at odds with previous modeling studies which propose that both silicate and carbonate flux contribute equally to the phosphorus weathering flux [*Flögel et al.*, 2011], and also different from the COPSE model [*Bergman et al.*, 2004], in which P weathering flux depends on silicate, and carbonate weathering and kerogen oxidation in the proportions of 2:5:5, respectively. The reason for keeping F_{pw} independent of F_{wc} in LOSCAR-P2, is to be consistent with the GEOCARB modeling framework. In GEOCARB, carbonate weathering has no effect on the atmospheric CO_2 concentration. If carbonate weathering is allowed to control phosphorus weathering in LOSCAR-P2, it would also control the organic carbon burial and hence atmospheric CO_2. Thus, for consistency between the models, β is kept at 1.0.

Carbonate and silicate weathering rates (Figure 5.5b) are primarily driven by the product of dimensionless parameters (See Eqs. (4.5) and (4.6) and Figure 5.4). The major difference between the F_{wc} and F_{Si} equation is that the f_{LA} term only appears in the equation for carbonate weathering as it describes the percentage of land area covered by carbonates. Its fluctuations are caused partly by the changes in sea level and the consequent exposure/disappearance of continental shelves and also by changes of the amount of land area underlain by carbonates. Therefore the carbonate weathering curve exhibits a prominent peak at 30 Ma, just like f_{LA} and f_D, and overall follows the shape of the product of f_{LA} and f_D. On the other hand, f_R, which is the uplift factor or the mean global relief, appears in the F_{Si} equation but not in the formulation for weathering of carbonates. The changes in mean continental relief are assumed to be recorded in the $^{87}Sr/^{86}Sr$ ratio of seawater as the higher ratio is believed to be correlated with increased silicate weatherability [*Berner*, 1994].

As P fluxes (Figure 5.5f) and $[PO_4]$ of seawater change (Figure 5.5e; due to changes in silicate weathering fluxes and oxygen concentration), so does the export production of organic carbon from the surface ocean (Figure 5.5d) and consequently the organic carbon burial flux (Figure 5.5c). Therefore the organic carbon burial curve closely mimics the organic carbon export curve. A sudden decline in organic C export at t = 23 Ma (Figure 5.5d) is due to the closure of the Tethys ocean. Before this point in time (0 to 23 Ma), the Tethys ocean boxes are no longer accounted for in the model, so the organic carbon rain from this ocean basin essentially "disappears".

The deep ocean oxygen concentration and organic carbon burial rate in Simulation 1 mirror each other (Figure 5.5c). The peak organic carbon burial rates are observed at 52 Ma (6.7×10^{12}mol yr^{-1}), when deep ocean oxygen concentration is at its lowest due to high

temperatures. This time period coincides with the highest dissolved P concentrations (Figure 5.5c) and low total P burial. Low oxygen concentrations favor enhanced organic carbon preservation while diminishing organic phosphorus burial due to increased remineralization (See Chapter 3). Higher organic P respiration in turn fuels the surface ocean with recycled organic P and enhances the primary production and results in even larger organic carbon export (positive feedback).

The positive feedback loop between carbon, oxygen and phosphorus (C-O-P feedback) has important ramifications for the various components of the carbon cycle and carbonate chemistry that are calculated by the model and become apparent when compared to the data (Figure 5.6). The discrepancies between the model results and data are most obvious during Paleocene and Eocene, when the Earth was much warmer than today and when atmospheric CO_2 concentrations were several times that of the modern (preindustrial) atmosphere [*Lowenstein and Demicco*, 2006; *Beerling and Royer*, 2011]. Starting at around 58 Ma, the Earth system experienced a 6 Myr global warming trend. Concomitant with the warming was a long-term decline of surface and deep ocean $\delta^{13}C$ [e.g *Zachos et al.*, 2008; *Hilting et al.*, 2008] while the CCD deepened [e.g *Pälike et al.*, 2012; *Leon-Rodriguez and Dickens*, 2010; *Slotnick et al.*, 2015]. Also, the gradient between the surface and deep ocean $\delta^{13}C$ remained relatively constant or slightly decreased [e.g. *Hilting et al.*, 2008; *Komar et al.*, 2013]. These features are not captured by the model in Simulation 1, in fact, they are opposite to available observations (Figure 5.6).

The main culprit for the erroneous model behavior are the high organic carbon burial rates that arise as a result of the C-O-P feedback. The model suggests declining pCO_2 during the Late Paleocene and Early Eocene, with a pCO_2 minimum at 52 Ma. Whereas in

reality, 52 Ma marks the highest temperatures (excluding hyperthermals) and quite possibly the highest atmospheric pCO_2 values in the entire Cenozoic[*Lear et al.*, 2000; *Zachos et al.*, 2001]. Various modeling studies showed that the warming (and other trends outlined above) during the LPEE might have been caused by declining net ocean-atmosphere organic carbon burial [*Kurtz et al.*, 2003; *Hilting et al.*, 2008; *Komar et al.*, 2013]. However, when also considering the long-term P cycle coupled to the C cycle via redox dependency, increased rates in organic carbon burial are predicted, driving pCO_2, surface, deep ocean and bulk sediment $\delta^{13}C$ and the CCD in the direction opposite to observations (Figure 5.6).

The problem with the modeling approach described above is that it assumes that any excess in delivery of dissolved P to the surface ocean (whether through increased continental supply or via deep ocean P recycling) and thus rising surface ocean $[PO_4]$ will not only increase export production form the surface ocean but also result in an increased amount of carbon being deposited in the deep ocean (strong carbon "pump"). Because of tight coupling between surface ocean $[PO_4]$, primary productivity, and export production, the above modeling approach will necessarily lead to high organic carbon burial rates during periods of increased warming. This poses the question: is there a mechanism that could decouple high nutrient concentration (high production) in the surface ocean from high organic carbon export? A possible mechanism is investigated in the following section.

4.3.2 Simulations 2 and 3: Preferred scenario and temperature dependent organic Carbon and Phosphorus burial

Temperature exerts two competing effects on organic carbon export and remineralization. On the one hand, higher temperatures elicit increased primary production and stronger carbon

export [*Eppley*, 1972], which is consistent with the model behavior explained above. On the other hand, high temperatures instigate a higher degradation rate of organic matter sinking through the water column, albeit resulting in a lower amount of organic matter being exported to the ocean floor [*Laws et al.*, 2000]. *Matsumoto* [2007] quantified the opposing effects that temperature has on the organic carbon pump, and therefore on pCO_2. The study showed that rising temperatures promote a boost in remineralization at a rate higher than the rise of the export production (the opposite is true for declining temperatures), essentially decoupling export production rates from the organic carbon pump. Hence, it is possible to increase the nutrient supply to surface waters while organic carbon burial in the deep ocean simultaneously decreases.

In LOSCAR-P2, the above behavior is simulated by inversely scaling organic carbon and phosphorus burial with temperature in an attempt to simulate the Q10 effect on degradation of sinking organic matter (See Eq. (4.3)). Note that this is only an approximation of the Q10 factor, as our scaling factor (Q_r) is not applied to the remineralization rate of organic matter but rather directly to the organic carbon and phosphorus burial rates, and thus is different from the actual Q10 factor. In other words, the Q_r value of 2 for example, does not equate to a doubling of respiration per 10^oC increase in temperature. In Simulation 2 (Figures 5.7, 5.8), Q_r is set to 2, which translates to halving of C and P burial rates per a 10 degree temperature increase. Note that during the LPEE the inclusion of temperature dependence amplifies the organic carbon export (Figure 5.7d). Despite higher surface ocean $[PO_4]$ (Figure 5.7e), the increase in overall organic carbon burial is dampened in Simulation 2 (Figure 5.7c), illustrating the effect of temperature on remineralization rates. Due to lower organic carbon burial, atmospheric pCO_2 is now slightly more elevated (Figure 5.8a), which consequently

results in accelerated carbonate and silicate weathering fluxes (Figure 5.7b) compared to Simulation 1. The effect of lower organic carbon burial combined with the increased silicate weathering (and pCO_2) and higher carbonate input gives model trends more consistent with the data. Organic carbon is isotopically light, thus burying less org. C causes a slight drop in $\delta^{13}C$ of the bulk sediments as well as that of the surface ocean (Figures 5.8a and Figures 5.8b, respectively). Higher carbonate weathering rates, and thus larger inorganic carbon export, produce the CCD deepening between 58 and 52 Ma, which is more consistent with observations (Figure 5.8e, Figure 5.8f).

Next, Q_r was doubled (= 4) in Simulation 3, which enhances model trends compared to Simulation 2, producing results increasingly consistent with observations during the LPEE (Figure 5.10). Nonetheless, while the general trends are consistent, absolute changes in magnitude are not. The observed mean bulk carbonate $\delta^{13}C$ decrease during this time period is about 2.0‰, whereas the model captures approximately only half of the observed negative excursion (∼1.00‰). Similar behavior is observed during the rest of the Cenozoic; even though the shape of the $\delta^{13}C$ curve follows the data trend, the relative changes in modeled bulk $\delta^{13}C$ are dampened (Figure 5.10b). The absolute value of $\delta^{13}C$ is also underestimated, especially during the late Paleocene and between 50 and 10 million years ago. Keeping everything else equal, there are at least two possible reasons for the model-data discrepancy. First, the $\delta^{13}C$ value of the riverine input is kept constant throughout the run. Changes in type of the material being preferentially weathered, and/or changes in proportion of the amount of organic carbon being weathered relative to carbonate carbon, at different climates and across different time intervals, could very well cause variations in the carbon isotopic value of the riverine flux. If the carbon isotopic value of carbonates being weathered was higher (or

the ratio between carbonate to organic carbon isotopic value was higher and/or the isotopic value of organic material being weathered was heavier) at 58 Ma and decreased throughout the LPEE, it would ameliorate the δ^{13}C disagreement. Higher δ^{13}C of the carbonates washed in the ocean and/or a higher δ^{13}C of kerogens could also close the model-data gap between 50 and 10 Ma. Second, it could be possible that the absolute organic carbon burial rates predicted by the model are lower than the actual ones. Higher organic C burial rates would lead to a more enriched carbon isotopic value, however, this would not fix the relative changes in δ^{13}C that are underestimated in the model. On the other hand, the relative variations in δ^{13}C could be rectified by applying a stronger Q_r (= 8; see Figures 5.11, 5.12) but would result in a larger discrepancy in the absolute value of δ^{13}C.

4.3.3 The CCD trends

The records of carbonate accumulation rates and carbonate content of the sediments show the variable nature of the calcite compensation depth across the Cenozoic [*Pälike et al.*, 2012; *Slotnick et al.*, 2015]. For an easier model-data comparison we classify these changes in two different categories: (1) the first order, general CCD trend across the entire studied interval, and (2) the second order, multi-million year trends. Important to note is that prominent short-term CCD variations are also observed in the sediment record across the studied period, nevertheless the nature of the model and its resolution (1 My), precludes investigation of the transient CCD features.

The first order CCD trend

The general, first order trend, indicates global CCD deepening of at least 1 km from 62 Ma, when the CCD resided at ∼3.5 km, to ∼4.5 km at present [*van Andel, T. H.*, 1975; *Pälike et al.*, 2012; *Slotnick et al.*, 2015] (Figure 5.1d). Our coupled modeling approach captures the first order, deepening trend of the CCD across the Cenozoic in all simulations (Figures 5.6, 5.8, 5.10, 5.12). The long-term CCD trend is consistent with the data despite the model predicted decline in both silicate and carbonate weathering fluxes across the same time interval. According to a conventional view of the carbon cycle, decreasing weathering rates should diminish the alkalinity supply and lower the carbonate saturation state of the ocean, causing the CCD to shoal [e.g. *Sluijs et al.*, 2013, *and references therein*]. However, the CCD trends can be decoupled from weathering fluxes, and thus alkalinity delivery. Such decoupling could arise due to sea transgression/regression as it would affect the relative partitioning of carbonate burial between the shelf and deep ocean [*Pälike et al.*, 2012; *Sluijs et al.*, 2013]. But there could be additional factors, such as changes in bathymetry, weatherability, variations in the rain ratio as well as changes in ocean mixing rates.

As mentioned above, the original LOSCAR shelf-deep partitioning (fsh) value for the paleo model set-up was obtained by model tuning, i.e., shelf carbonate deposition relative to deep ocean carbonate deposition is several times higher than the modern partitioning (Table 5.2), which is justified by much higher sea level during the Late Paleocene [e.g. *Miller et al.*, 2005; *Kominz et al.*, 2008]. Simulations 1-4 all assume a variable fsh, where its value is linearly interpolated between high carbonate deposition on the shelves in the Late Paleocene (fsh = 4.5), to high deep ocean carbonate deposition in the modern ocean (fsh = 1). To show the importance and the effect of the shelf-basin carbonate deposition on the CCD, the

preferred simulation was run keeping fsh constant at the modern value (Figure 5.13). This experiment shows that the change in shelf-basin carbonate deposition could be responsible for the overall CCD deepening across the Cenozoic in our simulations but is likely not the main mechanism for the permanent CCD offset that happened at the E/O boundary (See Section 4.3.3 for possible mechanism). More importantly, it demonstrates that the global CCD deepening over the Cenozoic does not necessarily require an increase in global chemical erosion rates, a mechanism often invoked to reconcile the observed trends across this time period [*Raymo et al.*, 1988; *Raymo and Ruddiman*, 1992; *Misra and Froelich*, 2012; *Pälike et al.*, 2012]. Our result is also more consistent with the current understanding of the long-term carbon cycling and feedbacks between weathering and atmospheric pCO_2. Declining atmospheric CO_2 concentration [*Beerling and Royer*, 2011], combined with relatively constant or decreasing CO_2 degassing rates over the same time period [*Berner et al.*, 1983; *Müller et al.*, 2008; *Van Der Meer et al.*, 2014] require a slow-down in weathering rates because of the pCO_2-silicate weathering feedback that stabilizes atmospheric CO_2 on geological time scales [e.g. *Walker and Kasting*, 1981; *Berner et al.*, 1983; *Berner and Caldeira*, 1997].

The model predicted changes in silicate and carbonate weathering fluxes are also consistent with phosphorus accumulation rates. *Delaney and Filippelli* [1994] and *Filippelli and Delaney* [1994] found phosphorus accumulation rates to be declining between 50 and 20 Ma (which is also consistent with the total P burial trend in our model; see Figure 5.9f) and then rising again from 10 Ma to present with a substantial peak around 5 Ma (rising P burial between 10 and 0 Ma also present in our preferred simulation, only the increase is not as pronounced). However, *Delaney and Filippelli* [1994] interpreted the long-term Cenozoic decline in phosphorus accumulation rate as a contradiction, because the trend was in conflict with

the Himalayan uplift theory [e.g. *Raymo and Ruddiman*, 1992], which they believed caused an increase in chemical erosion across the Cenozoic. If the weathering rates did not increase during this time interval, for which there is evidence [e.g. *Willenbring and von Blanckenburg*, 2010], then there is no inconsistency between P accumulation rates and the Cenozoic weathering trends, which further validates our modeling results.

The overall changes in P weathering and silicate weathering fluxes presented here are also similar to the fluxes calculated in a model of long-term geochemical cycling called MAGic [*Arvidson et al.*, 2006; *Guidry et al.*, 2007]. MAGic describes the influence of P, and other elements such as Ca, Mg, C and S, on biogeochemical cycles and climate over multi-million year time scales. Because of the different magnitudes of modern date (0 Ma) silicate and phosphorus weathering fluxes between LOSCAR-P and MAGic, the similarities and differences are discussed in terms of relative variations and trends rather than discussing absolute changes. Much like LOSCAR-P, MAGic predicts an increase in P weathering flux between 60 and 50 Ma (the resolution of MAGic is 10 my), which closely follows the shape of the silicate weathering curve [*Guidry et al.*, 2007] (Figure 5.14). The P weathering flux in MAGic then gradually decreases from 50 Ma until present, while always staying above the modern value during the entire Cenozoic. Silicate and phosphorus weathering trends start to diverge in MAGic at 20 Ma (until 0 Ma), when the decline in silicate weathering rates slows down and remains lower than the present day silicate flux, while the P flux continues to decrease. Silicate weathering trends in LOSCAR-P at 10 and 20 Ma are also lower than the present day fluxes and thus in good agreement with the trends predicted by MAGic. The major difference between the two models occurs at 20 and 10 Ma, when LOSCAR-P predicts P weathering rates to be lower than the modern day value, which is due to the phosphorus-silicate dependence assumed in

LOSCAR-P.

The second order CCD trends

The most notable second order, multi-million year CCD patterns across the Cenozoic are the CCD deepening between 58 and 52 Ma, interrupted by a sudden shoaling from 52 to around 50 Ma [See Figure 5.1d; *Slotnick et al.*, 2015]. From 50 Ma until 10 Ma the Pacific CCD exhibits a deepening trend punctuated by several short-lived shoaling events. The most prominent, sustained deepening took place at the Eocene/Oligocene boundary (∼34 Ma) when the Pacific CCD deepened by more than 1 km in less than 300 ky [*Coxall et al.*, 2005]. Starting at about 10 Ma the Pacific CCD begins to shoal until it finally reaches the modern depth of about 4.7 km. The Atlantic CCD second order trends begin to differ from the ones displayed in the Pacific basin over the past 10-15 Ma, as it appears that the Atlantic CCD deepened by ∼1 km over this time interval (Figure 5.1d).

Our preferred scenario adequately matches most of the second order trends described above. The majority of the second order CCD variations are a result of alkalinity fluctuations, which arise due to variable carbonate weathering fluxes, as well as due to the variable alkalinity export from the surface ocean (inorganic carbon rain scales with organic carbon rain because of the rain ratio) along with changing P burial fluxes (see Chapter 3 for details on P and alkalinity relationship).

The observed CCD deepening trend (along with pCO_2 increase and negative $\delta^{13}C$ excursion) between 58 and 52 Ma is difficult to reproduce without an increase in riverine carbonate delivery. In order to produce increasing carbonate weathering fluxes during this time period, elevated atmospheric pCO_2 is necessary, which is also consistent with temperature proxies.

However, in order for CO_2 to accumulate in the atmosphere sufficiently over this time span to cause an adequate increase in carbonate weathering (and indirectly via P weathering an increase in organic carbon export), a decrease in organic carbon burial is required. The issue here is that the same mechanism responsible for the rising pCO_2 and thus accelerated weathering fluxes will also drive up the surface ocean phosphate concentration, which will ultimately increase organic carbon burial (and lower pCO_2), and result in the CCD, and pCO_2 and $\delta^{13}C$ trends, inconsistent with observations. In order to reconcile the trends across the LPEE, a temperature dependent burial must be invoked (See sections 4.3.1 & 4.3.2).

The model fails to predict CCD observations between 45 and 50 Ma, when the Pacific CCD was at its shallowest in the past 50 Mys (Figure 5.10e). The failure stems from the fact that the rapid shoaling at ∼50 Ma is not captured as it happens over time scales that are not well resolved by the model (the model resolution is 1 My). For the same or similar reasons, the Pacific CCD shoaling of about 600 m during the mid-Miocene (∼19 to 16 Ma) is also unresolved by the model. The sudden CCD deepening at 24 Ma is a model artifact, as this point in time marks the closing of the Tethys basin in the model (after 24 Ma the Tethys ocean is not present in the model; see Section 4.3.1). The Tethys basin closure results in a drop in total organic (and inorganic) carbon export, which in turn results in a lower inorganic carbon rain per area of sediments and the consequent global CCD deepening.

The precipitous CCD deepening at the E/O transition, as stated above, cannot be resolved by the model due to the resolution constraints. However, a long-term, background trends might provide an insight to as to why the Earth system crossed a threshold at the E/O boundary after which the CCD has never recovered to the shallow Eocene depths. Our model predicts the lowest organic carbon burial in the Entire Cenozoic during the Late Eocene-Early

Oligocene, which remained relatively stable despite a noticeable increase in deep ocean oxygen concentration between 40 and 30 Ma (Figure 5.9c). Cooling temperatures across this time period according to the Q10 theory should increase organic burial but rapidly increasing deep ocean O_2 concentration of the cooling ocean cancels the Q10 effect. Simultaneously, the model predicts a rapidly dropping export production (Figure 5.9d), due to declining surface ocean PO_4 concentration (Figure 5.9e), while at the same time carbonate weathering rates are predicted to increase considerably (Figure 5.9b) as a result of the increased carbonate land area (Figure 5.4). Because of the cooling temperatures and decreasing respiration of organic matter the CO_2 content in the intermediate water declines. All the factors combined lead to an increase in the ocean alkalinity and a rapid rise of the $[CO_3^{2-}]$, especially that of the intermediate water, pushing the CCD deeper. Interestingly, the $[CO_3^{2-}]$ of the intermediate waters becomes higher than the deep ocean concentration right around the time of the E/O boundary ($\sim$34 Ma), after which it remains higher for the rest of the Cenozoic (Figure 5.15).

As mentioned above, another second order observed CCD trend, is the shoaling of the CCD in the Pacific basin starting at $\sim$10 Ma, while at the same time the Atlantic CCD seems to deepen (Figures 5.10e & 5.10f). There is evidence around the same time for a step in the onset of North Atlantic Deep Water formation [*Woodruff and Savin*, 1989; *Wright et al.*, 1991], prior to which deep water was primarily formed in the Southern Ocean. We modeled this reorganization in deep water formation by assuming a linear switch from predominantly SO (at 10 Ma) to entirely NADW (at present) formation (see Table 5.2). If such a circulation pattern is invoked, then the model is successful in reproducing the observed CCD trends but not the magnitude of the CCD change.

To understand the effect of changing circulation on the CCD, we describe here the dif-

ferences between SO and NADW circulation patterns. Water masses entering the Pacific and the Atlantic ocean during the SO circulation mode are relatively equally distributed, resulting in a similar chemistry in both basins as the ages of water masses do not significantly differ. The differences between the Atlantic and the Pacific CCD mainly arise due to different bathymetries. The Atlantic ocean shelf area during the Miocene is larger than that of the Pacific. The larger shallow areas of the Atlantic bury more carbonate delivered by rivers, resulting in a smaller fraction of carbonate being exported to the open ocean, compared to the Pacific. In turn, the carbonate ion concentration in the deep Atlantic is lower than in the deep Pacific (keeping everything else equal), and accordingly the Atlantic CCD is shallower.

On the other hand, during a dominant NADW regime, the water traverses large distances before first reaching the Indian, and finally the Pacific ocean. Along the flow path, the water masses become progressively more corrosive due to remineralization of sinking organic matter from the surface ocean. The respiration of the organic matter produces CO_2 and therefore steadily increases the dissolved inorganic content of the water mass along its path. The increased CO_2 reacts with CO_3^{2-}, thus making the carbonate ion content of the Pacific considerably lower than that of the Atlantic ocean, which consequently results in a shallower Pacific CCD. Hence, going forward in time (from 10 Ma to present) as the contribution of deep water formation is gradually changed from predominantly SO to entirely NADW (see Table 5.2), the Pacific CCD shoals while the Atlantic CCD deepens, producing trends consistent with observations (Figures 5.10e & 5.10f).

4.4 Conclusions and Outlook

Over the past ∼60 My, the Earth system has experienced long-term and rapid variations in climate and ocean chemistry [e.g. *Zachos et al.*, 2001; *Lyle et al.*, 2008]. The two most distinct long-term trends observed in the Cenozoic are Late Paleocene Early Eocene, a 6-My-long interval of global warming [*Zachos et al.*, 2001; *Bijl et al.*, 2009; *Westerhold et al.*, 2011], accompanied by global CCD deepening of at least 500 m [*Slotnick et al.*, 2015]. Second, the LPEE is followed by a steady decline in global temperatures and atmospheric pCO_2 since 50 Ma, which eventually resulted in large ice sheets forming at high latitudes, which were non existent prior to the onset of the cooling [*Zachos et al.*, 2001]. Concurrent with the cooling was the global CCD deepening of about 1 km [*Pälike et al.*, 2012]. The climate and ocean chemistry evolution during the Cenozoic has been the focus of numerous studies [*Berner et al.*, 1983; *Berner and Kothavala*, 2001; *Zachos et al.*, 2001; *Wallmann*, 2001; *Arvidson et al.*, 2006; *Pälike et al.*, 2012; *Li and Elderfield*, 2013; *Caves et al.*, 2016]. However, to the best of our knowledge, continuous simulation of the CCD, which is a crucial part for understanding carbon cycle shifts during the Cenozoic, has so far been neglected.

Our results show that complete ocean carbonate chemistry, prognostic organic carbon and phosphorus burial rates, and $\delta^{13}C$ at various depths combined with the ability to predict the CCD is vital for constraining carbon cycle and climate dynamics over multi-million-year time scales. We suggest that metabolic effects caused by elevated temperatures of the Paleogene must be accounted for when the long-term phosphorus cycle is considered. Otherwise, the predicted organic carbon burial is inconsistent with records of $\delta^{13}C$, temperature, pCO_2, and carbonate accumulation rates. Another fundamental model result is that the observed long-term deepening of the CCD across the Cenozoic does not require an increase in silicate

and carbonate weathering fluxes. The results suggest that the CCD trends were decoupled from the silicate and carbonate weathering fluxes during the Cenozoic. We propose that the decoupling developed partially due to the decreasing proportion of carbonate buried in the open ocean relative to the shelf carbonate deposition, as the sea level regressed with global cooling and the formation of continental ice sheets. Additionally, high PO_4 and consequently high remineralization rates of the Paleocene-Eocene resulted in low intermediate $[CO_3^{2-}]$ due to high CO_2 production rates from respiration of organic matter. As the Earth cooled and PO_4 concentrations declined, the carbonate ion content of intermediate waters rose, crossing a critical threshold that increased the preservation of calcium carbonate in the sediment and consequently enabled a sudden and permanent CCD deepening that occurred during the Eocene/Oligocene.

Several model deficiencies remain when simulating shorter time scale features. The high Miocene bulk carbonate $\delta^{13}C$ values are underestimated by our model. This discrepancy stems from the fact that the GEOCARB predicted temperatures for the Miocene are much lower than the observed values. Higher temperatures in the model would lead to lower oxygen concentration of the deep sea, instigating preservation of organic carbon and higher organic carbon burial rates. Consequently, as a larger amount of ^{13}C depleted organic carbon is buried, it would lead to higher $\delta^{13}C$ of the ocean.

Another important shortcoming of the coupled GEOCARB-LOSCAR model is that GEOCARB land parameters, which drive the continental weathering fluxes of organic and inorganic carbon, have a very low resolution ($>$ 10 My). Therefore, any changes related to those continental fluxes occurring on sub-10 My time scales are not captured by the model. For example, as the land parameters exert control on carbonate and silicate weathering rates,

which in turn affect the CCD and carbon isotopes, the second order CCD and δ^{13}C variations are not appropriately resolved. Future modeling studies would greatly benefit from more detailed description of land parameters across the Cenozoic. As mentioned above, the sea level fluctuations and the associated covering and exposure of the continental shelves as well as the fraction of land area covered by carbonates is described by the GEOCARB's f_{LA} parameter, which governs the carbonate weathering rates. On the other hand, the relative proportion of carbonate being buried in the deep ocean versus shelves (the fsh parameter) is linearly interpolated between only two tuned values. Essentially, there is a disconnect between the sea level changes described by the f_{LA} parameter and the partitioning of carbonates in deep versus shelf ocean. The modeling framework could be approved upon by using GEOCARB's f_{LA} factor to describe the changes in LOSCAR's fsh parameter. With this approach, partitioning of carbonates between shelf and deep ocean would be represented more realistically and would be consistent with the sea level transgression/regression trends across the Cenozoic. If incorporated, the sea level changes could potentially ameliorate model-data CCD discrepancies outlined in Section 4.3.3 (e.g. the rapid shoaling at ∼52 Ma or the magnitude of the CCD change during the oast 10 my due to change in the circulation mode of the ocean). But it is important to note that there are other processes affecting the CCD that are not considered, such as ocean vertical mixing rates and the rain ratio of carbon from the surface ocean. However, the temporal evolution of these processes in the time domain considered here is very limited or non existent and therefore an attempt to tune these parameters in order obtain more consistent CCD variations would be purely speculative.

Because the long-term P and organic C cycles are modeled as one box (see Section 4.2.2), the model does not explicitly account for the effect of the continental shelves, which leaves

room for future model improvements. For example, today, up to 70-90% of organic matter and reactive P burial takes place on the continental margins and alluvial, lagoonal, and littoral environments [e.g. *Berner*, 1982; *Howarth et al.*, 1995]. The shelf oceanic reservoirs therefore play an important role in nutrient recycling and global marine production [e.g. *Mackenzie et al.*, 1993], which is not captured by the current modeling framework. The model in its current state, for example, precludes the reconstruction of episodic intervals of phosphorite formation, such as those observed during the Eocene and the Miocene [e.g. *Cook and McElhinny*, 1979; *Riggs*, 1984]. These events might hold important clues regarding the climatic conditions associated with the time intervals during which abundant phosphorite deposits were formed. For instance, the phosphorites might indicate sea level increase and possibly accelerated inputs of P from the continents. Once a more realistic representation of organic matter burial in the neritic environments is included in the model, it will provide an insight into the importance of the role of continental shelves in multi-million year shifts in climate and variations in biological primary production.

Despite the limitations, the model used in this study adequately captures the long-term CCD, pCO_2 and $\delta^{13}C$ trends. Certainly, at this stage, there are still a few unresolved data-model discrepancies that prohibit a fully consistent reconstruction of climate and ocean chemistry across the Cenozoic. This does not come as a surprise, however, as this is the first attempt at reconciling both the CCD and other carbon cycle trends by considering a large number of biogeochemical components and feedbacks of the ocean-atmosphere system.

CHAPTER 5
SUMMARY OF FINDINGS AND GENERAL DISSERTATION CONCLUSIONS

5.1 Introduction

The purpose of this chapter is to summarize the principal findings of the individual research projects comprising this dissertation. The underlying common subject of the three studies presented here is numerical carbon cycle and paleo-climate modeling on a variety of time scales and across different time intervals. In general, the research presented in Chapters 2 and 3 investigates the responses of the Earth system to abrupt CO_2 emissions into the ocean-atmosphere system during the end-Permian mass extinction event and during the Paleocene Eocene Thermal Maximum. More specifically, the goal of Chapter 2 is to check the fidelity of calcium isotopes as a proxy for ocean acidification during past carbon cycle perturbation events. The PETM modeling presented in Chapter 3 explores the connection between the organic and inorganic carbon cycles and therefore biogeochemical feedbacks, possibly responsible for termination of hyperthermal events. We conclude with Chapter 4, where we utilize the biogeochemical feedbacks developed in Chapter 3 but apply them on a much longer time scale to examine their role in controlling the long-term evolution of climate and carbon cycling across the entire Cenozoic. Collectively, the results contribute to an improved understanding of ocean carbonate chemistry and climate responses to intense carbon cycle emissions, which aids in improving the forecast for the ongoing and future anthropogenic climate change.

5.2 Summary of the Individual Project Results

5.2.1 Chapter 2 Findings

The work presented in Chapter 2 points out the deficiencies of calcium-only models and stresses the importance and the need for a fully coupled calcium-carbon cycle model when investigating changes in carbon and calcium cycling during carbon cycle perturbation events, such as the end-Permian. Chapter 2 employs the LOSCAR model, expanded to track calcium and calcium isotopes in both seawater and sediments. Our modeling approach successfully reproduces all the end-Permian trends in δ^{13}C and δ^{44}Ca. The main conclusions of Chapter 2 are that the end-Permian trends observed in the sediment record are a result of Siberian Trap volcanism and emission of $\sim$12,000 Pg C and a severe reduction in biological production. More importantly, the changes in δ^{44}Ca of seawater are not a direct result of ocean acidification but more likely due to variable calcium isotope fractionation, which depends on $[CO_3^{2-}]$ during periods of enhanced inorganic carbonate precipitation (such as in the aftermath of a mass extinction event).

5.2.2 Chapter 3 Findings

The research presented in Chapter 3 centers around a short-term (geologically speaking) carbon cycle perturbation event, however, the focus is on a different time interval. That is, we investigate the Paleocene Eocene Thermal Maximum and more specifically, we explore mechanisms responsible for the rapid restoration of the ocean-atmosphere system back to pre-perturbation levels. The fast termination of the PETM has been suggested to result from increased organic carbon burial rates [*Bowen and Zachos*, 2010] but prior to the present

study, a predictive mechanism responsible for the elevated organic carbon burial rates after significant CO_2 emission events has not been explored. By expanding the LOSCAR model to include a long-term phosphorus cycle (in addition to the existing short-term cycle), we show that a feedback between carbon, oxygen and phosphorus (C-O-P feedback) may accelerate organic carbon sequestration during major carbon cycle perturbations, such as the PETM. The accelerated recovery of the Earth system is attributed to an increase in nutrient delivery to the surface ocean and a consequent enhancement in primary production, which ultimately increases the burial of organic carbon and a drawdown of atmospheric CO_2.

5.2.3 Chapter 4 Findings

In Chapter 4 the focus switches from rapid global warming events to more gradual, long-term shifts in climate and carbon cycling during the Cenozoic era. For that purpose, we use the expanded LOSCAR version of Chapter 3 (including long-term P cycle), and couple it to the modified version of the GEOCARB III model. This modeling framework allows multi-million year simulation of ocean carbonate chemistry, reconstruction of the CCD, and prediction of carbonate and silicate weathering fluxes, as well as predictive organic carbon export and burial. Such modeling architecture imposes additional constraints on the carbon cycle and weathering fluxes, and enhances our understanding of the puzzling carbon cycle trends during the past 50 Ma. The major conclusion of our modeling effort is that the carbonate and silicate weathering rates were decoupled from the global CCD trends over most of the Cenozoic. We propose that the decoupling occurred as a result of decreasing sea level and changes in shelf vs. deep ocean carbonate burial, as well as due to long-term cooling and a decrease in remineralization of organic matter in intermediate waters. Our results imply that the pCO_2-

weathering feedback was the main regulator controlling atmospheric pCO_2 and therefore, silicate and carbonate weathering rates likely declined across the Cenozoic as atmospheric pCO_2 dropped.

5.3 Dissertation Synthesis and General Conclusions

Since the beginning of the Industrial Revolution, humans have been emitting large and growing amounts of CO_2 to the atmosphere, primarily through fossil fuel burning and cement production. The direct result of human activities is a steady increase in atmospheric CO_2 concentration of over 40% during the last two centuries (280 ppmv to >400 ppmv). As a greenhouse gas, rising atmospheric CO_2 concentrations greatly affect climate and global temperatures by changing Earth's radiative forcing. A vast amount of CO_2 entering the atmosphere is eventually absorbed by the oceans, lowering seawater pH and decreasing the calcium carbonate saturation state. A considerable effort over past three decades has been made to predict the consequences of rising CO_2, both on climate and ocean chemistry, as well as marine life. One way to gain insight into the possible future ramifications and impacts on ocean chemistry is to examine the geological past, as greenhouse conditions persisted for larger portions of the Phanerozoic [*Berner and Kothavala*, 2001; *Arvidson et al.*, 2006].

Sedimentary archives and traditional proxies, as well as the advent of various new geochemical proxies has improved our ability to reconstruct Earth's past climate and carbon cycle dynamics [*Zachos et al.*, 2001]. Particularly invaluable are stable carbon and oxygen isotopes, which reveal the rates and scales of the past climate change [*Zachos et al.*, 2001]. When used in combination with numerical models, such as the biogeochemical models employed in Chapters 2-4 of this dissertation, $\delta^{13}C$ and $\delta^{18}O$ become a powerful asset for

analyzing and quantifying past environmental changes. Not only do models allow interpretation of climate conditions at a certain point in the past, but also provide a predictive ability regarding the dynamics of the carbon cycle and climate, as they describe the resiliency of the Earth system to carbon cycle perturbations. Therefore, the ability to reconstruct and reconcile geological data during massive carbon emission events in the past using carbon cycle models, may provide insight into future changes in climate and ocean carbonate chemistry. One such event is the Paleocene Eocene Thermal Maximum, which is presumably the closest analog for the present and future anthropogenic CO_2 emissions. During the PETM around 5,000 Pg of carbon was released to the ocean-atmosphere system, which is equivalent to the entire fossil fuel reserves that could potentially be exploited over the next 500 years. This amount of carbon significantly alters the carbonate chemistry of the ocean and may have deleterious effects on marine calcifying organisms. In Chapter 3, we primarily examine the biogeochemical feedbacks that take place after the cessation of the CO_2 emissions and pathways in which the Earth system restores back to the pre-perturbation state. It appears that the feedback between carbon, oxygen, and phosphorus helps in restoration of climate and ocean chemistry at a pace faster than expected from silicate weathering alone during prominent carbon cycle perturbation events. Worth mentioning is that even if a similar mechanism operated today, the time scale necessary for the feedback to become significant is too long (tens of thousands of years) to alleviate the short-term consequence of rapidly rising CO_2, such as ocean acidification on time scales of decades to centuries.

Carbon cycle models can also be used to test the fidelity of some geochemical proxies. For example, a coupled carbon-calcium cycle model as used in Chapter 2, evaluates the assertion of previous studies [*Payne et al.*, 2010; *Hinojosa et al.*, 2012], which propose that abrupt

changes in calcium isotopes of seawater might reflect the oceans paleo-acidity, particularly during the end-Permian. Our modeling results, however, do not agree with their claims. The results of *Payne et al.* [2010] were erroneous because they only considered the calcium cycle without accounting for the effects of carbonate chemistry in a coupled carbon-calcium cycle. We suggest that future studies take into account our results presented in Chapter 2 to improve the interpretation of calcium isotope changes during past climate-carbon cycle events. Finally, follow-up projects to this thesis should include the application of the C-O-P feedback (see Chapter 3) to the end-Permian, as well as other events in the past such as the oceanic anoxic events of the Cretaceous era.

5.4 Figure Captions:

Figure 5.1. Compilation of Cenozoic temperature, $\delta^{13}C$, pCO_2, and CCD history for different ocean basins. (a) Global deep ocean temperature [*Zachos et al.*, 2008], (b) $\delta^{13}C$ compilation at different depths (Benthic: *Zachos et al.* [2008], Surface: *Hilting et al.* [2008]), Bulk: *Kurtz et al.* [2003]), (b) atmospheric CO_2 [*Beerling and Royer*, 2011; *Zhang et al.*, 2013], (d) Pacific, Atlantic and and Indian ocean CCD as estimated by *van Andel, T. H.* [1975] (blue), *Pälike et al.* [2012] (red) and *Slotnick et al.* [2015] (green, hypethermals data excluded).

Figure 5.2. Cenozoic Mg and Ca concentrations. a) Magnesium concentration. The lines are calculated by cubic interpolation of the Cenozoic Ca and Mg concentrations data compiled by [*Tyrrell and Zeebe*, 2004] b) The Mg/Ca ratio calculated from the data in panel "a".

Figure 5.3. LOSCAR-P2 − GEOCARB coupling schema. See section 4.2.2 for details.

Figure 5.4. Dimensionless GEOCARB parameters that account for various biological and geological factors across the Cenozoic (resolution = 10 Myr). All parameters are expressed relative to modern. f_{LA}: describes the changes in the land area of carbonates available for weathering, f_D: describes changes in river runoff due to variations in paleogeography, f_E: soil biological activity of land plants and their influence on weathering rates, f_R: represents the mean global relief relative to present.

Figure 5.5. Simulation 1 (Control run: See section 4.3 for more details). a) GEOCARB predicted deep ocean temperature based on Eq. (4.2) assuming that the high latitude (deep ocean) warming is twice as large compared to global average. b) LOSCAR-P2 evolution of carbonate, silicate and phosphorus weathering fluxes. c) LOSCAR-P2 predicted organic carbon burial rate (solid line) and mean deep ocean oxygen concentration (dashed line). d)

Total global organic carbon export form the surface ocean. e) Phosphate concentration in all LOSCAR-P2 boxes. "L" stands for low latitude surface ocean, "I" is intermediate, "D" is deep ocean, and "H" is the high latitude ocean. A,I,P and T correspond to Atlantic, Indian, Pacific, and Tethys ocean, respectively. f) Phosphorus burial fluxes.

Figure 5.6. Data − model comparison of various model results for Simulation 1. a) Atmospheric pCO_2. The continuous red line is the model result and the symbols represent the data (See Figure 5.1 for symbols description). b) Bulk carbonate $\delta^{13}C$ data (open circles) versus model predicted bulk carbonate $\delta^{13}C$ (green line). c) Model predicted pH versus pH reconstructed from paleo-proxies [*Pearson et al.*, 2009; *Seki et al.*, 2010; *Foster et al.*, 2012; *Raitzsch and Hönisch*, 2013; *Stap et al.*, 2016] d) Evolution of $\delta^{13}C$ in all ocean boxes. e) Model predicted evolution of the Pacific CCD against the Pacific CCD data ([*Pälike et al.*, 2012]). f) Model predicted evolution of the Atlantic CCD against the Atlantic CCD data [*van Andel, T. H.*, 1975].

Figure 5.7. Simulation 2 ($Q_r = 2$; See section 4.3 for more details). a) GEOCARB predicted deep ocean temperature based on Eq. (4.2) assuming that the high latitude (deep ocean) warming is twice as large compared to global average. b) LOSCAR-P2 evolution of carbonate, silicate and phosphorus weathering fluxes. c) LOSCAR-P2 predicted organic carbon burial rate (solid line) and mean deep ocean oxygen concentration (dashed line). d) Total global organic carbon export form the surface ocean. e) Phosphate concentration in all LOSCAR-P2 boxes. "L" stands for low latitude surface ocean, "I" is intermediate, "D" is deep ocean, and "H" is the high latitude ocean. A,I,P and T correspond to Atlantic, Indian, Pacific, and Tethys ocean, respectively. f) Phosphorus burial fluxes.

Figure 5.8. Data − model comparison of various model results for Simulation 2. For

individual panel description, refer to Figure 5.6.

Figure 5.9. Simulation 3 ($Q_r = 4$, preferred scenario; See section 4.3 for more details). a) GEOCARB predicted deep ocean temperature based on Eq. (4.2) assuming that the high latitude (deep ocean) warming is twice as large compared to global average. b) LOSCAR-P2 evolution of carbonate, silicate and phosphorus weathering fluxes. c) LOSCAR-P2 predicted organic carbon burial rate (solid line) and mean deep ocean oxygen concentration (dashed line). d) Total global organic carbon export form the surface ocean. e) Phosphate concentration in all LOSCAR-P2 boxes. "L" stands for low latitude surface ocean, "I" is intermediate, "D" is deep ocean, and "H" is the high latitude ocean. A,I,P and T correspond to Atlantic, Indian, Pacific, and Tethys ocean, respectively. f) Phosphorus burial fluxes.

Figure 5.10. Data − model comparison of various model results for Simulation 3. For individual panel description, refer to Figure 5.6.

Figure 5.11. Simulation 4 ($Q_r = 8$, extreme scenario; See section 4.3. For individual panel description, refer to Figure 5.5.

Figure 5.12. Data − model comparison of various model results for Simulation 4. For individual panel description, refer to Figure 5.6.

Figure 5.13. The CCD sensitivity to shelf-basin carbonate deposition. The solid line shows the Pacific CCD from Simulation 3. The dashed line is the Pacific CCD evolution using the same forcing as in Simulation 3 except the fsh = 1 throughout the entire run.

Figure 5.14. MAGic phosphorus (P) and silicate (Si) weathering fluxes [*Guidry et al.*, 2007].

Figure 5.15. The evolution of $[CO_3^{2-}]$ across the Cenozoic for the preferred scenario (Simulation 3).

5.5 Figures:

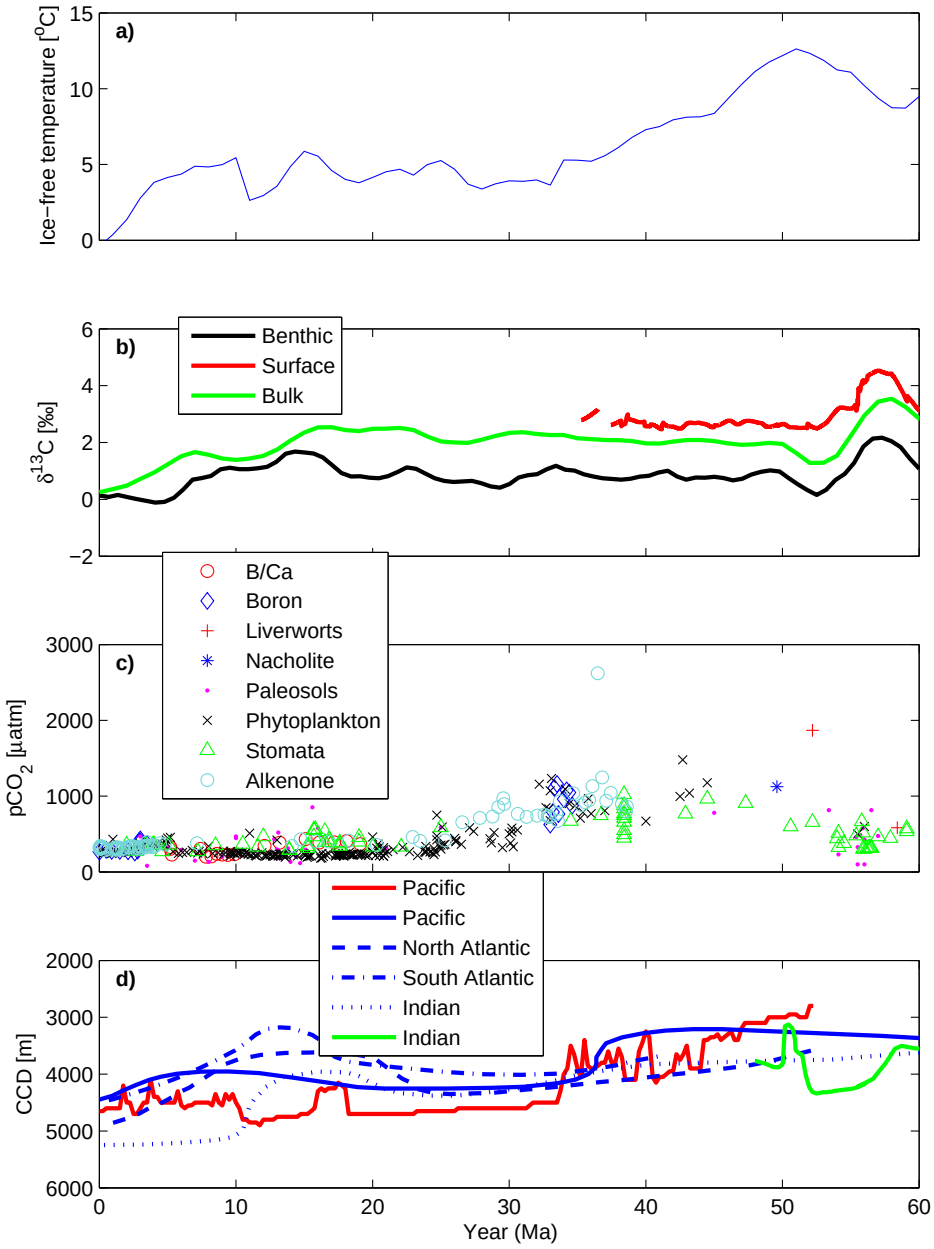
a)
Ice−free temperature [°C]
15
10
5
0
b)
Benthic
Surface
Bulk
δ13C [‰]
6
4
2
0
−2
c)
B/Ca
Boron
Liverworts
Nacholite
Paleosols
Phytoplankton
Stomata
Alkenone
pCO2 [µatm]
3000
2000
1000
0
d)
Pacific
Pacific
North Atlantic
South Atlantic
Indian
Indian
CCD [m]
2000
3000
4000
5000
6000
0
10
20
30
40
50
60
Year (Ma)

Figure 5.1:

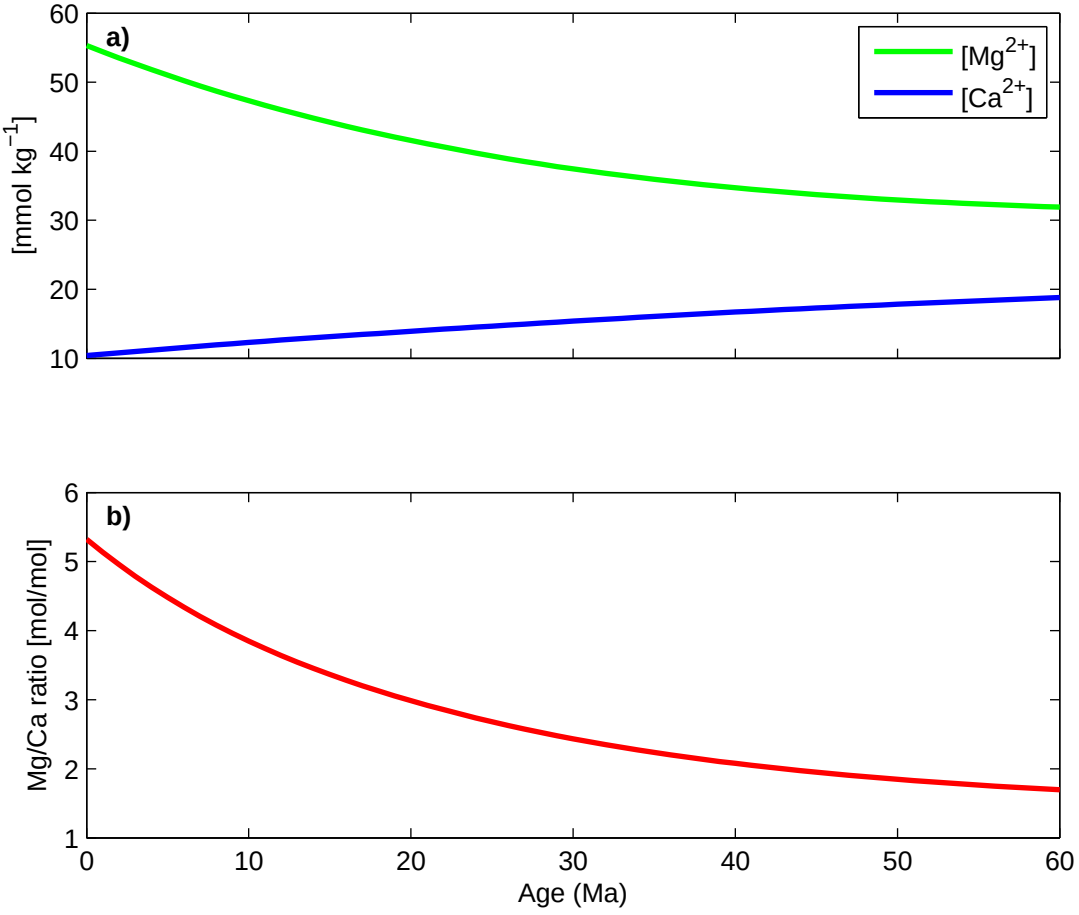
a)
[Mg2+]
[Ca2+]
[mmol kg−1]
60
50
40
30
20
10
b)
Mg/Ca ratio [mol/mol]
6
5
4
3
2
1
0
10
20
30
40
50
60
Age (Ma)

Figure 5.2:

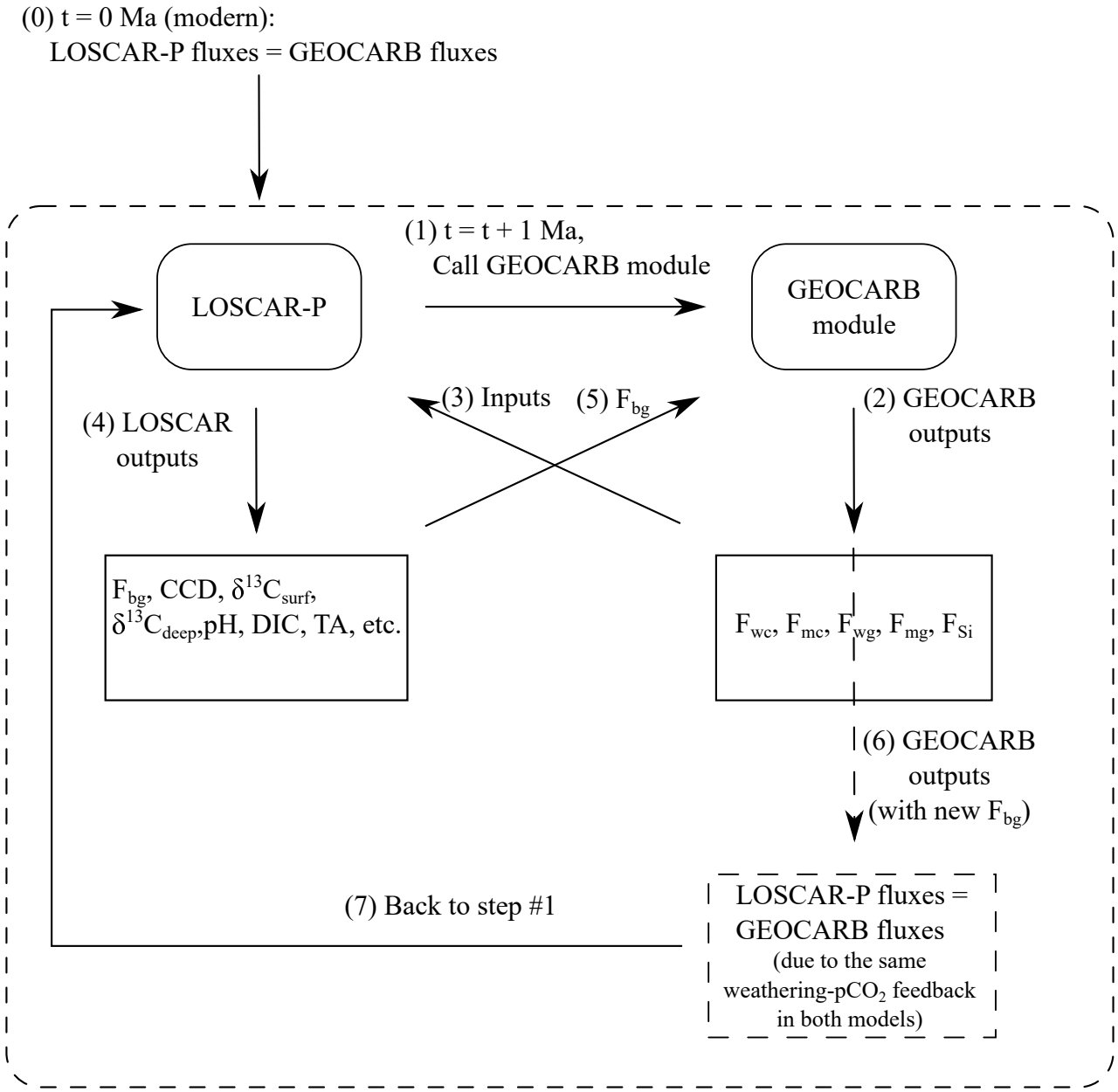
(0) t = 0 Ma (modern):
LOSCAR-P fluxes = GEOCARB fluxes
(1) t = t + 1 Ma,
Call GEOCARB module
LOSCAR-P
GEOCARB module
(3) Inputs
(5) F_{bg}
(4) LOSCAR outputs
(2) GEOCARB outputs
F_{bg}, CCD, $\delta^{13}C_{surf}$, $\delta^{13}C_{deep}$,pH, DIC, TA, etc.
F_{wc}, F_{mc}, F_{wg}, F_{mg}, F_{Si}
(6) GEOCARB outputs (with new F_{bg})
(7) Back to step #1
LOSCAR-P fluxes = GEOCARB fluxes (due to the same weathering-pCO_2 feedback in both models)

Figure 5.3:

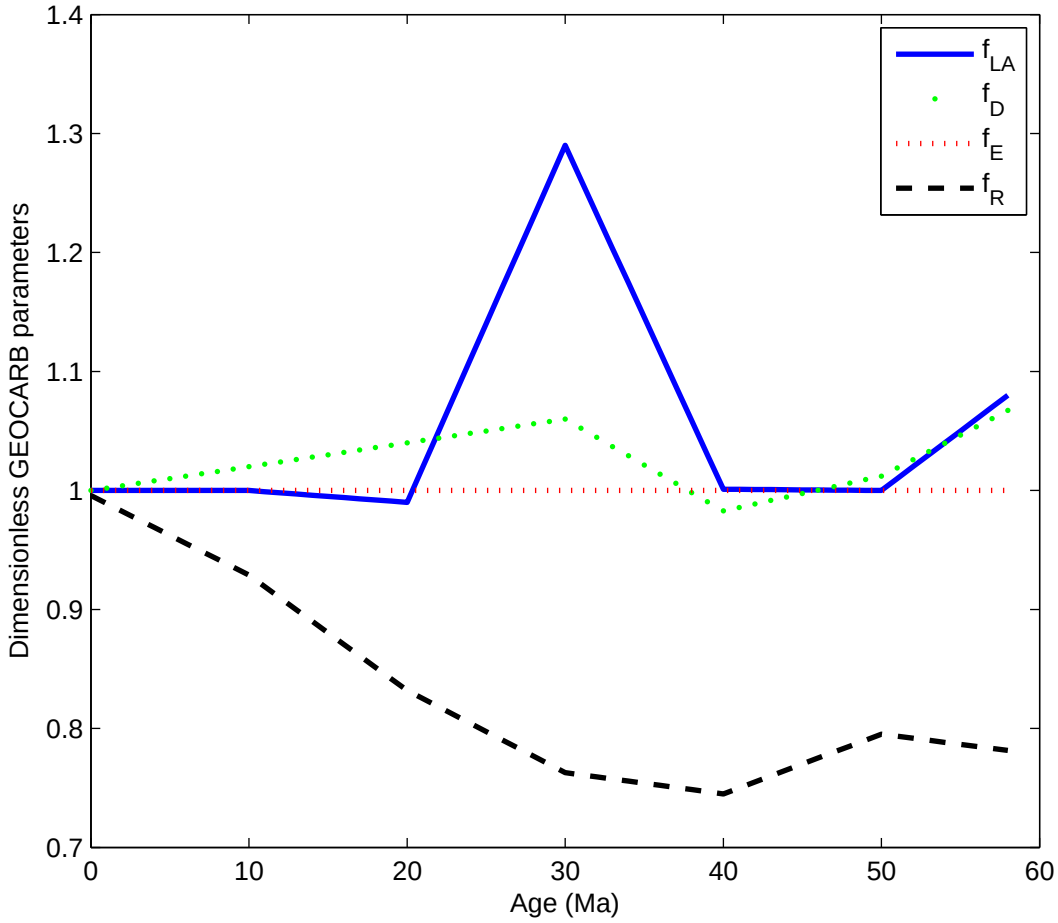
1.4
1.3
1.2
1.1
1
0.9
0.8
0.7
0
10
20
30
40
50
60
Age (Ma)
Dimensionless GEOCARB parameters
f_LA
f_D
f_E
f_R

Figure 5.4:

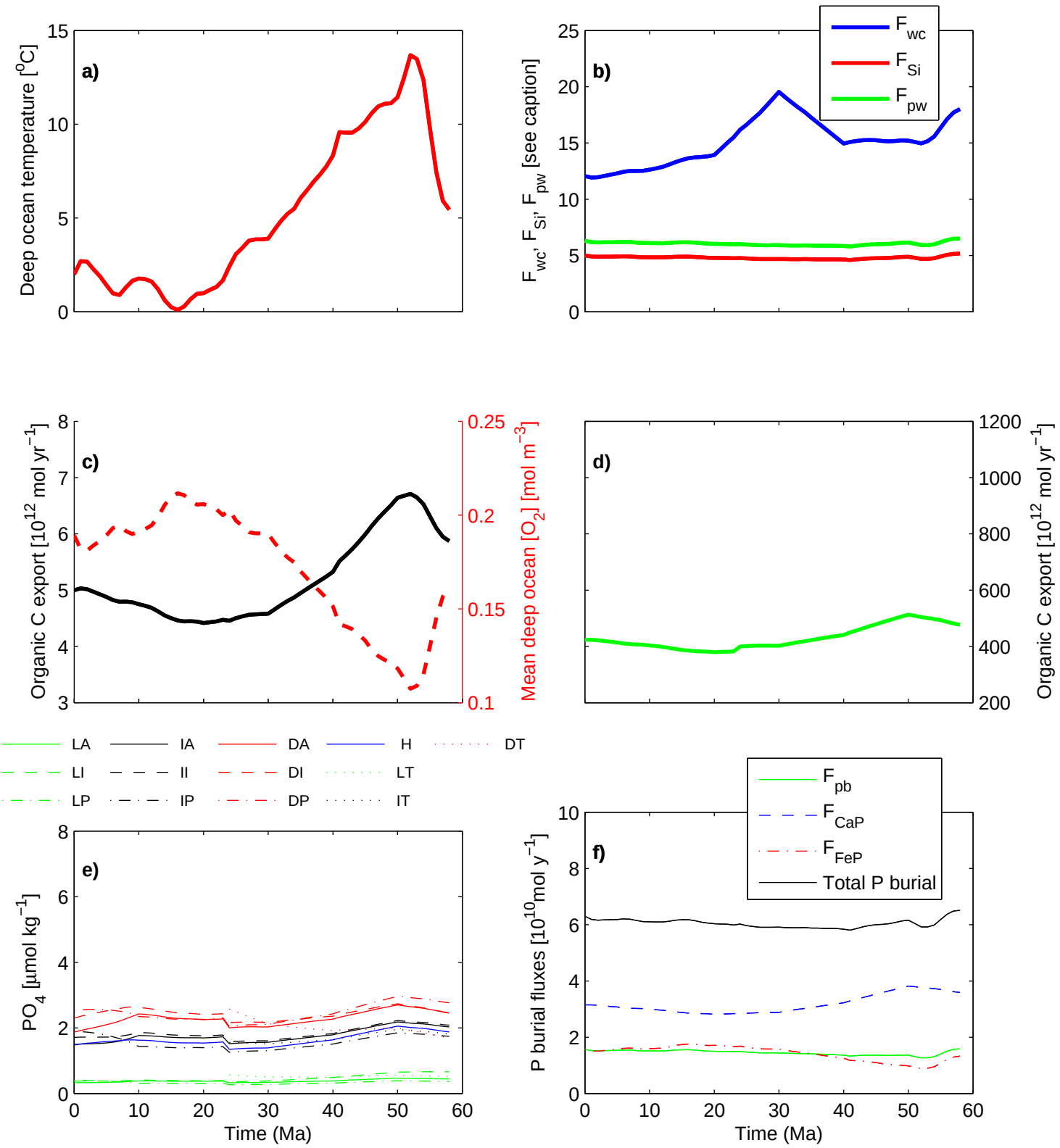

Figure 5.5: Simulation 1: Control

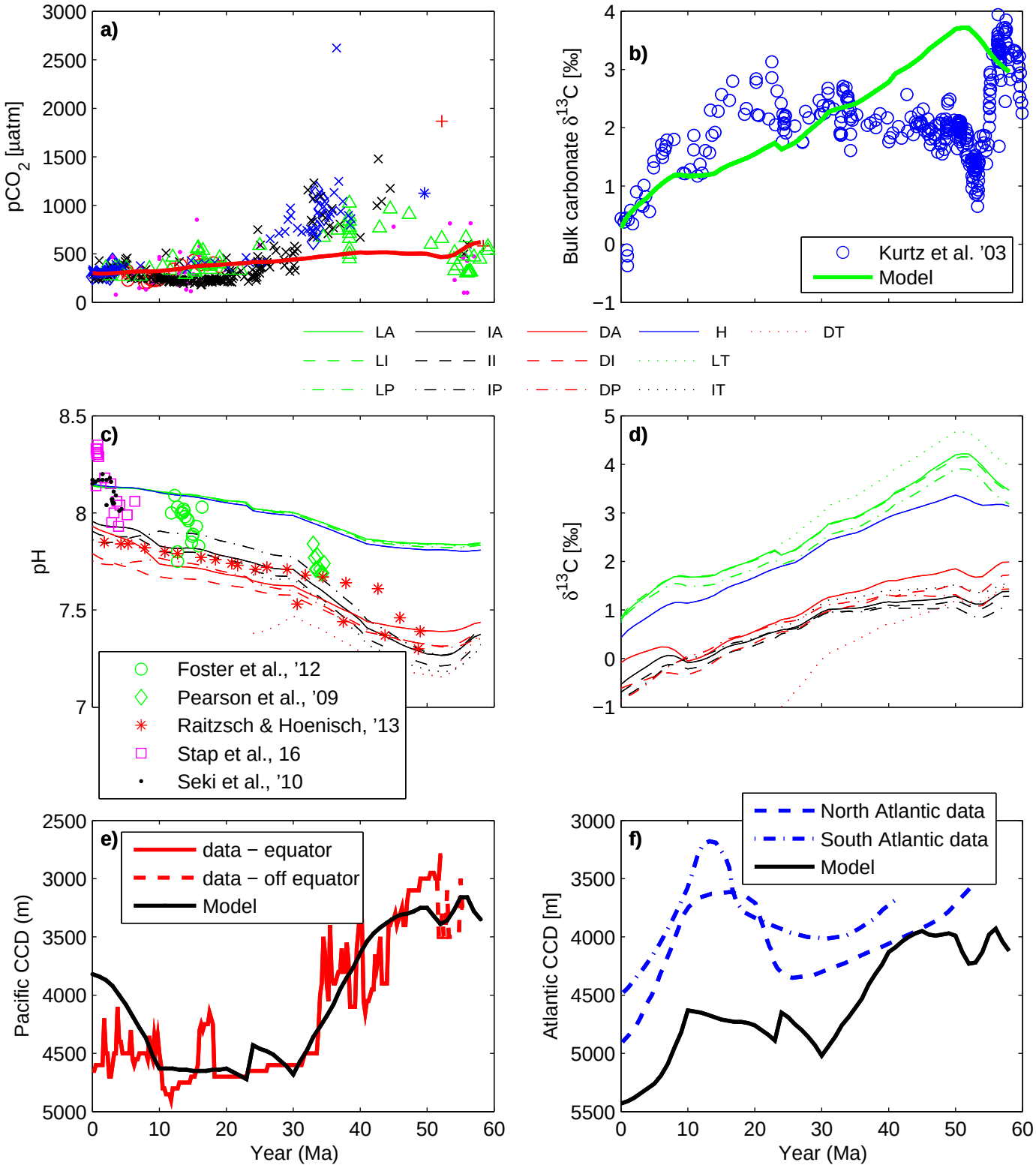

Figure 5.6: Simulation 1: Control, Data − model comparison

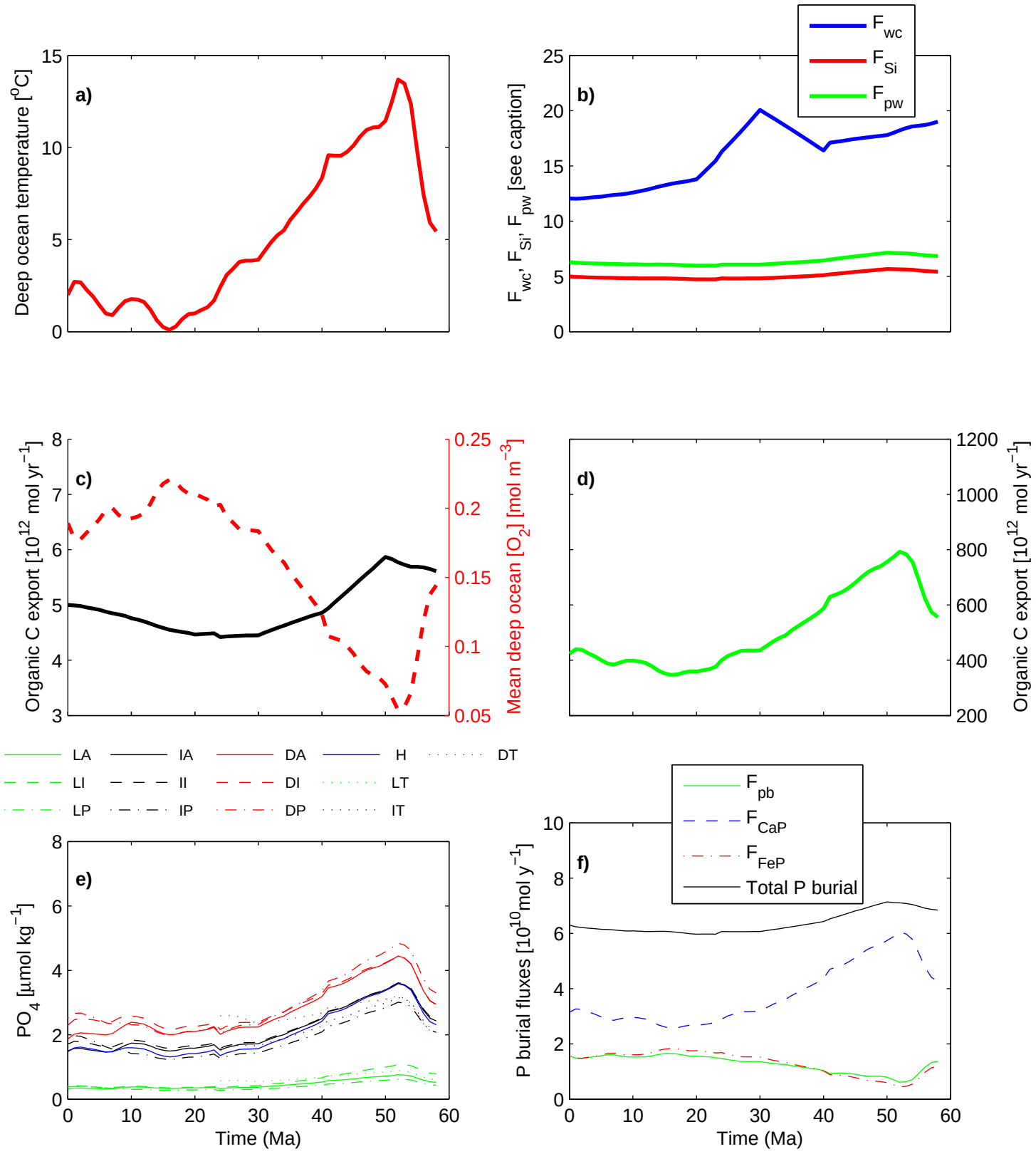

Figure 5.7: Simulation 2

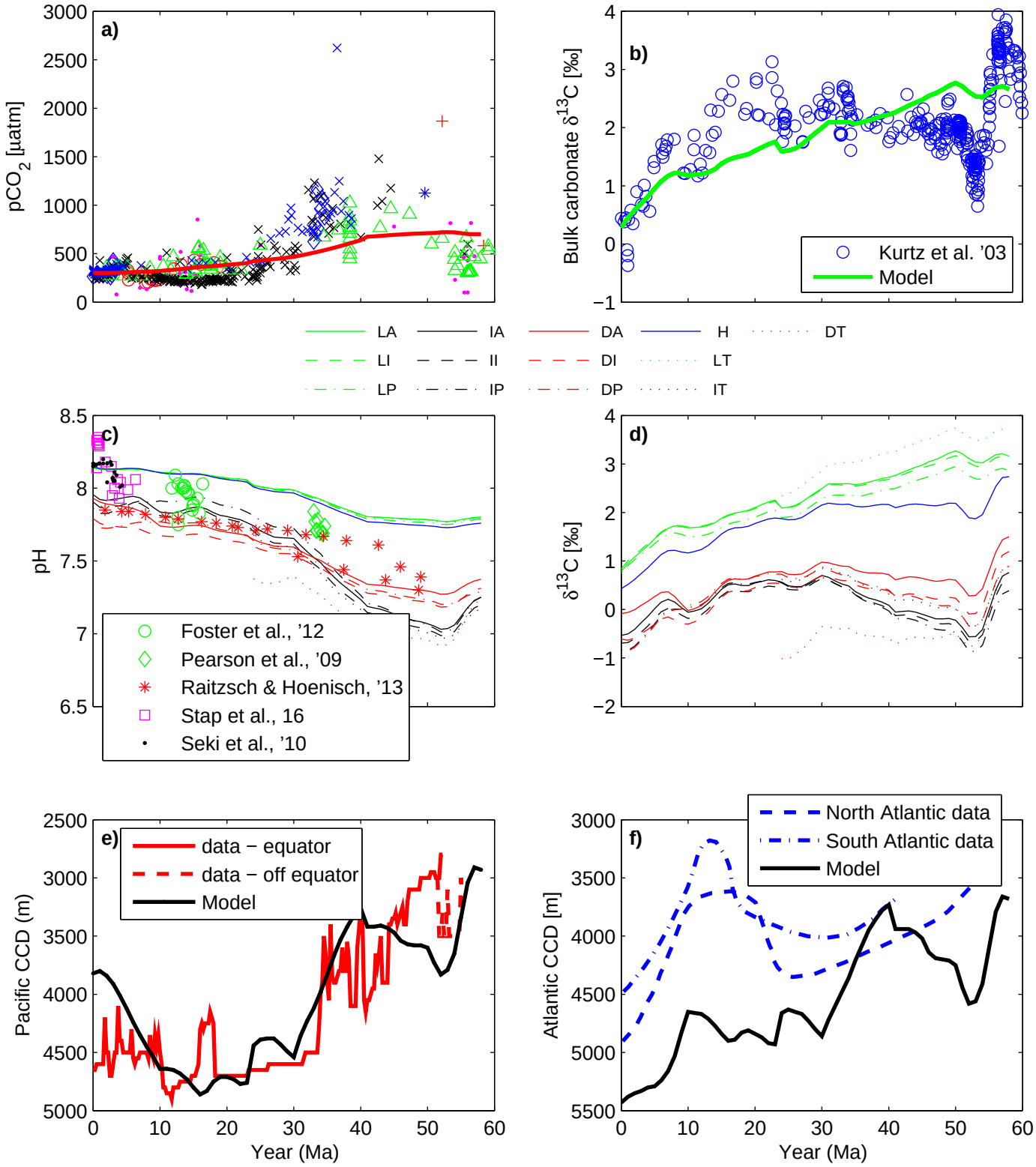

Figure 5.8: Simulation 2, Data − model comparison

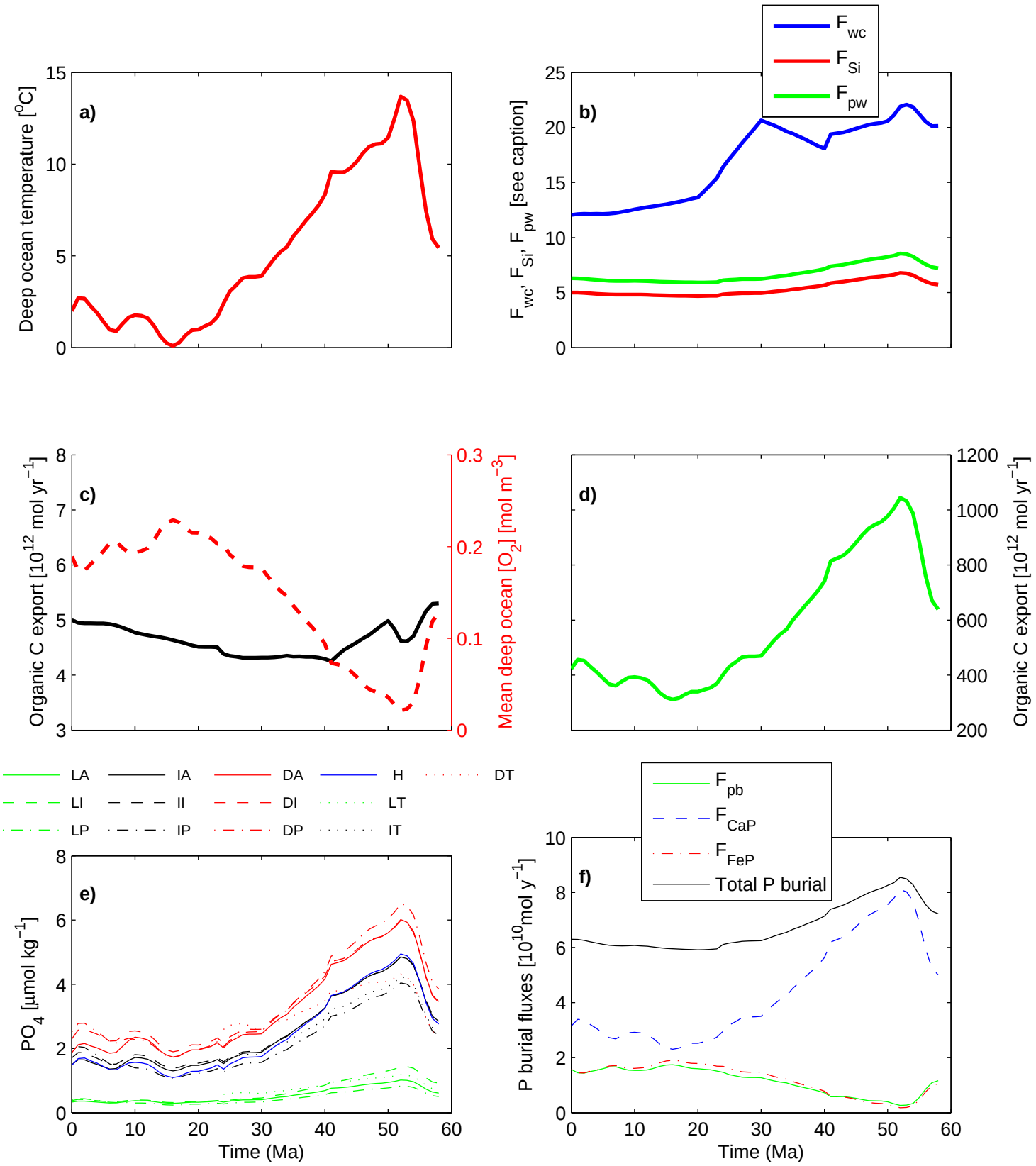

Figure 5.9: Simulation 3: Preferred

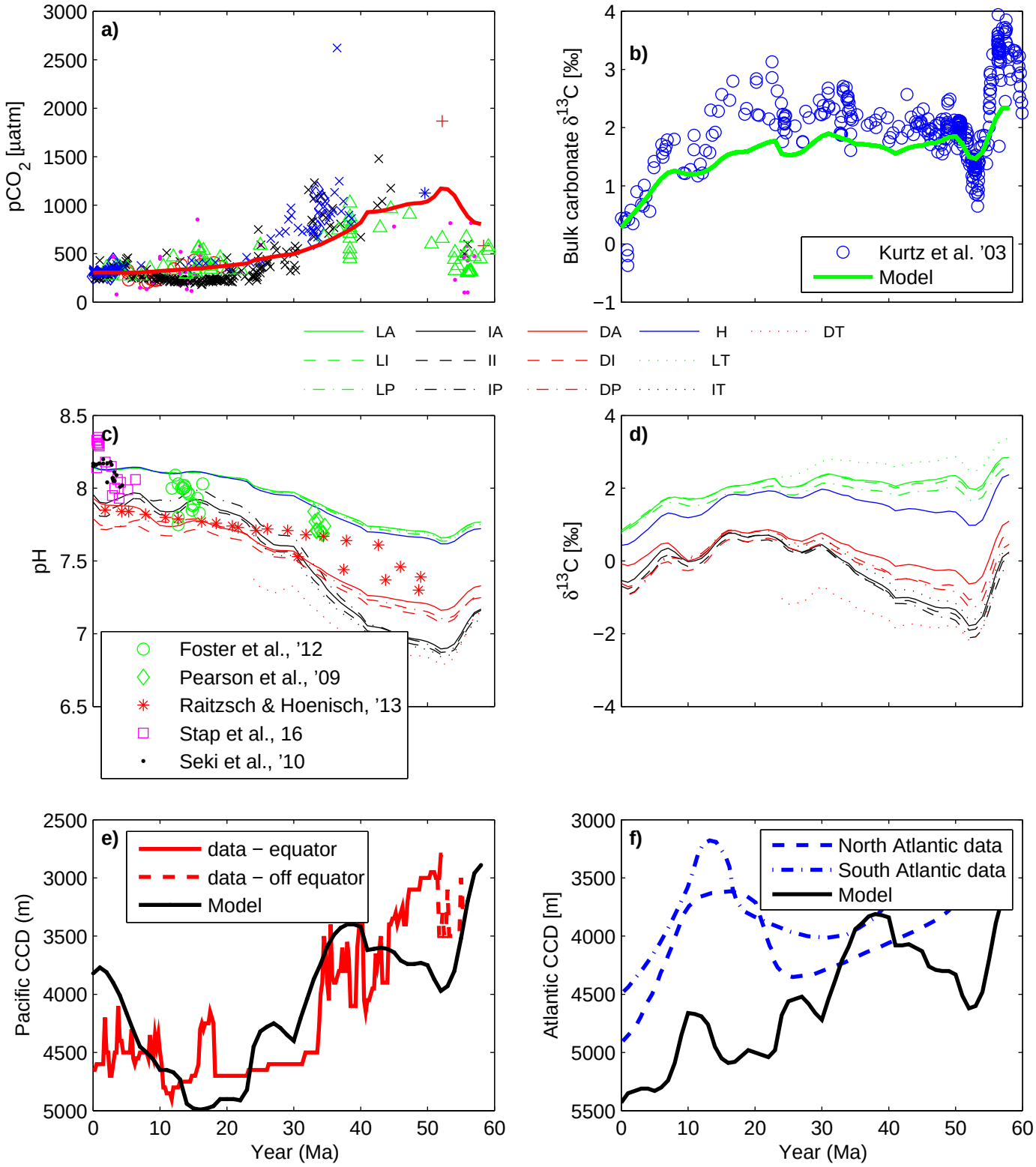

Figure 5.10: Simulation 3: Preferred, Data − model comparison

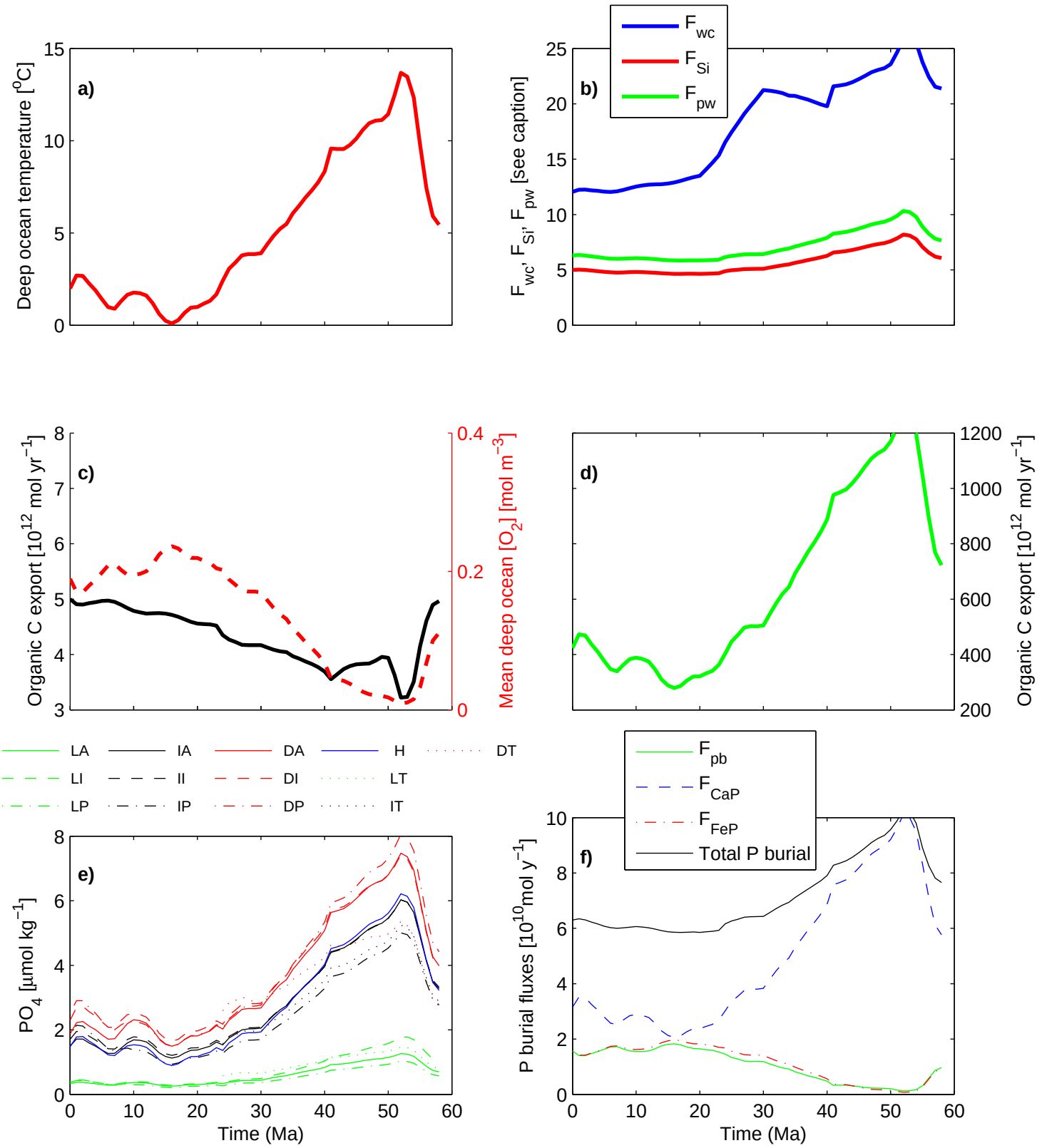

Figure 5.11: Simulation 4: High Q_r

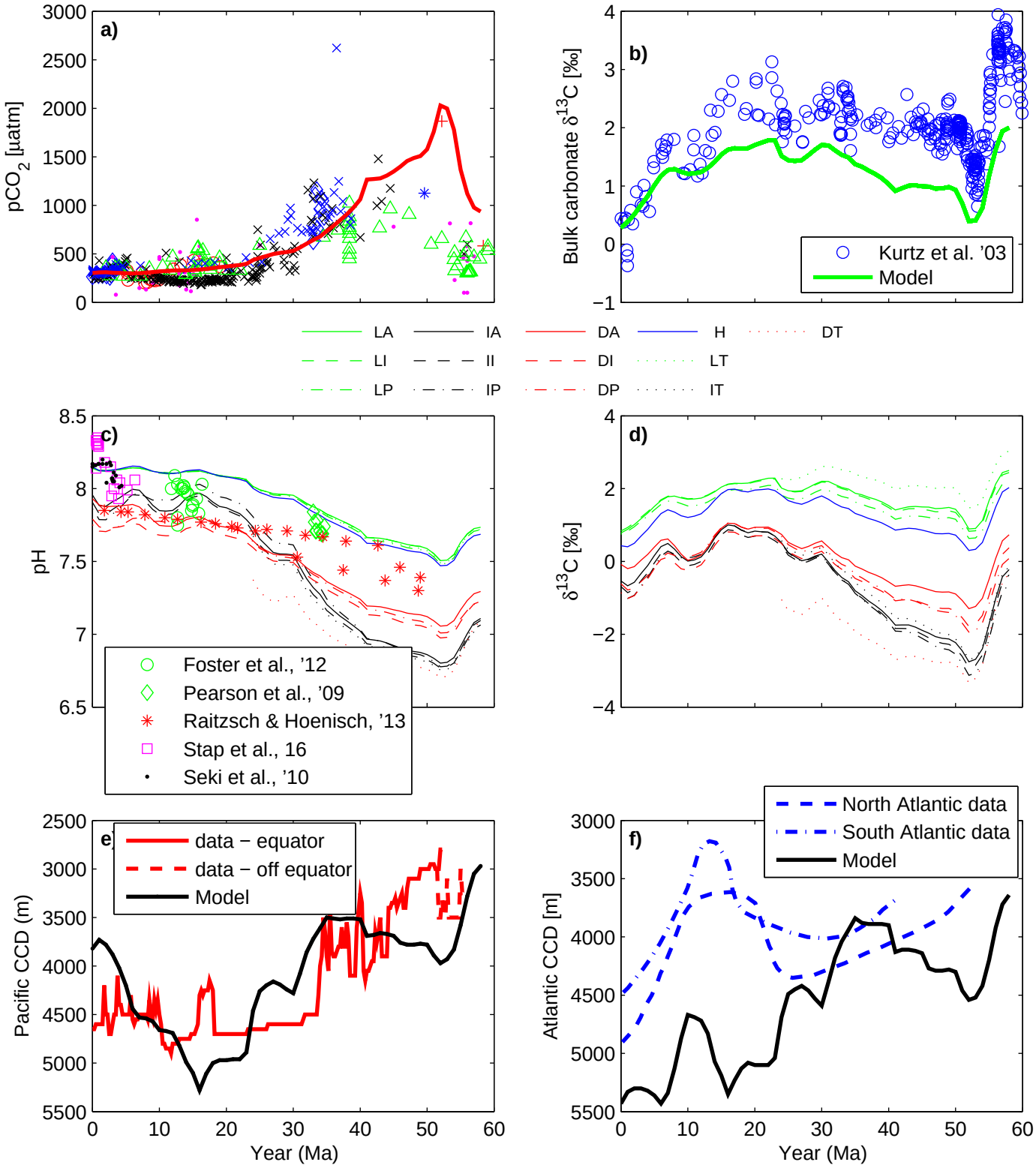

Figure 5.12: Simulation 4: High Q_r, Data − model comparison

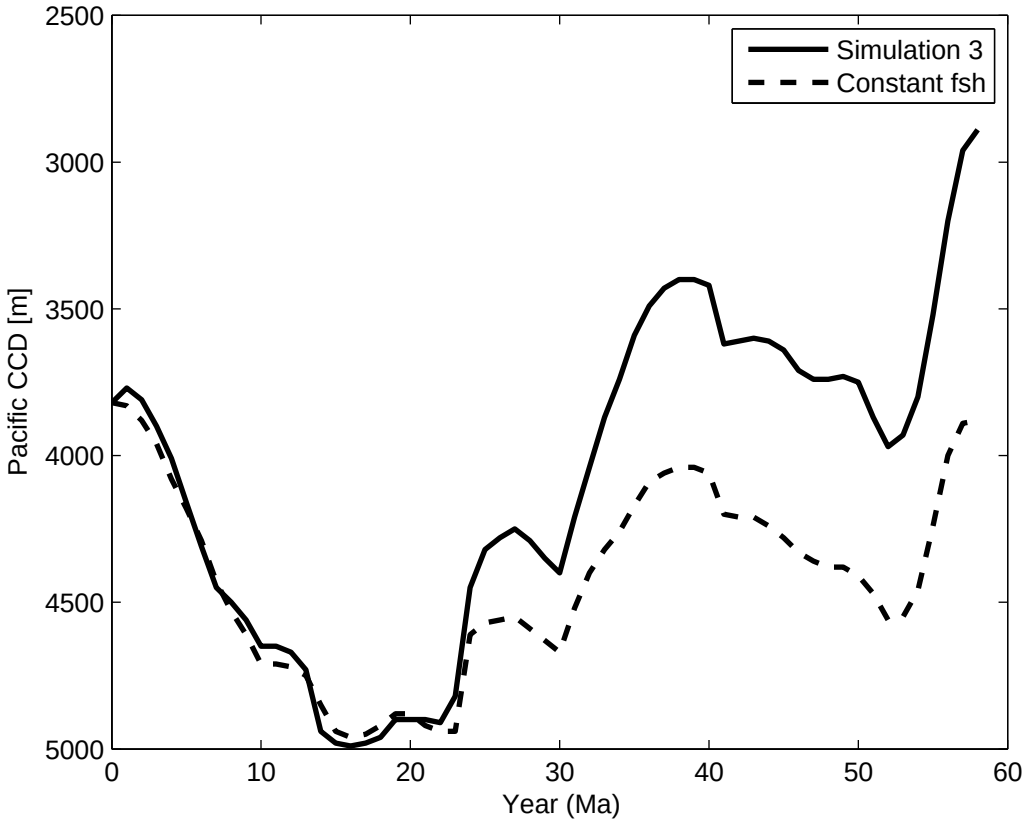
Simulation 3
Constant fsh
Pacific CCD [m]
Year (Ma)
2500
3000
3500
4000
4500
5000
0
10
20
30
40
50
60

Figure 5.13:

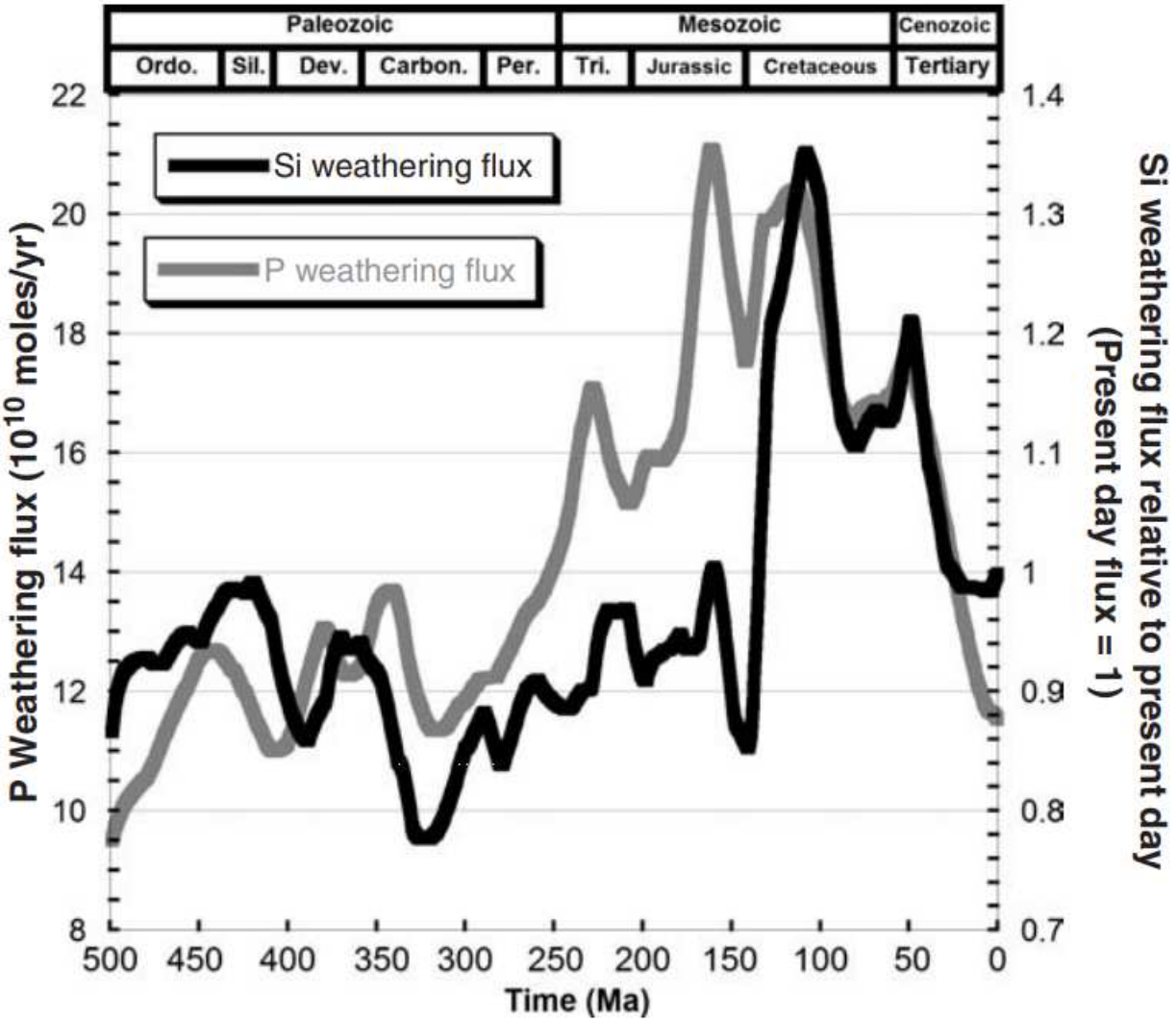
Paleozoic
Mesozoic
Cenozoic
Ordo.
Sil.
Dev.
Carbon.
Per.
Tri.
Jurassic
Cretaceous
Tertiary
Si weathering flux
P weathering flux
P Weathering flux (10^10 moles/yr)
Si weathering flux relative to present day
(Present day flux = 1)
Time (Ma)
22
20
18
16
14
12
10
8
1.4
1.3
1.2
1.1
1
0.9
0.8
0.7
500
450
400
350
300
250
200
150
100
50
0

Figure 5.14:

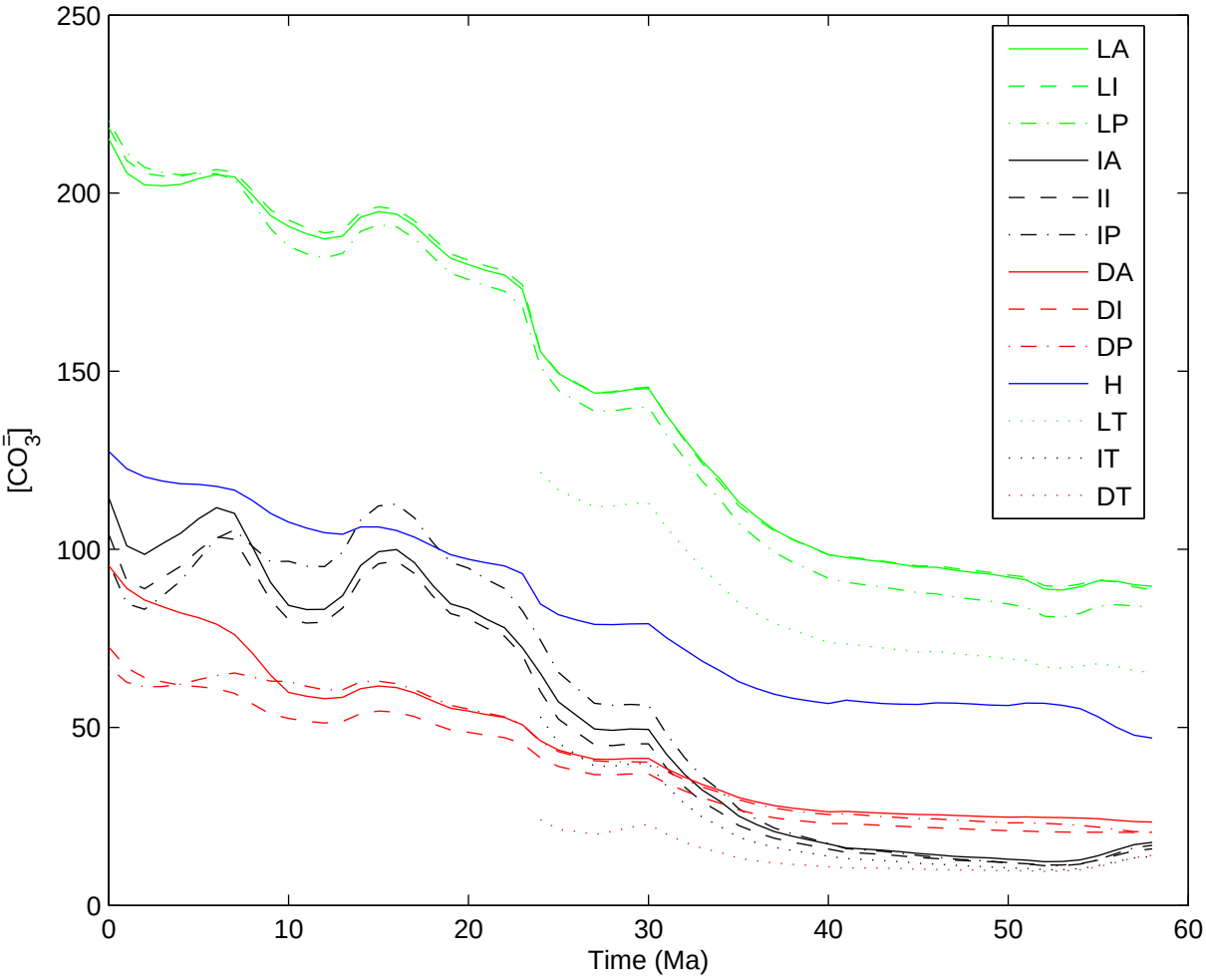
250
200
150
100
50
0
0
10
20
30
40
50
60
Time (Ma)
$[CO_3^{\bar{}}]$
LA
LI
LP
IA
II
IP
DA
DI
DP
H
LT
IT
DT

Figure 5.15:

Table 5.1: Modern steady state fluxes of phosphorus and organic carbon for the control model run. All units are in mol yr^{-1} except for isotopic values.

Symbol	*Fluxes*	*Value*	*Notes*
F_{Cexp}	Total carbon export	$\sim 424 \times 10^{12}$	
F_{Pexp}	Biological fixation of reactive P	3.260×10^{10}	$\frac{F_{Cexp}}{130}$
F_{bg}	Org. C burial	5.000×10^{12}	e.g. *Berner* [1994]
F_{bp}	Org. P burial	1.575×10^{10}	*Slomp and Van Cappellen* [2007]
F_{CaP}	CaP burial	3.150×10^{10}	*Slomp and Van Cappellen* [2007]
F_{FeP}	FeP burial	1.575×10^{10}	*Slomp and Van Cappellen* [2007]
F_{wg}	Kerogen oxidation	5.000×10^{12}	to satisfy steady-state
F_{wc}	Carbonate weathering	12.00×10^{12}	*Berner* [1994]
F_{bc}	Inorganic C burial	17.00×10^{12}	*Berner* [1994]
F_{Si}	Silicate weathering	5.000×10^{12}	$F_{bc}-F_{wc}$; *Berner* [1994]
F_{pw}	Phosphate weathering flux	6.300×10^{10}	$F_{bp} + F_{CaP} + F_{FeP}$
$\delta^{13}C_{vc}$	Carbon isotope value of volcanic flux	-4.00 ‰	constant
$\delta^{13}C_{wc}$	Carbon isotope value of riverine flux	$+2.00$ ‰	constant

Table 5.2: Physical and biogeochemical LOSCAR-P2 boundary condition.

Parameters	*Symbol*	*Modern*	*Late Paleocene*	*Other intervals*	*Unit*
Thermohaline Transport	TH	20	25	interpolated	Sv
Tethys Transport	TH_T	–	2	interpolated[1]	Sv
NADW	–	100	0	interpolated[2]	%
SO	–	0	100	interpolated[3]	%
Temperature	T	20,10,2,2 [4]	Eq.(4.2)	Eq.(4.2)	^{o}C
Shelf/deep parameter	fsh[5]	1	4.5	interpolated	–
Rain ratio	r_{rain}	6.1	6.7	interpolated	–

[1]Linearly interpolated from 0 Sv at t = 24 Ma (when Tethys first appears) to 2 Sv at 58 Ma.

[2]Linearly interpolated from 100% to 0 from 0 Ma to 10 Ma, before which NADW contribution is 0%.

[3]Linearly interpolated from 0 to 100% from 0 Ma to 10 Ma, after which SO contribution remains at 100%.

[4]Surface, Intermediate, Deep, and high latitude boxes, respectively.

[5]The number does not represent the total deposition ratio. The fsh parameter adjusts the relative amount of shelf to open ocean production.

BIBLIOGRAPHY

Amini, M., et al., Calcium isotope ($\delta^{44/40}$ ca) fractionation along hydrothermal pathways, logatchev field (mid-atlantic ridge, 14° 45' n), *Geochimica et Cosmochimica Acta*, *72*(16), 4107–4122, 2008.

Archer, D., Modeling the calcite lysocline, *J. Geophys. Res.*, *96*, 17,037–17,050, 1991.

Archer, D., A data-driven model of the global calcite lysocline, *Global Biogeochemical Cycles*, *10*(3), 511–526, 1996.

Archer, D., S. Emerson, and C. Reimers, Dissolution of calcite in deep-sea sediments: ph and o2 microelectrode results, *Geochimica et Cosmochimica Acta*, *53*(11), 2831–2845, 1989.

Arvidson, R. S., F. T. Mackenzie, and M. Guidry, Magic: A phanerozoic model for the geochemical cycling of major rock-forming components, *American Journal of Science*, *306*(3), 135–190, 2006.

Bains, S., R. D. Norris, R. M. Corfield, and K. L. Faul, Termination of global warmth at the palaeocene/eocene boundary through productivity feedback, *Nature*, *407*(6801), 171–174, 2000.

Beerling, D. J., and D. L. Royer, Convergent cenozoic CO_2 history, *Nature Geoscience*, *4*(7), 418–420, 2011.

Bergman, N. M., T. M. Lenton, and A. J. Watson, Copse: a new model of biogeochemical cycling over phanerozoic time, *American Journal of Science*, *304*(5), 397–437, 2004.

Berner, R. A., Burial of organic carbon and pyrite sulfur in the modern ocean: its geochemical and environmental significance, *Am. J. Sci.;(United States)*, *282*, 1982.

Berner, R. A., A model for atmospheric CO_2 over Phanerozoic time, *Am. J. Sci.*, *291*, 339–376, 1991.

Berner, R. A., GEOCARB II: A revised model of atmospheric CO_2 over Phanerozoic time, *Am. J. Sci*, *294*, 56–91, 1994.

Berner, R. A., A New Look at the Long-term Carbon Cycle, *GSA Today*, *9*, 1–6, 1999.

Berner, R. A., and E. K. Berner, Silicate weathering and climate, in *Tectonic uplift and climate change*, pp. 353–365, Springer, 1997.

Berner, R. A., and K. Caldeira, The need for mass balance and feedback in the geochemical carbon cycle, *Geology*, *25*, 955–956, 1997.

Berner, R. A., and Z. Kothavala, GEOCARB III: A revised model of atmospheric CO_2 over Phanerozoic time, *Am. J. Sci*, *304*, 397–437, 2001.

Berner, R. A., A. C. Lasaga, and R. M. Garrels, The carbonate-silicate geochemical cycle and its effect on atmospheric carbon dioxide over the past 100 million years, *Am. J. Sci.*, *283*, 641–683, 1983.

Bice, K. L., E. J. Barron, and W. H. Peterson, Reconstruction of realistic early eocene paleobathymetry and ocean gcm sensitivity to specified basin configuration, in *Tectonic Boundary Conditions for Climate Reconstructions*, edited by T. J. Crowley and K. C. Burke, pp. 227 – 247, Oxford University Press, 1998.

Bijl, P. K., S. Schouten, A. Sluijs, G. J. Reichart, J. C. Zachos, and H. Brinkhuis, Early Palaeogene temperature evolution of the southwest Pacific Ocean, *Nature*, *461*, 776–779, 2009.

Bowen, G. J., Up in smoke: A role for organic carbon feedbacks in paleogene hyperthermals, *Global and planetary change*, *109*, 18–29, 2013.

Bowen, G. J., and J. C. Zachos, Rapid carbon sequestration at the termination of the palaeocene-eocene thermal maximum, *Nature Geoscience*, *3*(12), 866–869, 2010.

Bowring, S. A., D. Erwin, Y. Jin, M. Martin, K. Davidek, and W. Wang, U/pb zircon geochronology and tempo of the end-permian mass extinction, *Science*, *280*(5366), 1039–1045, 1998.

Brazier, J.-M., G. Suan, T. Tacail, L. Simon, J. E. Martin, E. Mattioli, and V. Balter, Calcium isotope evidence for dramatic increase of continental weathering during the toarcian oceanic anoxic event (early jurassic), *Earth and Planetary Science Letters*, *411*, 164–176, 2015.

Broecker, W. S., Ocean chemistry during glacial times, *Geochim. Cosmochim. Acta*, *46*, 1689–1705, 1982.

Buesseler, K. O., et al., Revisiting carbon flux through the ocean's twilight zone, *science*, *316*(5824), 567–570, 2007.

Caldeira, K., and M. R. Rampino, Aftermath of the end-Cretaceous mass extinction: Possible biogeochemical stabilization of the carbon cycle and climate, *Paleoceanography*, *8*, 515–525, 1993.

Caves, J. K., A. B. Jost, K. V. Lau, and K. Maher, Cenozoic carbon cycle imbalances and a variable weathering feedback, *Earth and Planetary Science Letters*, *450*, 152–163, 2016.

Chun, C. O., M. L. Delaney, and J. C. Zachos, Paleoredox changes across the paleocene-eocene thermal maximum, walvis ridge (odp sites 1262, 1263, and 1266): Evidence from mn and u enrichment factors, *Paleoceanography*, *25*(4), 2010.

Clarkson, M., et al., Ocean acidification and the permo-triassic mass extinction, *Science*, *348*(6231), 229–232, 2015.

Cook, P. J., and M. McElhinny, A reevaluation of the spatial and temporal distribution of sedimentary phosphate deposits in the light of plate tectonics, *Economic Geology*, *74*(2), 315–330, 1979.

Corsetti, F. A., A. Baud, P. J. Marenco, and S. Richoz, Summary of early triassic carbon isotope records, *Comptes Rendus Palevol*, *4*(6), 473–486, 2005.

Coxall, H. K., P. A. Wilson, H. Pälike, C. H. Lear, and J. Backman, Rapid stepwise onset of antarctic glaciation and deeper calcite compensation in the pacific ocean, *Nature*, *433*(7021), 53–57, 2005.

Cramer, B. S., J. R. Toggweiler, J. D. Wright, M. E. Katz, , and K. G. Miller, Ocean overturning since the Late Cretaceous: Inferences from a new benthic foraminiferal isotope compilation, *Paleoceanogaphy*, *24*, PA4216, 2009.

Cui, Y., and L. R. Kump, Global warming and the end-permian extinction event: Proxy and modeling perspectives, *Earth-Science Reviews*, 2014.

DeConto, R. M., S. Galeotti, M. Pagani, D. Tracy, K. Schaefer, T. Zhang, D. Pollard, and D. J. Beerling, Past extreme warming events linked to massive carbon release from thawing permafrost, *Nature*, *484*(7392), 87–91, 2012.

Delaney, M. L., and G. M. Filippelli, An apparent contradiction in the role of phosphorus in cenozoic chemical mass balances for the world ocean, *Paleoceanography*, *9*(4), 513–527, 1994.

Dickens, G. R., Carbon addition and removal during the Late Palaeocene Thermal Maximum: basic theory with a preliminary treatment of the isotope record at ODP Site 1051, Blake Nose, in *Western North Atlantic Palaeogene and Cretaceous Palaeoceanography*, edited by Kroon, D., Norris, R. D., and Klaus, A., pp. 293–305, Geol. Soc. London. Special Publication 183, 2001.

Dickens, G. R., Rethinking the global carbon cycle with a large, dynamic and microbially mediated gas hydrate capacitor, *Earth Planet. Sci. Lett.*, *213*, 169–183, 2003.

Dickens, G. R., Down the Rabbit Hole: toward appropriate discussion of methane release from gas hydrate systems during the Paleocene-Eocene thermal maximum and other past hyperthermal events, *Climate of the Past*, *7*, 831–846, 2011.

Dickens, G. R., and J. Backman, Core alignment and composite depth scale for the lower Paleogene through uppermost Cretaceous interval at Deep Sea Drilling Project Site 577, *Newsletters on Stratigraphy*, 2013.

Dickens, G. R., J. R. O'Neil, D. K. Rea, and R. M. Owen, Dissociation of oceanic methane hy-

drate as a cause of the carbon isotope excursion at the end of the Paleocene, *Paleoceanogr.*, *10*, 965–971, 1995.

Dickens, G. R., M. M. Castillo, and J. C. G. Walker, A blast of gas in the latest Paleocene; simulating first-order effects of massive dissociation of oceanic methane hydrate, *Geology*, *25*, 259–262, 1997.

Dickson, A. J., A. S. Cohen, and A. L. Coe, Seawater oxygenation during the paleocene-eocene thermal maximum, *Geology*, *40*(7), 639–642, 2012.

Dickson, A. J., R. L. Rees-Owen, C. März, A. L. Coe, A. S. Cohen, R. D. Pancost, K. Taylor, and E. Shcherbinina, The spread of marine anoxia on the northern tethys margin during the paleocene-eocene thermal maximum, *Paleoceanography*, *29*(6), 471–488, 2014.

Elderfield, H., and A. Schultz, Mid-ocean ridge hydrothermal fluxes and the chemical composition of the ocean, *Annual Review of Earth and Planetary Sciences*, *24*, 191–224, 1996.

Emerson, S., and D. Archer, Calcium carbonate preservation in the ocean, *Philosophical Transactions of the Royal Society of London A: Mathematical, Physical and Engineering Sciences*, *331*(1616), 29–40, 1990.

Eppley, R. W., Temperature and phytoplankton growth in the sea, *Fish. Bull*, *70*(4), 1063–1085, 1972.

Erba, E., The first 150 million years history of calcareous nannoplankton: biosphere–geosphere interactions, *Palaeogeography, Palaeoclimatology, Palaeoecology*, *232*(2), 237–250, 2006.

Erwin, D. H., *The great Paleozoic crisis: life and death in the Permian*, Columbia University Press, 1993.

Fantle, M. S., Evaluating The Ca Isotope Proxy, *American Journal of Science*, *310*, 194–230, 2010.

Fantle, M. S., and D. J. DePaolo, Ca isotopes in carbonate sediment and pore fluid from odp site 807a: The ca^{2+}(aq)–calcite equilibrium fractionation factor and calcite recrystallization rates in pleistocene sediments, *Geochimica et Cosmochimica Acta*, *71*(10), 2524–2546, 2007.

Fantle, M. S., and E. T. Tipper, Calcium isotopes in the global biogeochemical ca cycle: Implications for development of a ca isotope proxy, *Earth-Science Reviews*, *129*, 148–177, 2014.

Farley, K. A., and S. F. Eltgroth, An alternative age model for the Paleocene-Eocene thermal maximum using extraterrestrial ^{3}He, *Earth Planet Sci. Lett.*, *208*, 135–148, 2003.

Filippelli, G. M., Carbon and phosphorus cycling in anoxic sediments of the saanich inlet, british columbia, *Marine Geology*, *174*(1), 307–321, 2001.

Filippelli, G. M., and M. L. Delaney, The oceanic phosphorus cycle and continental weathering during the neogene, *Paleoceanography*, *9*(5), 643–652, 1994.

Flögel, S., K. Wallmann, C. Poulsen, J. Zhou, A. Oschlies, S. Voigt, and W. Kuhnt, Simulating the biogeochemical effects of volcanic co_2 degassing on the oxygen-state of the deep ocean during the cenomanian/turonian anoxic event (oae2), *Earth and Planetary Science Letters*, *305*(3), 371–384, 2011.

Foster, G. L., C. H. Lear, and J. W. Rae, The evolution of pco 2, ice volume and climate during the middle miocene, *Earth and Planetary Science Letters*, *341*, 243–254, 2012.

Gibbs, S. J., T. J. Bralower, P. R. Bown, J. C. Zachos, and L. M. Bybell, Shelf and open-ocean calcareous phytoplankton assemblages across the paleocene-eocene thermal maximum: Implications for global productivity gradients, *Geology*, *34*(4), 233–236, 2006.

Gibbs, S. J., H. M. Stoll, P. R. Bown, and T. J. Bralower, Ocean acidification and surface water carbonate production across the paleocene–eocene thermal maximum, *Earth and Planetary Science Letters*, *295*(3), 583–592, 2010.

Grotzinger, J. P., and A. H. Knoll, Anomalous carbonate precipitates: is the precambrian the key to the permian?, *Palaios*, pp. 578–596, 1995.

Guidry, M. W., R. S. Arvidson, and F. T. Mackenzie, Biological and geochemical forcings to phanerozoic change in seawater, atmosphere, and carbonate precipitate composition, *Evolution of Primary Producers in the Sea*, *15*, 377–403, 2007.

Gussone, N., F. Böhm, A. Eisenhauer, M. Dietzel, A. Heuser, B. M. Teichert, J. Reitner, G. Wörheide, and W.-C. Dullo, Calcium isotope fractionation in calcite and aragonite, *Geochimica et Cosmochimica Acta*, *69*(18), 4485–4494, 2005.

Hartnett, H. E., R. G. Keil, J. I. Hedges, and A. H. Devol, Influence of oxygen exposure time on organic carbon preservation in continental margin sediments, *Nature*, *391*(6667), 572–575, 1998.

Herold, N., M. Seton, R. D. Müller, Y. You, and M. Huber, Middle Miocene tectonic

boundary conditions for use in climate models, *Geochem. Geophys. Geosyst.*, *9*, Q10,009, doi:10.1029/2008GC002,046, 2008.

Hilting, A. K., L. R. Kump, and T. J. Bralower, Variations in the oceanic vertical carbon isotope gradient and their implications for the Paleoce-Eocene biological pump, *Paleoceanography*, *23*, 2008.

Hinojosa, J. L., S. T. Brown, J. Chen, D. J. DePaolo, A. Paytan, S.-z. Shen, and J. L. Payne, Evidence for end-permian ocean acidification from calcium isotopes in biogenic apatite, *Geology*, *40*(8), 743–746, 2012.

Holser, W. T., et al., A unique geochemical record at the permian/triassic boundary, *Nature*, *337*(6202), 39–44, 1989.

Horita, J., H. Zimmermann, and H. D. Holland, Chemical evolution of seawater during the Phanerozoic: Implications from the record of marine evaporites, *Geochim. Cosmochim. Acta*, *66(21)*, 3733–3756, 2002.

Howarth, R., H. S. Jensen, R. Marino, and H. Postma, Transport to and processing of p in near-shore and oceanic waters, *Scope*, *54*, 323–345, 1995.

Ingall, E. D., R. Bustin, and P. Van Cappellen, Influence of water column anoxia on the burial and preservation of carbon and phosphorus in marine shales, *Geochimica et Cosmochimica Acta*, *57*(2), 303–316, 1993.

IPCC, I. P. o. C. C., *Climate Change 2007: The Physical Science Basis*, Cambridge University Press, Cambridge, 996 pp., 2007.

Ivanov, A. V., H. He, L. Yan, V. V. Ryabov, A. Y. Shevko, S. V. Palesskii, and I. V. Nikolaeva, Siberian traps large igneous province: Evidence for two flood basalt pulses around the permo-triassic boundary and in the middle triassic, and contemporaneous granitic magmatism, *Earth-Science Reviews*, *122*, 58–76, 2013.

Jahnke, R. A., The global ocean flux of particulate organic carbon: Areal distribution and magnitude, *Global biogeochemical cycles*, *10*(1), 71–88, 1996.

John, C. M., S. M. Bohaty, J. C. Zachos, A. Sluijs, S. Gibbs, H. Brinkhuis, and T. J. Bralower, North american continental margin records of the paleocene-eocene thermal maximum: Implications for global carbon and hydrological cycling, *Paleoceanography*, *23*(2), 2008.

Kamo, S., J. Crowley, and S. Bowring, The permian-triassic boundary event and eruption of the siberian flood basalts: An inter-laboratory u–pb dating study, *Geochimica et Cosmochimica Acta*, *70*(18), A303, 2006.

Kelly, D. C., J. C. Zachos, T. J. Bralower, and S. A. Schellenberg, Enhanced terrestrial weathering/runoff and surface-ocean carbonate production during the recovery stages of the Paleocene-Eocene Thermal Maximum, *Paleoceanogr.*, *20*, PA4023 doi:10.1029/2005PA001,163, 2005.

Kelly, D. C., T. M. Nielsen, H. K. McCarren, J. C. Zachos, and U. Röhl, Spatiotemporal patterns of carbonate sedimentation in the south atlantic: Implications for carbon cycling during the paleocene–eocene thermal maximum, *Palaeogeography, Palaeoclimatology, Palaeoecology*, *293*(1), 30–40, 2010.

Kennett, J. P., and L. D. Stott, Abrupt deep-sea warming, palaeoceanographic changes and benthic extinctions at the end of the Palaeocene, *Nature*, *353*, 225–229, 1991.

Knoll, A. H., R. Bambach, D. Canfield, and J. Grotzinger, Comparative earth history and late permian mass extinction, *SCIENCE-NEW YORK THEN WASHINGTON-*, pp. 452–457, 1996.

Knoll, A. H., R. K. Bambach, J. L. Payne, S. Pruss, and W. W. Fischer, Paleophysiology and end-permian mass extinction, *Earth and Planetary Science Letters*, *256*(3), 295–313, 2007.

Komar, N., and R. Zeebe, Calcium and calcium isotope changes during carbon cycle perturbations at the end-permian, *Paleoceanography*, *31*(1), 115–130, 2016.

Komar, N., and R. Zeebe, Redox-controlled carbon and phosphorus burial: A mechanism for enhanced organic carbon sequestration during the petm, *Earth Planet. Sci. Lett*, p. http://dx.doi.org/10.1016/j.epsl.2017.09.011, 2017.

Komar, N., and R. E. Zeebe, Changes in oceanic calcium from enhanced weathering did not affect calcium-based proxies during the Paleocene-Eocene Thermal Maximum, *Paleoceanography*, *26*, doi:10.1029/2010PA001,979, 2011.

Komar, N., R. Zeebe, and G. Dickens, Understanding long-term carbon cycle trends: The late paleocene through the early eocene, *Paleoceanography*, *28*(4), 650–662, 2013.

Kominz, M. A., J. Browning, K. Miller, P. Sugarman, S. Mizintseva, and C. Scotese, Late cretaceous to miocene sea-level estimates from the new jersey and delaware coastal plain coreholes: An error analysis, *Basin Research*, *20*(2), 211–226, 2008.

Kump, L. R., and M. A. Arthur, Interpreting carbon-isotope excursions: carbonates and organic matter, *Chemical Geology*, *161*, 181–198, 1999.

Kump, L. R., S. L. Brantley, and M. A. Arthur, Chemical weathering, atmospheric CO_2, and climate, *Annu. Rev. Earth Planet. Sci.*, *28*, 611–667, 2000.

Kurtz, A., L. R. Kump, M. A. Arthur, J. C. Zachos, and A. Paytan, Early Cenozoic decoupling of the global carbon and sulfur cycles, *Paleoceanogr.*, *18*, 1090, 2003.

Kwon, E. Y., F. Primeau, and J. L. Sarmiento, The impact of remineralization depth on the air-sea carbon balance, *Nature Geoscience*, *2*(9), 630, 2009.

Laws, E. A., P. G. Falkowski, W. O. Smith, H. Ducklow, and J. J. McCarthy, Temperature effects on export production in the open ocean, *Global Biogeochemical Cycles*, *14*(4), 1231–1246, 2000.

Lear, C., H. Elderfield, and P. Wilson, Cenozoic deep-sea temperatures and global ice volumes from mg/ca in benthic foraminiferal calcite, *Science*, *287*(5451), 269–272, 2000.

Lemarchand, D., G. J. Wasserburg, and D. A. Papanastassiou, Rate-controlled calcium isotope fractionation in synthetic calcite, *Geochim. Cosmochim. Acta*, *68(22)*, 4665–4678, 2004.

Lenton, T. M., and A. J. Watson, Redfield revisited: 1. regulation of nitrate, phosphate, and oxygen in the ocean, *Global Biogeochemical Cycles*, *14*(1), 225–248, 2000.

Leon-Rodriguez, L., and G. R. Dickens, Constraints on ocean acidification associated with rapid and massive carbon injections: The early paleogene record at ocean drilling pro-

gram site 1215, equatorial pacific ocean, *Palaeogeography, Palaeoclimatology, Palaeoecology*, *298*(3), 409–420, 2010.

Li, G., and H. Elderfield, Evolution of carbon cycle over the past 100 million years, *Geochimica et Cosmochimica Acta*, *103*, 11–25, 2013.

Lightfoot, P. C., and R. R. Keays, Siderophile and chalcophile metal variations in flood basalts from the siberian trap, norilsk region: Implications for the origin of the ni-cu-pge sulfide ores, *Economic Geology*, *100*(3), 439–462, 2005.

Lowenstein, T. K., and R. V. Demicco, Elevated eocene atmospheric co2 and its subsequent decline, *Science*, *313*(5795), 1928–1928, 2006.

Lyle, M., J. Barron, T. J. Bralower, M. Huber, A. Olivarez Lyle, A. C. Ravelo, D. K. Rea, and P. A. Wilson, Pacific ocean and cenozoic evolution of climate, *Reviews of Geophysics*, *46*(2), 2008.

Ma, Z., E. Gray, E. Thomas, B. Murphy, J. Zachos, and A. Paytan, Carbon sequestration during the palaeocene-eocene thermal maximum by an efficient biological pump, *Nature Geoscience*, *7*(5), 382–388, 2014.

Mackenzie, F. T., L. M. Ver, C. Sabine, M. Lane, and A. Lerman, C, n, p, s global biogeochemical cycles and modeling of global change, in *Interactions of C, N, P and S Biogeochemical Cycles and Global Change*, pp. 1–61, Springer, 1993.

MacLeod, K. G., R. M. Smith, P. L. Koch, and P. D. Ward, Timing of mammal-like reptile extinctions across the permian-triassic boundary in south africa, *Geology*, *28*(3), 227–230, 2000.

Magaritz, M., and W. T. Holser, The permian-triassic of the gartnerkofel-1 core (carnic alps, austria): carbon and oxygen isotope variation, *Abhandlungen der Geologischen Bundesanstalt*, *45*, 149–163, 1991.

Magaritz, M., R. Krishnamurthy, and W. T. Holser, Parallel trends in organic and inorganic carbon isotopes across the permian/triassic boundary, *American Journal of Science;(United States)*, *292*(10), 1992.

Martin, J. H., G. A. Knauer, D. M. Karl, and W. W. Broenkow, VERTEX: carbon cycling in the northeast Pacific, *Deep-Sea Res.*, *34(2)*, 267–285, 1987.

Matsumoto, K., Biology-mediated temperature control on atmospheric pco2 and ocean biogeochemistry, *Geophysical Research Letters*, *34*(20), 2007.

McCartney, K., A. R. Huffman, and M. Tredoux, A paradigm for endogenous causation of mass extinctions, *Geological Society of America Special Papers*, *247*, 125–138, 1990.

McInerney, F. A., and S. L. Wing, The paleocene-eocene thermal maximum: a perturbation of carbon cycle, climate, and biosphere with implications for the future, *Annual Review of Earth and Planetary Sciences*, *39*, 489–516, 2011.

McLean, D. M., Mantle degassing unification of the trans-kt geobiological record, in *Evolutionary biology*, pp. 287–313, Springer, 1986.

Menard, H. W., and S. M. Smith, Hypsometry of Ocean Basin Provinces, *J. Geophys. Res.*, *71(18)*, 4305–4325, 1966.

Miller, K. G., et al., The phanerozoic record of global sea-level change, *science*, *310*(5752), 1293–1298, 2005.

Milliman, J. D., Production and accumulation of calcium carbonate in the ocean: Budget of a nonsteady state, *Global Biogeochem. Cycles*, *4*, 927–957, 1993.

Misra, S., and P. N. Froelich, Lithium isotope history of cenozoic seawater: changes in silicate weathering and reverse weathering, *Science*, *335*(6070), 818–823, 2012.

Müller, R. D., M. Sdrolias, C. Gaina, B. Steinberger, and C. Heine, Long-term sea-level fluctuations driven by ocean basin dynamics, *science*, *319*(5868), 1357–1362, 2008.

Murphy, B., K. Farley, and J. Zachos, An extraterrestrial 3 he-based timescale for the paleocene–eocene thermal maximum (petm) from walvis ridge, iodp site 1266, *Geochimica et Cosmochimica Acta*, *74*(17), 5098–5108, 2010.

Olivarez Lyle, A., and M. W. Lyle, Missing organic carbon in Eocene marine sediments: Is metabolism the biological feedback that maintains end-member climates, *Paleoceanography*, *21*, PA2007, doi:10.1029/2005PA001,230, 2006.

Opdyke, B. N., and B. H. Wilkinson, Carbonate mineral saturation state and cratonic limestone accumulation, *Am. J. Sci.*, *293*, 217–234, 1993.

Osen, A. K., A. M. Winguth, C. Winguth, and C. R. Scotese, Sensitivity of late permian climate to bathymetric features and implications for the mass extinction, *Global and Planetary Change*, *105*, 171–179, 2013.

Pagani, M., K. Calderia, D. Archer, and J. C. Zachos, An ancient carbon mystery, *Science*, *314*, 1556–1557, 2006.

Pälike, C., M. L. Delaney, and J. C. Zachos, Deep-sea redox across the paleocene-eocene thermal maximum, *Geochemistry, Geophysics, Geosystems*, *15*(4), 1038–1053, 2014.

Pälike, H., et al., A cenozoic record of the equatorial pacific carbonate compensation depth, *Nature*, *488*(7413), 609, 2012.

Pancost, R. D., D. S. Steart, L. Handley, M. E. Collinson, J. J. Hooker, A. C. Scott, N. V. Grassineau, and I. J. Glasspool, Increased terrestrial methane cycling at the palaeocene–eocene thermal maximum, *Nature*, *449*(7160), 332–335, 2007.

Payne, J. L., A. V. Turchyn, A. Paytan, D. J. DePaolo, D. J. Lehrmann, M. Yu, and J. Wei, Calcium isotope constraints on the end-permian mass extinction, *Proceedings of the National Academy of Sciences*, *107*(19), 8543–8548, 2010.

Pearson, P. N., G. L. Foster, and B. S. Wade, Atmospheric carbon dioxide through the eocene-oligocene climate transition, *Nature*, *461*(7267), 1110, 2009.

Penman, D. E., Silicate weathering and north atlantic silica burial during the paleocene-eocene thermal maximum, *Geology*, pp. G37,704–1, 2016.

Penman, D. E., et al., An abyssal carbonate compensation depth overshoot in the aftermath of the palaeocene-eocene thermal maximum, *Nature Geoscience*, 2016.

Pilson, M. E., *An Introduction to the Chemistry of the Sea*, Cambridge University Press, 2012.

Poore, H., R. Samworth, N. White, S. Jones, and I. McCave, Neogene overflow of northern component water at the greenland-scotland ridge, *Geochemistry, Geophysics, Geosystems*, *7*(6), 2006.

Post, W. M., T.-H. Peng, W. R. Emanuel, A. W. King, V. H. Dale, D. L. DeAngelis, et al., The global carbon cycle, *American scientist*, *78*(4), 310–326, 1990.

Raitzsch, M., and B. Hönisch, Cenozoic boron isotope variations in benthic foraminifers, *Geology*, *41*(5), 591–594, 2013.

Rampino, M. R., and K. Caldeira, Major perturbation of ocean chemistry and a strangelove oceanafter the end-permian mass extinction, *Terra Nova*, *17*(6), 554–559, 2005.

Ravizza, G., R. N. Norris, J. Blusztajn, and M.-P. Aubry, An osmium isotope excursion associated with the late Paleocene thermal maximum: Evidence of intensified chemical weathering, *Paleoceanogr.*, *16*, 155–163, 2001.

Raymo, M. E., and W. F. Ruddiman, Tectonic forcing of late cenozoic climate, *Nature*, *359*(6391), 117–122, 1992.

Raymo, M. E., W. F. Ruddiman, and P. N. Froelich, Influence of late cenozoic mountain building on ocean geochemical cycles, *Geology*, *16*(7), 649–653, 1988.

Retallack, G. J., Postapocalyptic greenhouse paleoclimate revealed by earliest triassic paleosols in the sydney basin, australia, *Geological Society of America Bulletin*, *111*(1), 52–70, 1999.

Ridgwell, A., A Mid Mesozoic Revolution in the regulation of ocean chemistry, *Marine Geology*, *217*, 339–357, 2005.

Ridgwell, A., Interpreting transient carbonate compensation depth changes by marine sediment core modeling, *Paleoceanography*, *22*(4), 2007.

Ridgwell, A., and R. E. Zeebe, The role of the global carbonate cycle in the regulation and evolution of the Earth System, *Earth and Planetary Science Letters*, *234*, 299–315, 2005.

Ridgwell, A. J., M. J. Kennedy, and K. Caldeira, Carbonate deposition, climate stability, and neoproterozoic ice ages, *Science*, *302*(5646), 859–862, 2003.

Riggs, S. R., Paleoceanographic model of neogene phosphorite deposition, us atlantic continental margin, *Science*, *223*, 123–132, 1984.

Röhl, U., T. Westerhold, T. J. Bralower, and J. C. Zachos, On the duration of the paleocene-eocene thermal maximum (petm), *Geochemistry, Geophysics, Geosystems*, *8*(12), 2007.

Royer, D. L., R. A. Berner, I. P. Montanez, N. J. Tabor, and D. J. Beerling, CO_2 as a primary driver of Phanerozoic climate change, *GSA Today*, *14(3)*, 4–10, 2004.

Royer, D. L., Y. Donnadieu, J. Park, J. Kowalczyk, and Y. Goddéris, Error analysis of co2 and o2 estimates from the long-term geochemical model geocarbsulf, *American Journal of Science*, *314*(9), 1259–1283, 2014.

Ruttenberg, K., Reassessment of the oceanic residence time of phosphorus, *Chemical Geology*, *107*(3-4), 405–409, 1993.

Samworth, R., and H. Poore, Understanding past ocean circulations: a nonparametric regression case study, *Statistical Modelling*, *5*(4), 289–307, 2005.

Sarmiento, J. L., and N. Gruber, *Ocean biogeochemical dynamics: Princeton*, Princeton University Press, New Jersey, 2006.

Schulte, P., C. Scheibner, and R. P. Speijer, Fluvial discharge and sea-level changes controlling black shale deposition during the paleocene–eocene thermal maximum in the dababiya quarry section, egypt, *Chemical Geology*, *285*(1), 167–183, 2011.

Seki, O., G. L. Foster, D. N. Schmidt, A. Mackensen, K. Kawamura, and R. D. Pancost, Alkenone and boron-based pliocene pco 2 records, *Earth and Planetary Science Letters*, *292*(1), 201–211, 2010.

Skulan, J., D. J. DePaolo, and T. L. Owens, Biological control of calcium isotopic abundances in the global calcium cycle, *Geochimica et Cosmochimica Acta*, *61*(12), 2505–2510, 1997.

Slomp, C., and P. Van Cappellen, The global marine phosphorus cycle: sensitivity to oceanic circulation, *Biogeosciences*, *4*, 155–171, 2007.

Slotnick, B. S., V. Lauretano, J. Backman, G. R. Dickens, A. Sluijs, and L. Lourens, Early paleogene variations in the calcite compensation depth: new constraints using old borehole sediments from across ninetyeast ridge, central indian ocean, *Climate of the Past*, *11*, 473–493, 2015.

Sluijs, A., H. Brinkhuis, et al., A dynamic climate and ecosystem state during the paleocene-eocene thermal maximum: Inferences from dinoflagellate cyst assemblages on the new jersey shelf, *Biogeosciences*, *6*(8), 1755–1781, 2009.

Sluijs, A., R. E. Zeebe, P. K. Bijl, and S. M. Bohaty, A middle eocene carbon cycle conundrum, *Nature Geoscience*, *6*(6), 429–434, 2013.

Sluijs, A., L. Van Roij, G. Harrington, S. Schouten, J. Sessa, L. LeVay, G.-J. Reichart, and C. Slomp, Warming, euxinia and sea level rise during the paleocene–eocene thermal maximum on the gulf coastal plain: implications for ocean oxygenation and nutrient cycling, *Climate of the Past*, *10*(4), 1421–1439, 2014.

Sluijs, A., et al., Subtropical Arctic Ocean temperatures during the Palaeocene/Eocene thermal maximum, *Nature*, *441*, 610–613, 2006.

Stanley, S. M., Relation of phanerozoic stable isotope excursions to climate, bacterial metabolism, and major extinctions, *Proceedings of the National Academy of Sciences*, *107*(45), 19,185–19,189, 2010.

Stap, L. B., B. de Boer, M. Ziegler, R. Bintanja, L. J. Lourens, and R. S. van de Wal, Co 2 over the past 5 million years: Continuous simulation and new δ 11 b-based proxy data, *Earth and Planetary Science Letters*, *439*, 1–10, 2016.

Stoll, H. M., and S. Bains, Coccolith sr/ca records of productivity during the paleocene-eocene thermal maximum from the weddell sea, *Paleoceanography*, *18*(2), 2003.

Stuecker, M. F., Modeling ocean carbon cycling and acidification in response to massive carbon release, Master's thesis, Carl-von-Ossietzky Universität Oldenburg, Germany, 2009.

Stuecker, M. F., and R. E. Zeebe, Ocean chemistry and atmospheric CO_2 sensitivity to carbon perturbations throughout the cenozoic, *Geophysical Research Letters*, *37*(3), 2010.

Sun, Y., M. M. Joachimski, P. B. Wignall, C. Yan, Y. Chen, H. Jiang, L. Wang, and X. Lai, Lethally hot temperatures during the early triassic greenhouse, *Science*, *338*(6105), 366–370, 2012.

Svensen, H., S. Planke, A. Malthe-Sørenssen, B. Jamtveit, R. Myklebust, T. R. Eidem, and S. S. Rey, Release of methane from a volcanic basin as a mechanism for initial eocene global warming, *Nature*, *429*(6991), 542–545, 2004.

Toggweiler, J. R., Variation of atmospheric CO_2 by ventilation of the ocean's deepest water, *Paleoceanogr.*, *14*, 571–588, 1999.

Tripati, A., C. D. Roberts, and R. E. Eagle, Coupling of CO_2 and Ice Sheet Stability Over Major Climate Transitions of the Last 20 Million Years, *Science Express*, p. 10.1126/science.1178296, 2009.

Tsandev, I., and C. Slomp, Modeling phosphorus cycling and carbon burial during cretaceous oceanic anoxic events, *Earth and Planetary Science Letters*, *286*(1), 71–79, 2009.

Tyrrell, T., The relative influences of nitrogen and phosphorus on oceanic primary production, *Nature*, *400*(6744), 525–531, 1999.

Tyrrell, T., and R. E. Zeebe, History of carbonate ion concentration over the last 100 million years, *Geochim. Cosmochim. Acta*, *68(17)*, 3521–3530, 2004.

Uchikawa, J., and R. E. Zeebe, Influence of terrestial weathering on ocean acidification and the next glacial inception, *Geophysical Research Letters*, *35*, L23,608, doi:10.1029/2008GL035,963, 2008.

Urey, H. C., *The Planets: Their Origin and Development*, Yale University Press, New Haven, Connecticut, pp. 245, 1952.

van Andel, T. H., and T. C. Moore, Cenozoic calcium carbonate distribution and calcite compensation depth in the central equatorial Pacific Ocean, *Geology*, *2*, 87–92, 1974.

van Andel, T. H., Mesozoic/Cenozoic calcite compensation depth and the global distribution of calcareous sediments, *Earth Planet. Sci. Lett.*, *26*, 187–194, 1975.

Van Cappellen, P., and E. D. Ingall, Benthic phosphorus regeneration, net primary production, and ocean anoxia: A model of the coupled marine biogeochemical cycles of carbon and phosphorus, *Paleoceanography*, *9*(5), 677–692, 1994.

Van Cappellen, P., E. D. Ingall, et al., Redox stabilization of the atmosphere and oceans by phosphorus-limited marine productivity, *Science(Washington)*, *271*(5248), 493–496, 1996.

Van Der Meer, D. G., R. E. Zeebe, D. J. van Hinsbergen, A. Sluijs, W. Spakman, and T. H. Torsvik, Plate tectonic controls on atmospheric co2 levels since the triassic, *Proceedings of the National Academy of Sciences*, *111*(12), 4380–4385, 2014.

Veizer, J., et al., $^{87}Sr/^{86}Sr$, $\delta^{13}C$ and $\delta^{18}O$ evolution of Phanerozoic seawater, *Chem. Geol.*, *161*, 59–88, 1999.

Walker, J. C. G., and J. F. Kasting, Effects of fuel and forest conservation on future levels of atmospheric carbon dioxide, *Palaeogeogr. Palaeoclim. Palaeoecology*, *97*, 151–189, 1992.

Walker, L. J., B. H. Wilkinson, and L. C. Ivany, Continental drift and phanerozoic carbonate accumulation in shallow-shelf and deep-marine settings, *The Journal of geology*, *110*(1), 75–87, 2002.

Walker, P. B. H., J. C. G., and J. F. Kasting, Negative feedback mechanism for the long-term stabilization of earth‘s surface temperature, *J. Geophys. Res.*, *86*, 9776–9782, 1981.

Wallmann, K., Controls of hte Cretaceous and Cenozoic evolution of seawater composition, atmospheric CO_2 and climate, *Geochim. Cosmochim. Acta*, *65*, 3005–3025, 2001.

Wallmann, K., Feedbacks between oceanic redox states and marine productivity: A model

perspective focused on benthic phosphorus cycling, *Global biogeochemical cycles*, *17*(3), 2003.

Wallmann, K., Phosphorus imbalance in the global ocean?, *Global Biogeochemical Cycles*, *24*(4), 2010.

Walsh, J. J., P. Biscaye, and G. Csanady, Importance of continental margins in the marine biogeochemical cycling of carbon and nitrogen, *Nature*, *350*(6313), 53–55, 1991.

Weiss, R., The solubility of nitrogen, oxygen and argon in water and seawater, in *Deep Sea Research and Oceanographic Abstracts*, vol. 17, pp. 721–735, Elsevier, 1970.

Westerhold, T., U. Rohl, B. Donner, H. K. McCarren, and J. C. Zachos, A complete high-resolution Paleocene benthic stable isotope record for the central Pacific (ODP Site 1209), *Paleoceanography*, *26*, PA2216, doi:10.1029/2010PA002,092, 2011.

Wignall, P., Large igneous provinces and mass extinctions, *Earth-Science Reviews*, *53*(1), 1–33, 2001.

Wignall, P. B., and R. Newton, Contrasting deep-water records from the upper permian and lower triassic of south tibet and british columbia: evidence for a diachronous mass extinction, *Palaios*, *18*(2), 153–167, 2003.

Willenbring, J. K., and F. von Blanckenburg, Long-term stability of global erosion rates and weathering during late-cenozoic cooling, *Nature*, *465*(7295), 211–214, 2010.

Wolf-Gladrow, D. A., R. E. Zeebe, C. Klaas, A. Körtzinger, and A. G. Dickson, Total alkalinity: The explicit conservative expression and its application to biogeochemical processes, *Marine Chemistry*, *106*(1), 287–300, 2007.

Woodruff, F., and S. M. Savin, Miocene deepwater oceanography, *Paleoceanography*, *4*(1), 87–140, 1989.

Woods, A. D., D. J. Bottjer, M. Mutti, and J. Morrison, Lower triassic large sea-floor carbonate cements: Their origin and a mechanism for the prolonged biotic recovery from the end-permian mass extinction, *Geology*, *27*(7), 645–648, 1999.

Wright, J. D., K. G. Miller, and R. G. Fairbanks, Evolution of modern deepwater circulation: Evidence from the late miocene southern ocean, *Paleoceanography*, *6*(2), 275–290, 1991.

Zachos, J. C., M. Pagani, L. Sloan, E. Thomas, and K. Billups, Trends, rhythms, and aberrations in global climate 65 Ma to present, *Science*, *292*, 686–693, 2001.

Zachos, J. C., M. W. Wara, S. Bohaty, M. L. Delaney, M. R. Petrizzo, A. Brill, T. J. Bralower, and I. Premoli-Silva, A transient rise in tropical sea surface temperature during the Paleocene-Eocene Thermal Maximum, *Science*, *302*, 1551–1554, 2003.

Zachos, J. C., G. R. Dickens, and R. E. Zeebe, An early Cenozoic perspective on greenhouse warming and carbon-cycle dynamics, *Nature*, *451*, 279–283, doi:10.1038/nature06,588, 2008.

Zachos, J. C., et al., Rapid acidification of the ocean during the Paleocene-Eocene Thermal Maximum, *Science*, *308*, 1611–1615, 2005.

Zeebe, R. E., LOSCAR: Long-term Ocean-atmosphere-Sediment CArbon cycle Reservoir Model v2.0.4, *Geosci. Model Development*, *1*, 149–166, 2012a.

Zeebe, R. E., History of Seawater Carbonate Chemistry, Atmospheric CO_2 and Ocean Acidification, *Annu. Rev. Earth Planet. Sci.*, *40*, 141:165, 2012b.

Zeebe, R. E., and P. Westbroek, A simple model for the $CaCO_3$ saturation state of the ocean: The "Strangelove", the "Neritan", and the "Cretan" Ocean, *Geochem. Geophys. Geosyst.*, *4(12)*, 1104, doi:10.1029/2003GC000,538, 2003.

Zeebe, R. E., and D. A. Wolf-Gladrow, *CO_2 in Seawater: Equilibrium, Kinetics, Isotopes*, Elsevier Oceanography Series, Amsterdam, pp. 346, 2001.

Zeebe, R. E., and J. C. Zachos, Reversed deep-sea carbonate ion basin-gradient during Paleocene-Eocene Thermal Maximum, *Paleoceanogr.*, *22*, PA3201, doi:10.1029/2006PA001,395, 2007.

Zeebe, R. E., and J. C. Zachos, Long-term legacy of massive carbon input to the earth system: Anthropocene versus eocene, *Philosophical Transactions of the Royal Society of London A: Mathematical, Physical and Engineering Sciences*, *371*(2001), 20120,006, 2013.

Zeebe, R. E., J. C. Zachos, K. Caldeira, and T. Tyrrell, Oceans: Carbon Emissions and Acidification (in Perspectives), *Science*, *321*, 51–52, doi:10.1126/science.1159,124, 2008.

Zeebe, R. E., J. C. Zachos, and G. R. Dickens, Carbon dioxide forcing alone insufficient to explain Palaeocene-Eocene Thermal Maximum warming, *Nature Geoscience*, *published online: 13 July 2009*, DOI:10.1038/NGEO578, 2009.

Zeebe, R. E., A. Ridgwell, and J. C. Zachos, Anthropogenic carbon release rate unprecedented during the past 66 million years, *Nature Geoscience*, *9*(4), 325–329, 2016.

Zeebe, R. E., T. Westerhold, K. Littler, and J. C. Zachos, Orbital forcing of the paleocene and eocene carbon cycle, *Paleoceanography*, *32*(5), 440–465, 2017.

Zhang, Y. G., M. Pagani, Z. Liu, S. M. Bohaty, and R. DeConto, A 40-million-year history of atmospheric co2, *Phil. Trans. R. Soc. A*, *371*(2001), 20130,096, 2013.

Zhu, P., and J. D. Macdougall, Calcium isotopes in the marine environment and the oceanic calcium cycle, *Geochimica et Cosmochimica Acta*, *62*(10), 1691–1698, 1998.